University of Pisa

Department of Physics

Ph.D. graduate school in Physics

Ph.D. Thesis

Mutual information, vibrational scaling, short-time dynamical heterogeneity and secondary relaxation in coarse-grained polymer systems

Candidate
Antonio Tripodo

Supervisor
Prof. Dino Leporini

Coordinator of the Ph.D. graduate school
Prof. Dario Pisignano

October 2020

Contents

Preface

Understanding the extraordinary viscous slow-down that accompanies glass formation is one of the major open challenges in condensed matter physics. On approaching the glass transition from the high fluidity regime, a particle spends increasing time within the cage formed by the first neighbors where it rattles with amplitude $\langle u^2 \rangle^{1/2}$. Its average escape time, i.e. the structural relaxation time τ_α, increases from a few picoseconds in the low-viscosity regime up to thousands of seconds at the glass transition. The transition from a liquid to a glass is accompanied by the progressive appearance of *dynamical heterogeneity*: it is observed the growth of transient spatial fluctuations in the local dynamical behavior. Experimentally, dynamical heterogeneity manifests itself in the relaxation spectra, measured through mechanical or dielectric probes, showing a very broad range of relaxation times and a strongly non-exponential behavior. This suggests the existence of wide distributions of relaxation rates. Despite the huge difference in time scales between the rattling motion and the relaxation, several studies addressed the fast rattling process within the cage to understand the slow relaxation dynamics. Within this context, several correlations between the amplitude of the rattling motion and the structural relaxation time have been found in a large variety of systems. This correlation is summarized in the form of a universal master curve

$$\tau_\alpha = \mathcal{F}(\langle u^2 \rangle) \tag{1}$$

An analytical derivation for this relation, in the framework of the Hall-Wolynes model, relies on the wide distribution of relaxation time, which is a manifestation of the dynamical heterogeneity.

This Thesis work has two main purposes, both central in the field of research of the glass transition physics by means of coarse-grained molecular dynamics simulations: i) achieving a deeper understanding of the connection between fast dynamics and slow relaxation ii) gaining further insight on the role of the dynamical heterogeneity in such a connection.

Chapters 1 and 2 are the introductory ones. The first one gives a quick presentation of the general context of this research. The second chapter is

dedicated to a brief introduction to Information Theory, as in some of the works presented in this thesis, Mutual Information is employed as a more refined and sensitive measure of correlation.

Chapter 3 and 4 are dedicated to the study of displacement-displacement correlation in a simple molecular liquid by means of mutual information. The research is motivated by, and as a follow-up to, previous studies based on displacements correlation function in the light of novel investigation carried out on atomic liquids by employing mutual information. Chapter 3 focuses on the mutual information correlation length. A comparison with both the results obtained in atomic liquids and the ones resulting from simple correlation function is carried out to determine whether mutual information could improve the analysis of correlated motion. Chapter 4 extends the previous investigation with a closer look at dynamical heterogeneity. Two particle fractions, with different mobilities and relaxations, are identified on the basis of mutual information related properties. The two fractions scalings, in the form of the aforementioned universal relation between relaxation and rattling amplitude, are investigated. The spatial and structural properties of these two fractions are studied as well.

In Chapter 5 and 6 a slightly more complex system is taken into consideration: a liquid of 25-mers with bending potential and a nearly fixed bond length shorter than the zero of the Lennard-Jones interaction. Such peculiar features give rise to the emergence of a faster secondary relaxation process. Chapter 5 investigates whether the presence of a secondary relaxation could interfere with the universal correlation between vibrational dynamics and primary relaxation. An analysis of the performance of secondary relaxation probe functions, including mutual information, is also carried out. Chapter 6 focuses on the role of the secondary relaxation on the system dynamical heterogeneity as sensed by the non-Gaussian parameter. A microscopical explanation of the phenomenon, as well as its impact on other standard observables, is also given.

Each Chapter presents a brief introductory paragraph to contextualize the work, motivated by the research performed in recent literature.

Publications

The research activity carried out during my Ph.D. has been reported in the following papers:

- A. Tripodo, A. Giuntoli, M. Malvaldi, and D. Leporini. *Mutual information does not detect growing correlations in the propensity of a model molecular liquid*. Soft Matter, 2019.
- A. Tripodo, F. Puosi, M. Malvaldi, and D. Leporini. *Vibrational scaling of the heterogeneous dynamics detected by mutual information*. Eur. Phys. J. E, 42(11), 2019
- F. Puosi, A. Tripodo, and D. Leporini. *Fast vibrational modes and slow heterogeneous dynamics in polymers and viscous liquids*. International Journal of Molecular Sciences, 20(5708), 2019.
- A. Tripodo, F. Puosi, M. Malvaldi, S. Capaccioli, and D. Leporini. *Coincident correlation between vibrational dynamics and primary relaxation of polymers with strong or weak Johari-Goldstein relaxation*. Polymers, 12(761), 2020.
- F. Puosi, A. Tripodo, M. Malvaldi, and D. Leporini. *Johari-Goldstein heterogeneous dynamics in a model polymer melt*, in preparation
- A. Tripodo, F. Puosi, M. Malvaldi, and D. Leporini. *Clustering properties of early-relaxing and late-relaxing particles in a molecular liquid*, in preparation

Other publications outside of the topic of my Ph.D. thesis:

- A. Pelissetto, A. Tripodo, and E. Vicari. *Criticality of $O(N)$ symmetric models in the presence of discrete gauge symmetries*. Phys. Rev. E , 97, 2018
- M. Malvaldi, A. Tripodo, F. Puosi, and D. Leporini. *Solvation shell dynamics as a novel viewpoint for long-time dynamics in polymeric glassformers*, in preparation

Chapter 1

Introduction

1.1 Supercooled liquids and glass transition

A liquid whose temperature is lowered below its melting point T_{melt} is expected to undergo a first order phase transition forming a crystal. However, if the cooling rate exceeds the time scales involving the crystal formation, the liquid-crystal phase transition can be avoided[12]. In this scenario, the system is kept in a metastable phase called *supercooled phase* (see Fig.1.1). Further cooling of the system beyond the *glass transition temperature* T_g entails a fall out of the equilibrium. The attained state is called a *glass*. Supercooled liquids and glasses have a very rich phenomenology which is still far from being completely understood [13, 39, 47].

In the supercooled phase, typical macroscopic time scales dramatically increase upon cooling and end up being greater than typical experimental observation times at the glass transition temperature T_g. Fig.1.2 offers a quick understanding of how much the typical time scale of the system τ_α, on which density fluctuation relax, changes around T_g: at a molecular level, far from T_g, these density fluctuations relax in times of the order of the picosecond whereas at T_g the typical time scales become of the order of 10^2 s, 14 orders of magnitude larger [11, 146]. Such an increase is impressive especially considering the change in temperature is quite moderate. Empirically one usually finds that $T_g \approx 2/3\ T_{melt}$.

The increasing of the relaxation time τ_α is accompanied by an increase of the shear viscosity η of the liquid. For a glass-forming liquid just above the glass transition the typical viscosity is of the order of $10^{13}P$. To have a grasp of how large this value is, simply recall that at the melting point a liquid's viscosity rarely exceeds $\eta \sim 10^{-1}P$. A system with $\eta = 10^{13}P$ appears mechanically solid on the experimental time scale, but it still exhibits the

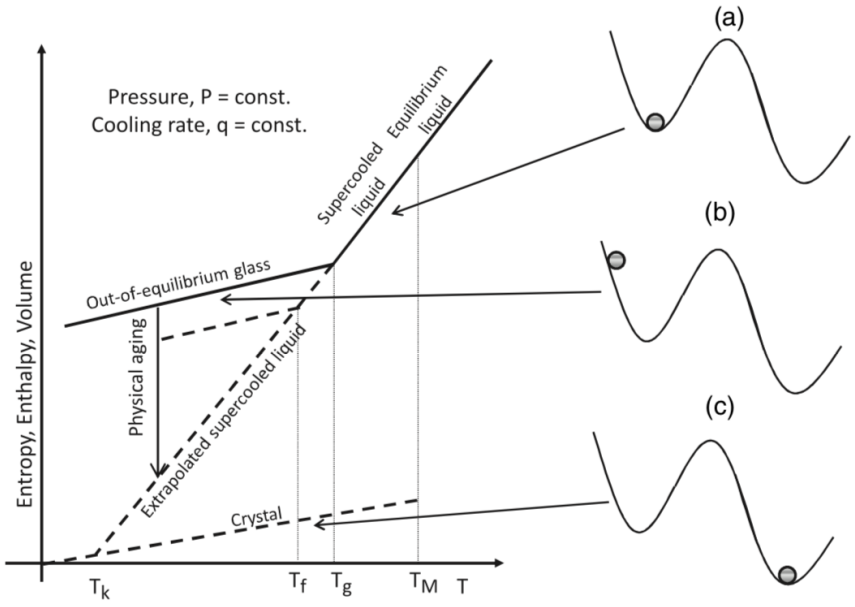

Figure 1.1: Left: a typical temperature dependence of properties of a glass-forming system at constant pressure. Right: schematic representation of the free energy of the indicated states: a supercooled liquid (a), a glass (b) and a crystal (c). Reprinted from Ref.[36]

typical structural features and lacking long range order of a liquid.

One of the key aspects related to going off-equilibrium is the loss of ergodicity. The system has not enough time to properly explore the phase space and tends to remain trapped in local energy minima. This leads to a reduction of the number of degrees of freedom accessible to the system and a consequent drop in the constant pressure specific heat at T_{glass} to a value very close to the one of the crystalline phase [11].

The glass transition temperature T_g marks the point at which the relaxation time of the liquid τ_α exceeds the available experimental time τ_{ex}. This is an odd definition for a transition temperature, especially having in mind phase-transitions happening at a given critical point such as the ferromagnetic or the liquid-vapor transition. From this perspective, it is important to underline that the glass transition is not an usual phase transition, as T_g depends on the experimental protocol and in particular on the cooling rate and experimental times. Nevertheless, the peculiar characteristics of a glass and the sharp increase of the relaxation time and viscosity make the definition of T_g quite robust from an operative point of view. As a matter of fact, the robustness of the definition is granted by the exponential increase of the

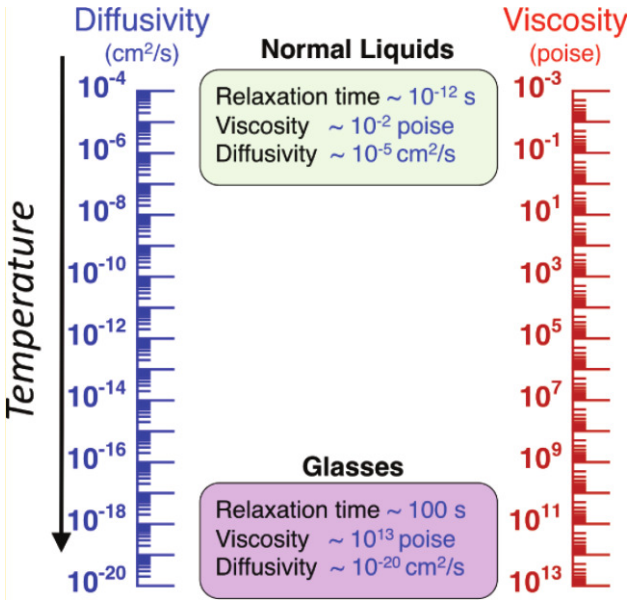

Figure 1.2: Comparison of the diffusivity and viscosity between a typical liquid (such as the water at room temperature) and a typical glass. Note the huge increase of the relaxation time from $10^{-12}s$ to $10^{2}s$. Reprinted from [146].

relaxation time and viscosity on approaching the glass transition. T_g is often defined as the temperature at which the relaxation time is equal to $10^2 s$.

The ability to transit into a glassy state is universal: once the highly viscous liquid state is reached, glass formation is unavoidable upon continued cooling. Under the right circumstances, any sort of molecular liquid [46], polymer [134], bio-material [70], metal [40] or molten salt [81] is able to form a glass. In many cases a rapid cooling is necessary to avoid the crystallization (cooling rate $\sim 10^6 K/s$ in the case of metallic glasses). A good glass former is therefore a liquid which is characterized by very low rates of crystal nucleation and growth at all temperatures [142]. Good glass formers are organic and ionic liquids, silicates, polymers and also some metallic glasses [57].

Despite the aforementioned universality of the glass transition, different liquids shows a disparate variety of relaxation times and viscosity temperature behavior on approaching T_g. For instance, Silica (SiO_2), shows an Arrhenius temperature dependence of the viscosity, close to its T_g

$$\eta \sim \exp\left[\frac{\Delta E}{k_B T}\right] \tag{1.1}$$

Such a behavior is obtained when the dynamics of the system is characterized by the presence of temperature independent energy barriers of amplitude

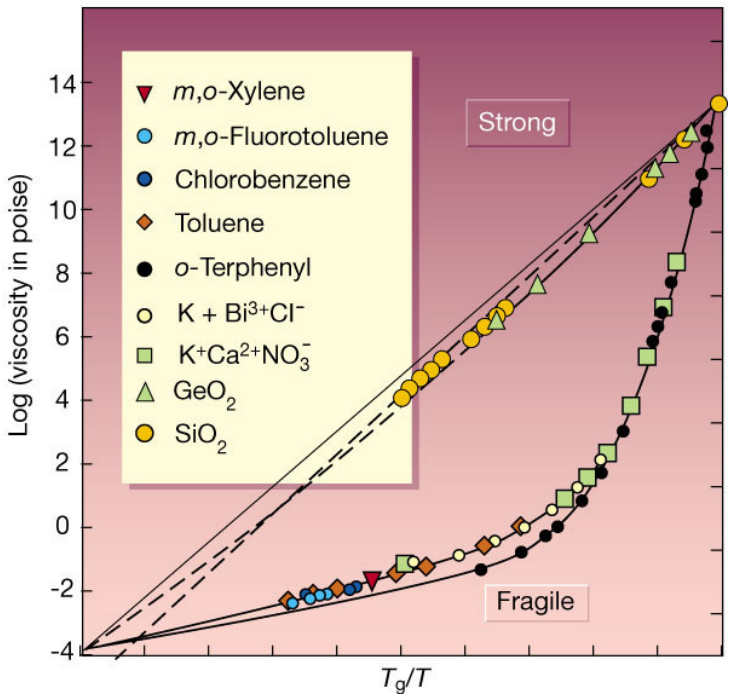

Figure 1.3: Angell plot showing the viscosity as a function of the inverse temperature normalized at the glass transition temperature T_g for different substances. An Arrhenius behavior results in a straight line in this plot. This is typical of strong glass-formers. Non-Arrhenius increase of the viscosity corresponds to fragile glass-formers. Reprinted from [47].

ΔE. Thermal fluctuations needs to overcome such barriers for the system to relax[47]. Other liquids, like many polymers, deviates from this behavior and are characterized by a steeper increase in the viscosity with decreasing temperature. The so called Angell plot [10] shown in Fig. 1.3 displays the temperature dependence of the viscosity of a wide variety of supercooled liquids at atmospheric pressure. Defining T_g as the temperature at which viscosity reaches the value of $\eta(T_g) = 10^{13}P$, all the curves are normalized to the same value at T_g. The Angell plot evidences two characteristic behavior dividing liquids into *strong* and *fragile* glass formers depending on the viscosity temperature behavior on approaching the glass transition temperature T_g. Silica (SiO_2) and $Ge0_2$ are the prototypical strong liquids whereas *o*-terphenyl (OTP) and toluene (C_7H_8) are the canonical fragile glass-formers (see Fig.1.3). The terminology *strong* and *fragile* is not related to mechanical properties of the given glass but was originally introduced in relation to the evolution of the short-range order close to T_g[31]. The dynamics of strong glass formers is characterized by a clear Arrhenius behavior, resulting

in linear curves of $\log \eta(^{T_g}/_T)$ in Fig. 1.3. The other family of curves, to which the vast majority of glass-forming polymers belongs, corresponds to fragile liquids, for which the viscosity increases much more strongly upon cooling toward T_g. These super-Arrhenius behaviors are often fitted [47] by the Vogel-Fulcher-Tammann (VFT) expression

$$\eta(T) \sim \exp\left[\frac{A}{T - T_0}\right] \tag{1.2}$$

where A is a temperature independent constant. Notably, Eq. 1.2 implies a divergence of the viscosity at the finite temperature T_0, a prediction that cannot be verified because the system is supposed to fall out of equilibrium as T_0 is approached. However, the physical origin of the non-Arrhenius behavior of fragile liquids is still an actively investigated question, and many other models exist (see for example [18, 23, 60]).

While the Angell plot offers a visual categorization of glass formers, a more quantitative classification is provided by the definition of the kinetic *fragility*

$$m = \left.\frac{\partial \log \eta}{\partial\left(\frac{T_g}{T}\right)}\right|_{T=T_g} \tag{1.3}$$

The van der Waals molecular liquids, such as o-terphenyl OTP and toluene C_7H_8 are the classical fragile ($m = 70 \div 150$) systems. The strong glass-formers ($m = 17 \div 35$) are instead characterized by strong covalent directional bonds, forming space-filling networks (like silica SiO_2 and germanium dioxide GeO_2). Hydrogen bonded materials (like glycerol or propylene glycols) present an intermediate level of fragility ($m = 40 \div 70$).

Parallel to the huge increase in viscosity, the solid-like behavior becomes apparent at microscopic level, too. It is observed that a particle spends increasing time within the cage formed by the first neighbors where it rattles with amplitude $\langle u^2 \rangle^{1/2}$ on picosecond time scales[109]. This temporary trapping is rather persistent and the particle average escape time increases sharply close to the glass transition[31]. Within the microscopical picture, this trapping time provides as useful definition of τ_α, the structural relaxation time. The quantity $\langle u^2 \rangle$ appears in the expression of the Debye-Waller (DW) factor, which, assuming harmonicity and isotropy of the thermal motion, takes the form $\exp(-q\langle u^2 \rangle/3)$, where q is the absolute value of the scattering vector [16]. It is therefore common to refer to $\langle u^2 \rangle$ as DW factor too. In the present work we will adopt the same convention.

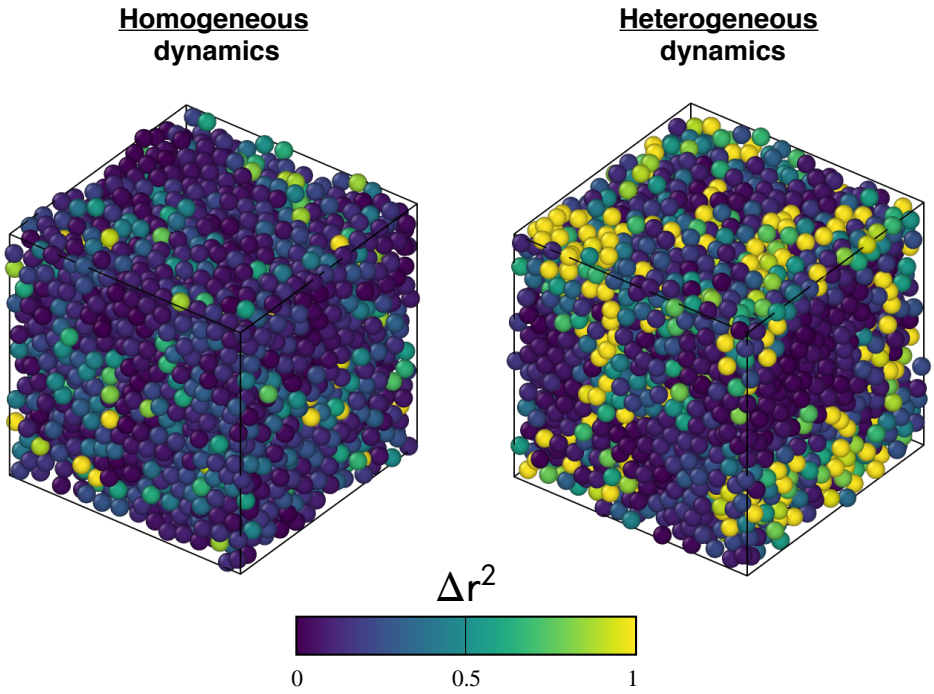

Figure 1.4: Molecular dynamics simulation of a polymer melt (see Sec.1.2 and Sec.1.3). Monomer arrangements at a time t_0 of two states with homogeneous and heterogeneous dynamics. Bonds are removed for clarity reasons. Particles are colored according to their squared displacements in the time interval $[t_0 - \tau_\alpha, t_0]$, normalized to the global maximum value of each state. Homogeneous, i.e. position-independent, dynamics of the monomers is an aspect of systems with fast relaxation. Conversely, in the presence of heterogeneous dynamics clusters of particles with extremely high mobility coexist with nearly immobile ones, slowing down the relaxation.

The transition from a liquid to a glass is accompanied by the growth of transient domains which exhibit different mobility, e.g. see Fig.1.4. The phenomenon is usually dubbed "*dynamical heterogeneity*" (DH) and has been extensively studied, [31, 52, 86, 132, 143, 155, 159]. The size of the domains is relatively small involving about 10 molecule diameters [59], corresponding to a few nanometers [159]. On a more general ground, the size of DH domains is strictly related to the possible presence of characteristic length scales in glassforming systems. This aspect will be discussed in more detail in Chapter 3.

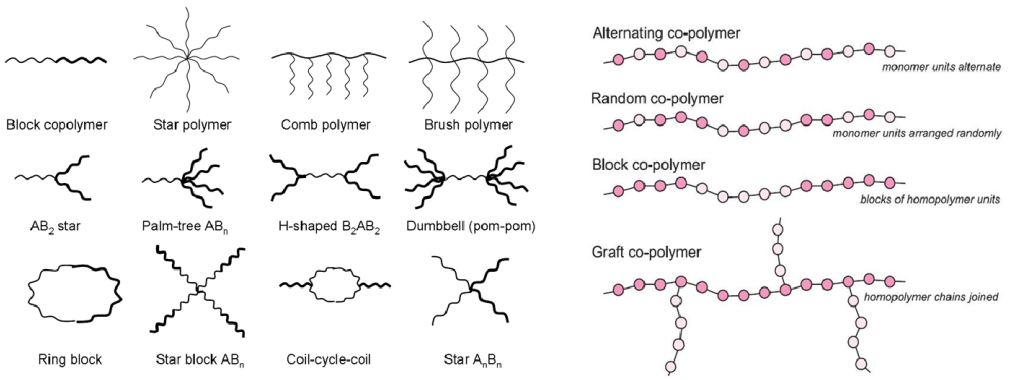

Figure 1.5: Classification of different types of polymers. Left: schematic representation of structures of polymers with different molecular architecture. Right: different classes of copolymers.

1.2 Polymers

Polymeric materials are ubiquitous in nature. From cellulose to the DNA molecules, from plexiglass in our homes to the nylon in the clothes or packaging, polymers exploit their high functional specificity in various applications. Their great versatility and adaptability in properties makes this class of materials attractive for technical applications and industrial research.

Polymers [71, 72, 151] are macro-molecules made up by a repetition of one or more constitutional repeating units, called monomers, connected by strong covalent bonds. The process that converts a bunch of monomers in a polymer is called *polymerization*. The term *polymer* usually refers to very large molecules. In a proper polymer, the number of monomers composing the macro-molecule is sufficient to provide a set of properties that do not vary markedly with the incorporation of additional ones [114]. A molecule with only a few constitutional repeating units is called an *oligomer*. An additional distinction can be made between *homopolymers*, consisting in chains of a single repeated unit, and *copolymers*, i.e. chains of monomers of different species, arranged in an alternating, random, block or other ways (right part of Fig. 1.5).

One reason for the abundance of applications of polymeric materials is the diversity in the chemical structure and composition ranging from simple linear homopolymers to branched polymers or more complex structures. Polymer chains can be classified by their *molecular architecture* and *configuration*. Molecular architecture, or *conformation*, deals with the spatial organization of the polymer chain. Many different conformations exist: lin-

ear, star, comb, network etc. Some examples of polymers with different molecular architecture are reported in the left part of Fig. 1.5. On the other hand, the configuration refers to the "permanent" stereostructure of a polymer. The configuration is defined by the polymerization process and it is preserved until the polymer undergoes further chemical reactions. In fact, any change of configuration requires the rupture of the chemical bonds forming the polymer.

Polymer science is attested to begin in 1920s [67], and the interest has been growing year after year also from a theoretical point of view, because of their many scaling properties [48]. Being very large molecules, polymers are very complex systems to study, especially due to the many diverse length scales involved in their dynamics, from the internal structure of a single monomer to the length and structure of the entire chain. The competition between chain-scale and monomer-scale spatial disposition gives rise to phenomena of geometrical frustration: at low temperature, the tendency of monomers to assume positions corresponding to an ordered configuration is opposed by the constraints imposed by the conformation of the chains. For polymers with regular enough chain structure, this usually results in two phase structures, in which crystalline and amorphous regions alternate [151]. For those polymers which have a strongly irregular chain structure, such as atactic and random copolymers, crystallization is completely inhibited, and in general even for those which own an ordered ground state the ordering is kinetically hard to achieve. For this reason, polymers are usually good glass formers.

1.3 Molecular dynamics simulations

Molecular Dynamics (MD) simulations have proven to be a powerful tool to study molecular liquids at a microscopic level [6, 22, 88]. Studying the glass transition of molecular liquids at a microscopic level is in principle straightforward since one has to answer a simple question: how do particles move in a liquid close to T_g? Attempt to answering this question experimentally is, of course, a daunting task. One should then resolve the dynamics of single molecules to be able to follow the trajectories of objects that are a few angstroms large on time scales of tens or hundreds of seconds. In recent years, such direct experimental investigations have been attempted using time- and space-resolved techniques such as atomic force microscopy [164] or single molecule spectroscopy [3], but this remains indeed a difficult task.

Conversely, in numerical simulations, the trajectory of each particle in the system can, by construction, be followed at all times. This allows to

easily quantify single-particle dynamics.

Trying to carry out a MD simulation of a liquid from first principles is an extremely complex job since the Schroedinger's equation of the entire system (atoms and electrons), should be solved. This is an incredible task, due to the huge amount of degrees of freedom (DoFs) of the system and to the complexity of the equations. This results in an extremely high computational cost that binds this kind of simulations to a relatively small number of atoms [25].

A way to reduce the computational cost is to eliminate the huge bottleneck of the calculation, namely the electronic DoFs, and with them the quantum mechanics treatment of the system. In fact, atomic DoFs can in most cases be described by classical dynamics by means of the so called *atomistic* (or all-atom) empirical models.

Classical computer simulations of supercooled liquids usually proceed by solving a cleverly discretized version of the equations of motion for all the particles positions and momenta given a potential interaction. Hence, considering the Hamiltonian for a system of N particles with mass m

$$H(\{\mathbf{r}_i, \mathbf{p}_i\}) = \sum_{i=1}^{N} \frac{\mathbf{p}_i^2}{2m} + V(\{\mathbf{r}_i\}) \tag{1.4}$$

in which $V(\{\mathbf{r}_i\})$ is the interaction term, it is possible to construct the equations of motion, either in Lagrangian, Hamiltonian or Newtonian form, which govern the entire time-evolution of the system and, therefore, its mechanical properties. Such equations of motion are energy conserving, hence they would describe the dynamics of the system in the micro-canonical ensemble. However, constant temperature or constant pressure schemes have been developed, allowing simulations to be performed in any desired statistical ensemble [5]. Furthermore, there are non-equilibrium simulation techniques that allow, for instance, computer studies of the aging dynamics or the non-linear rheology of supercooled fluids [61]. The integration of the equation of motion is, of course, numerical and thus approximated over a very short interval of time Δt which is usually of the order of 10^{-14}- $10^{-15}s$. This brings to light one of the major drawbacks of MD simulations of super-cooled liquids: it is impossible to completely follow the dynamics and explore its properties close to T_g. It is presently possible to follow the dynamics of a simple glass-forming liquid over more than eight decades of time, and over a temperature window in which average relaxation time scales increase by more than five decades.

In the case in which the studied liquid is composed of complex molecules or polymers, further simplification can be achieved through a *coarse-graining*

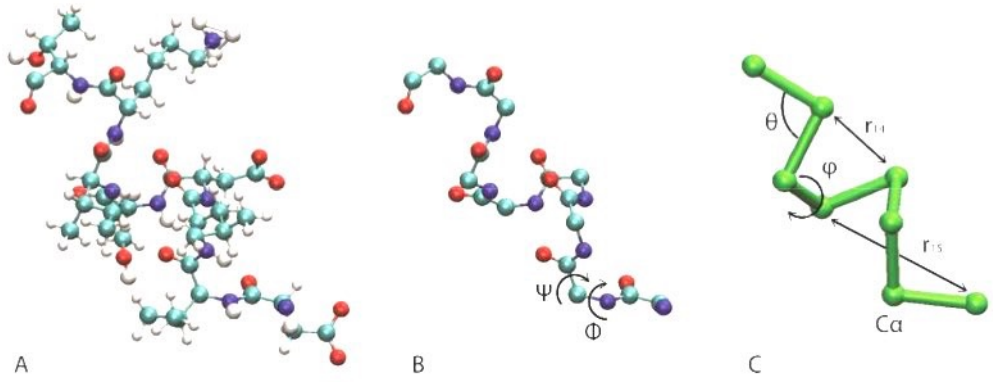

Figure 1.6: Coarse graining procedure from the atomistic to a Coarse-Grained model in a typical polypeptide (protein). From the all-atom representation (A) to the backbone atoms of the polypeptide chain (B) to the Coarse-Grained model (C) with reduced DoFs [100].

procedure. Therefore, the system is considered to a less-than-atomistic resolution, in which "beads" representing groups of atoms interact with each other. For instance, an atomistic model of a polymer contains all the atoms which are present in the real polymer. Their interactions are modelled as realistically as possible. In contrast, its coarse-grained model consists of beads which represent groups of monomers or parts thereof, or even several adjacent monomers. Interactions are only defined between these beads. They are effective interactions, as they incorporate in a mean-field way the effects of the neglected degrees of freedom. Through this operation, the number of DoFs of the system can be greatly reduced, accordingly to the size of the bead considered, which roughly correspond to the chosen loss of resolution. Fig. 1.6 reports a typical Coarse Graining procedure for a polypeptide from its atomistic representation.

The coarse-grained models level of resolution is the most commonly used in the simulation of atomic or polymeric liquids in the study of phenomena related to the slowing down of the dynamics on approaching the glass transition. Apart from the benefit of being able to simulate larger systems for longer time scales, a strong argument in favor of the coarse-graining models applied in the study of polymeric liquids is the apparent universality of the glass transition. Many phenomena related to to the slowing down of the

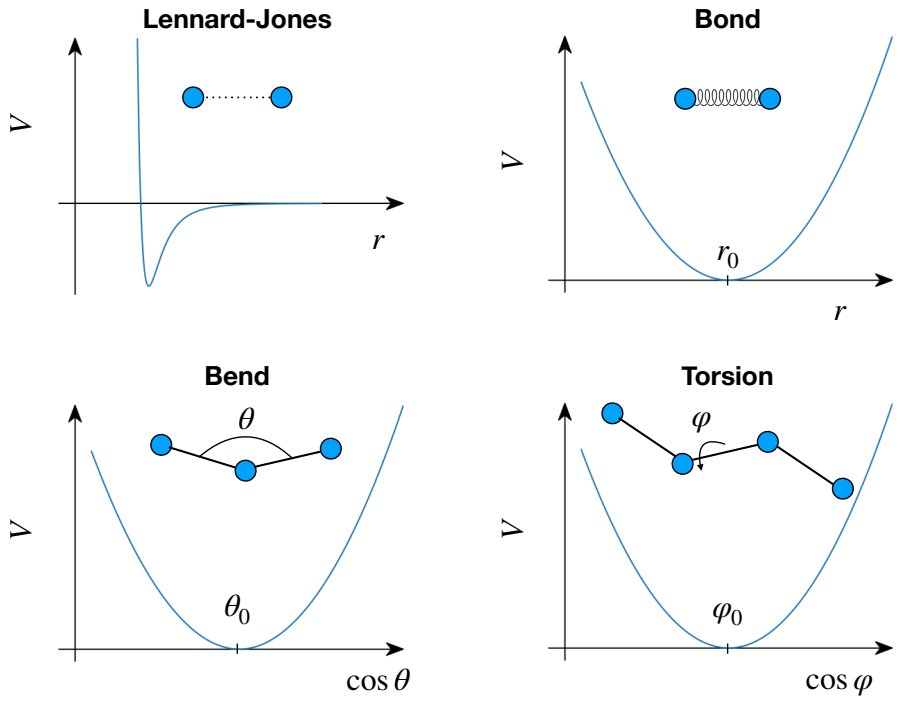

Figure 1.7: Main interactions between monomers in the model under study. The listed interactions are physically described in terms of their corresponding degrees of freedom and the typical analytical functions associated to them.

dynamics on approaching the glass transition, are not affected by the system chemical details [48]. Therefore, the implicit, but quite strong, hypothesis is that molecular and or atomic details are not needed to explain the behavior of supercooled liquids, so that the glass transition is indeed a topic for statistical mechanics, with very little influence from microscopic details.

In coarse-grained models, effective interactions are empirically designed to mimic the real counterpart of the simulated system. Usually these effective interactions are represented by analytic functions, with a set of knob adjustable parameters. In the present work a polymer is considered within the so-called *bead-spring* model. In such a model, a monomer is considered as a single interacting bead and beads are consecutively connected by bonds to form a linear polymer chain. Each couple of monomers in the system is either *bonded* or *non-bonded*. Some of the typical interaction employed in this model are schematically represented in Fig.1.7. In this work, the bond between adjacent bonded monomers in the polymeric chain is represented by

an harmonic potential

$$U^b(r) = k(r - r_0)^2 \tag{1.5}$$

depending on the distance r between the monomers with varying stiffness k and equilibrium bond length r_0. This choice is dictated to mimic the strong covalent chemical bond. Alternative choices for the bonding potential, not employed in this work, are for example the rigid bond, consisting of a constraint that binds the length of the bond to be exactly r_0, or the finitely extendible nonlinear elastic (FENE) potential [91].

Another effective potential, employed in some of the simulations of this work, is the bending potential

$$U_{bending} = k_\theta(\cos\theta - \cos\theta_0)^2 \tag{1.6}$$

where θ is the angle formed by a triplet of subsequent atoms in a chain and θ_0 is its equilibrium value (see for example Fig.1.7) introducing a chain stiffness for the simulated polymer. When the bending potential is absent the stiffness is neglected, and the chain is considered *fully-flexible*. Non-bonded monomers interact via a Lennard-Jones potential mimicking the Van der Waals interactions [25].

$$U^{LJ}(r) = \varepsilon\left[\left(\frac{\sigma^*}{r}\right)^{12} - 2\left(\frac{\sigma^*}{r}\right)^{6}\right] + U_{cut} \tag{1.7}$$

for $r \leq r_c = 2.5\,\sigma$ and zero otherwise, where $\sigma^* = 2^{1/6}\sigma$ is the position of the potential minimum with depth ε. The value of the constant U_{cut} is chosen to ensure that $U^{LJ}(r)$ is continuous at $r = r_c$ avoiding impulsive forces in that point.

When dealing with simulations, it is often useful to have a system of reduced units. A system of reduced units of measurement can be defined employing the parameters of Eq.1.7 as fundamental units. Hence the Lennard-Jones units system can be defined considering σ as fundamental length scale, ϵ as fundamental energy-scale and m, the monomer mass, as the fundamental mass-scale. Typical values for these reduced units are reported in Table 1.1 in the case of Argon [17] and of Polystyrene [93].

Once the model and the interactions are defined, proceeding with the actual simulation is straightforward. The dynamics of the system is obtained solving the equation of motion for all the particles of the system. One of the simplest method, and also the one employed for this work, is to address the problem in the Newtonian picture. Trajectories for all the particle are then obtained solving the set of equation

Physical quantity	Unit	Value for Ar	Value for PS
Length	σ	$3.4 \cdot 10^{-10}\, m$	$9.7 \cdot 10^{-10}\, m$
Energy	ε	$1.65 \cdot 10^{-21}\, J$	$6.74 \cdot 10^{-21}\, J$
Mass	m	$6.69 \cdot 10^{-26}\, Kg$	$5.8 \cdot 10^{-25}\, Kg$
Time	$(\sigma^2 m/\varepsilon)^{1/2}$	$2.17 \cdot 10^{-12}\, s$	$9 \cdot 10^{-12}\, s$
Velocity	$(\varepsilon/m)^{1/2}$	$1.57 \cdot 10^{2}\, m/s$	$1.08 \cdot 10^{2}\, m/s$
Force	ε/σ	$4.85 \cdot 10^{-12}\, N$	$6.95 \cdot 10^{-12}\, N$
Pressure	ε/σ^3	$4.20 \cdot 10^{7}\, N/m^2$	$7.38 \cdot 10^{6}\, N/m^2$
Temperature	ε/k_B	$120\, K$	$490\, K$

Table 1.1: Typical experimental values for the liquid Argon and for Polystyrene are reported compared to the reduced LJ units used in MD simulations.

$$m_i \ddot{\mathbf{r}}_i = \mathbf{F}_i \qquad , \qquad \mathbf{F}_i = -\nabla_{\mathbf{r}_i} V(\mathbf{r}_1, ..., \mathbf{r}_n) \tag{1.8}$$

This is a deterministic system of $3N$ equations, where N is the number of monomers of the system. Implementation of differential equations in computer code requires the introduction of algorithms to discretize and thus numerically integrate the equations. One of the most used is the Verlet algorithm [152, 163], chosen for its numerical stability and for beeing a symplectic integrator

$$\mathbf{r}_i(t + \Delta t) = 2\mathbf{r}_i(t) - \mathbf{r}_i(t - \Delta t) + \frac{\mathbf{F}_i(t)\Delta t^2}{m_i} + O(\Delta t^4) \tag{1.9}$$

where the Δt is the time step of the simulation. As already mentioned above Δt must be chosen small enough to produce little error in the single time step evolution, yet not too small to reduce the computational efficiency (due to the large number of operations required). After all the parameters have been chosen, the time evolution of the system is performed and quantities such as the positions and velocities of the monomers are stored at any desired time. From these informations all the dynamical or static features of the system can be 'measured' after the post-processing analysis. In this work simulations are carried out with the open-source LAMMPS [122] software. Each simulation starts from an initial random distribution for monomers positions and velocities. An initial equilibration phase is needed to decorrelate from the starting configuration and relax, if present, some non-physical local arrangement. This phase of the simulation is performed in the canonical ensemble, where the number of particle is constant and specific variables are added to the Hamiltonian of the system [112] to simulate external control on

the temperature and/or the pressure of the system, so that they can be considered adjustable parameters of the simulation. Actual measurements are then taken only after the equilibration phase. Further details on the specific preparation of each studied system is given in the next chapters.

Since the limited size of the sample (always far from the thermodynamic limit) implies accordingly large fluctuations on the studied observables, each simulation is usually repeated many times with the same thermodynamical conditions but starting from different independent initial configurations. This is done to obtain a meaningful statistical ensemble of data to average over when computing observables.

Chapter 2

An introduction to information theory

2.1 Missing information and entropy

In this manuscript, alongside usual ones, we will make use of some information theory-based observables. This kind of observables are rather new to the physics scenario. Therefore, the aim of this chapter is to give a basic introduction to this topic and also give some practical examples of their application.

As already mentioned in the previous chapter, if one knows the state of a system with N particles (all the positions and velocities are sufficient within classical mechanics) at a given time t_0 and its Hamiltonian, he is able to produce its complete temporal evolution. However, when dealing with macroscopic systems, i.e. when the number of particles N becomes very big, such a simple concept might get very complicated. In this context, writing down the Hamiltonian and solving the equation of motion becomes incredibly difficult tasks. In statistical physics this problem is generally bypassed adopting a dynamical description of the system that use a *less complete information* on it. This is usually done describing the evolution of the system as a whole considering macroscopic observables as its pressure, temperature, position, velocity of the center of mass and so on. This description implies a *lack of information* corresponding to the complete knowledge of the system microscopical state.

How to quantify this missing information? Let us consider simpler case: a discrete random variable with W equally probable outcomes. We now want to guess the outcome of a single realization of this random variable. To have a graphical representation of this problem, we can picture it as a ball hidden

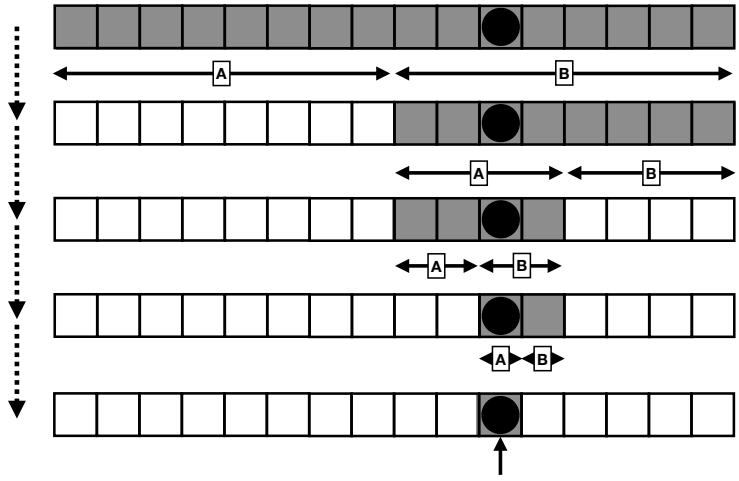

Figure 2.1: Optimal strategy to guess the position of a ball hidden in one of $W = 16 = 2^4$ boxes. The number of *yes* or *no* answers needed to locate the ball is 4.

in W identical box. How much information do we need to know exactly the position of the ball? The best strategy to quickly locate the ball is to progressively divide the system in two sets of boxes, namely A and B, and then ask "*Is the ball inside the set A?*". Whether the answer is *yes* or *no*, the number of possible states is halved down. Iterating the process, one is able to find the ball with $n = \log_2 W$ questions. Fig.2.1 illustrates a schematization of the process. If W is not a power of 2, n is the average number of questions needed to locate the ball (see Appendix A for details) [105]. We can define the missing information H as the minimum average number of *yes* or *no* questions needed locate the ball.

$$H = n = \log_2 W \tag{2.1}$$

It is worth underlying that H is exactly the amount of information which would be given when responding to the direct question *"what box is the ball in?"*. Since the nature of the questions we ask to the system is binary, the missing information is measured in *bits*. It is also conventional to find Eq.2.1 with the natural logarithm instead of the base 2 one. In that case, the missing information should be measured in *nats*. We will adopt the natural logarithm to define any information related observable. Therefore, all the information reported in this work is intended measured in *nats*.

Up until now, we considered a discrete random variable where each of the possible W outcomes comes with a probability $p = 1/W$. In the case of a

non-uniform distribution in which every outcome has a probability p_i so that

$$\sum_i p_i = 1 \tag{2.2}$$

where the summation index i runs over all the possible outcomes of the random variable, it is possible to demonstrate that Eq.2.1 must be re-cast in the form

$$H = -\sum_i p_i \log p_i \tag{2.3}$$

For the full details of this demonstration see the Appendix A.

What up until now we called missing information, within the context of *information theory*, is more properly called *entropy* of a discrete random variable[42], defined according to Shannon [141].

Information theory studies the quantification, storage, and communication of information. Originally proposed by Claude Shannon in 1948 to find fundamental limits on signal processing and communication operations, nowadays information theory not only is the keystone of coding theory but it also finds application in a huge variety of fields, ranging from mathematics and natural sciences [84, 104] to semiotics or linguistics [98].

Entropy is the fundamental measure in information theory. Quantifying the information needed to completely define a random variable, it is usually said that H, the entropy, measures its degree of randomness: the larger the entropy, the less is the a priori available information on the value of the random variable.

The concept of entropy in information theory is deeply related to the concept of entropy in statistical mechanics. The reason for this peculiar name will be discussed later in this chapter.

Let us consider, for example, a Bernoulli process. The Bernoulli random variable X, can take values 0, 1 with probabilities $p(0) = p$ and $p(1) = q = 1 - p$. According to Eq.2.3 its entropy is

$$H_X(p) = -p \log(p) - (1-p) \log(1-p) \tag{2.4}$$

and it is plotted as a function of p in Fig. 2.2. $H_X(p)$ vanishes as $p = 0$ or $p = 1$ because, as those values are approached, the process becomes more and more certain. The maximum of $H_X(p)$ is at $p = q = 1/2$ where the uncertainty of the outcome is maximal. Note that the entropy is a functional of the distribution of the given random variable. Thus it does not depend on the values taken by the variable but only on their probabilities.

For a continuous random variable, the result is similar. Let us suppose that our random variable is distributed according to a probability density

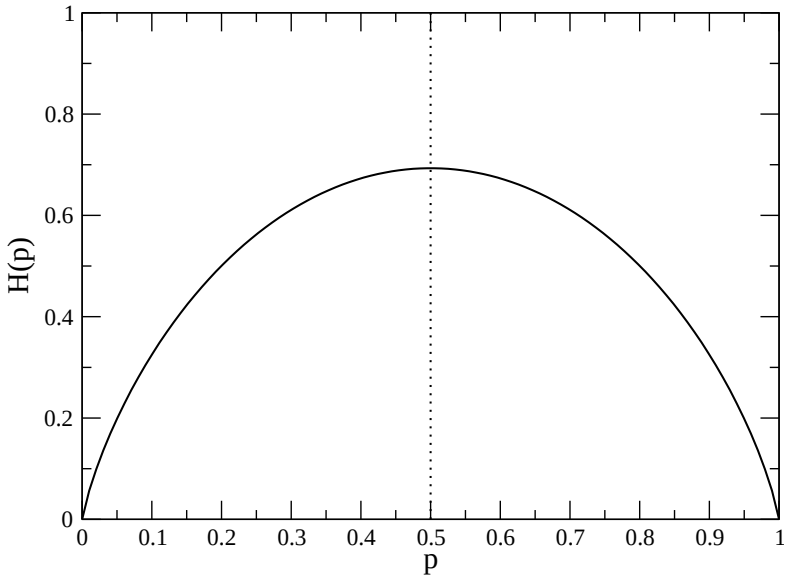

Figure 2.2: The entropy $H(p)$ of a binary variable X with $p(X = 0) = p$ and $p(X = 1) = 1 - p$, plotted versus p

function $p(x)$ within the interval $[a, b]$. The probability that the outcome of a single sampling lies between the values x_1 and x_2 is

$$W(x1, x2) = \int_{x_1}^{x_2} p(x)\, dx \tag{2.5}$$

with

$$p(x) \geq 0 \;\; \forall\, x \in [a, b] \quad \text{and} \quad \int p(x)\, dx = 1 \tag{2.6}$$

It is possible to show that in this case the entropy can be cast in the form

$$H = -\int_a^b p(x) \log p(x) \tag{2.7}$$

In this case we will speak of *continuous*, or *differential*, entropy [42]. This form may look very similar to Eq.2.3 but it actually hides some subtleties. For the full demonstration of this definition and some comments on the subtleties see the Appendix A.

2.2 Shannon entropy of an ideal gas

To get a more practical view on the *entropy* introduced in the previous section, we shall now apply those notions into a well-known physics playground: the ideal mono-atomic gas. Thus, let us consider a system of N

non-interacting, material points of mass m, confined in a volume V, with Hamiltonian

$$\mathcal{H}_0(\{\mathbf{x}_i\},\{\mathbf{p}_i\}) = \sum_{i=1}^{N} \frac{\mathbf{p}_i^2}{2m} + U(\{\mathbf{x}_i\}) \tag{2.8}$$

where U is the potential, equal for all the particles that is 0 inside the volume and ∞ outside it. The probability of finding the system in a specific state defined by the complete set of positions and momenta, $\{\bar{\mathbf{x}}_i\}$ and $\{\bar{\mathbf{p}}_i\}$, can be easily derived as

$$f(\{\bar{\mathbf{x}}_i\},\{\bar{\mathbf{p}}_i\}) = \exp\left[\Omega(\beta) - \beta\mathcal{H}_0(\{\bar{\mathbf{x}}_i\},\{\bar{\mathbf{p}}_i\})\right] \tag{2.9}$$

where $\beta = 1/k_B T$ and $\Omega(\beta)$ is

$$\begin{aligned}\Omega(\beta) &= -\log \int \{d^3x_i\}\{d^3p_i\} \exp\left[-\beta\mathcal{H}_0(\{\mathbf{x}_i\},\{\mathbf{p_i}\})\right] \\ &= -N\log V - N\log\varphi(\beta)\end{aligned} \tag{2.10}$$

being $\varphi(\beta)$ the gaussian integral over momenta

$$\varphi(\beta) = \int d^3p e^{-\beta\frac{p^2}{2m}} = \left(\frac{2\pi m}{\beta}\right)^{3/2} \tag{2.11}$$

Therefore, the Shannon joint entropy, related to the set of variables $\{\bar{\mathbf{x}}_i\}$ and $\{\bar{\mathbf{p}}_i\}$, according to Eq.2.7, is

$$H_{\{x_i,p_i\}} = -\Omega(\beta) + \beta\langle\mathcal{H}\rangle \tag{2.12}$$

where $\langle\mathcal{H}\rangle$ is the expectation value of the energy. Thus,recalling Eq.2.10, one may conclude

$$H_{\{x_i,p_i\}} = -N\log V - N\log\varphi(\beta) + \frac{3}{2}N \tag{2.13}$$

It is quite natural asking how the Shannon entropy, derived from "missing information" principles, compares to the thermodynamic one. Thus let us consider the variation of thermodynamic entropy S for our ideal gas during a reversible isothermal transformation from an initial volume V_i to a final one V_f

$$\Delta S_{\text{isothermal}} = \int \frac{\delta Q_{\text{rev}}}{T} = \frac{1}{T}\int_{V_i}^{V_f} pdV = Nk_B\log\left(\frac{V_f}{V_i}\right) \tag{2.14}$$

while for the Shannon entropy variation we have from Eq.2.13

$$\Delta H^{\text{isothermal}}_{\{x_i,p_i\}} = N\log\left(\frac{V_f}{V_i}\right) \tag{2.15}$$

Analogously, if instead we consider an isochore transformation from an initial temperature T_i to a final one T_f, according to thermodynamics we have

$$\Delta S_{\text{isochore}} = \frac{3}{2} N k_B \int_{T_i}^{T_f} \frac{dT}{T} = \frac{3}{2} N k_B \log\left(\frac{T_f}{T_i}\right) \tag{2.16}$$

and for the same transformation we have

$$\Delta H_{\{x_i,p_i\}}^{\text{isochore}} = N \log\left[\frac{\varphi(\beta_f)}{\varphi(\beta_i)}\right] = \frac{3}{2} N \log\left(\frac{T_f}{T_i}\right) \tag{2.17}$$

These comparisons lead us to conclude that the Shannon entropy is nothing but the thermodynamic one measured in *nats* (or *bits* if one instead uses $\log_2$) [105]. One *nats* of missing information correspond to a thermodynamic entropy of k_B J/K.

This is not surprising at all,in fact Eq.2.7 and Eq.2.3 are cast in the exact same form of the Gibbs definition of entropy. Despite this, the information theory entropy and the thermodynamic (statistical mechanics) one are formally different. The difference is more theoretical than actual: aside from the mismatch in the unit of measure, in the case of a thermodynamic entropy the probability density function must be specifically defined on a statistical ensemble;on the other hand it can be any distribution in the case of Shannon entropy. In this sense, Shannon entropy can be considered a generalization of the familiar concept of entropy.

2.3 Correlated variables and mutual information

In the case of multiple, discrete or continuous, random variables say X and Y distributed according to the joint probability distribution $p(x, y)$, it is possible to extend the definition of entropy Eq.2.3 and Eq.2.7 obtaining

$$H(X, Y) = -\sum_{x \in \mathcal{X}} \sum_{y \in \mathcal{Y}} p(x, y) \log p(x, y) \tag{2.18}$$

the *joint entropy* for a discrete random variable, where $\mathcal{X}$ and $\mathcal{Y}$ are the sets of all possible values (*alphabeth*) of X and Y respectively, and

$$H(X, Y) = -\int_{\mathcal{X}} \int_{\mathcal{Y}} p(x, y) \log p(x, y) \tag{2.19}$$

the *continuous* or *differential joint entropy* for a continuous random variable.

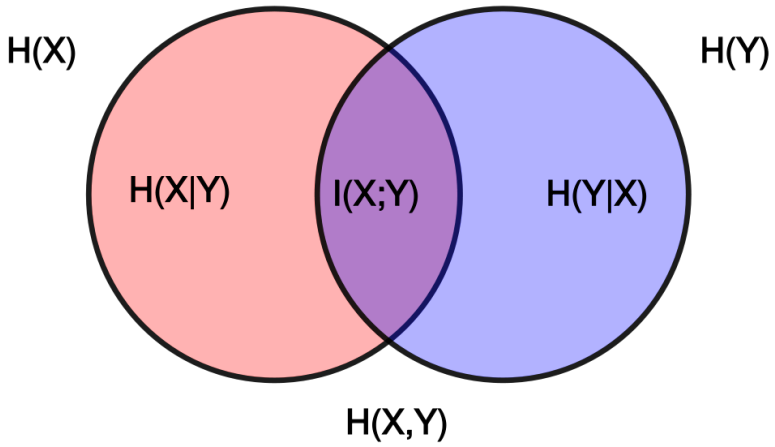

Figure 2.3: Graphical representation of Eq.2.20. Here the two circles are the individual Shannon Entropies $H(X)$ and $H(Y)$. Mutual Information is represented as the intersection of the two circles. The two non-overlapping parts of the circles represent the conditional entropies.

There is nothing really new in these definitions, since (X, Y) can be considered in both the cases to be a single vector-valued random variable. From both of the definitions Eq.2.19 and Eq.2.18, it follows immediately that, if X and Y are independent, the joint entropy simply boils down to the sum of individual entropies.

If instead X and Y are somehow correlated, the joint entropy deviates from the naive sum. The difference is known as Mutual Information (MI) between X and Y, $I(X, Y)$ and quantify the reduction in randomness of a variable knowing the outcome of the other

$$I(X, Y) = H(X) + H(Y) - H(X, Y) \tag{2.20}$$

A graphical representation of this relation is given in Fig.2.3. An alternative expression for the MI between discrete variables can be obtained replacing Eq. 2.3 in Eq. 2.20

$$I(X, Y) = \sum_{x \in \mathcal{X}} \sum_{y \in \mathcal{Y}} p(x, y) \log \left[\frac{p(x, y)}{p(x)p(y)} \right] \tag{2.21}$$

or for two continuous variables, Eq. 2.7 in Eq. 2.20

$$I(X, Y) = \int_{\mathcal{X}} \int_{\mathcal{Y}} dx\, dy\; p(x, y) \log \left[\frac{p(x, y)}{p(x)p(y)} \right] \tag{2.22}$$

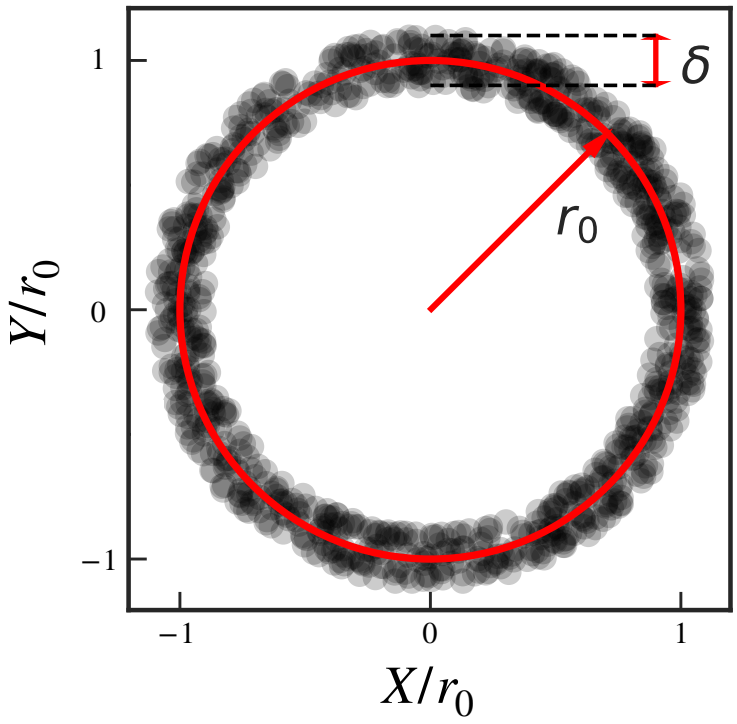

Figure 2.4: A toy model to understand the usefulness of the mutual information. Joint distribution of a sample of size $N = 1000$ of two continuous random variables X ad Y both limited in the interval $[-1, 1]$.

Quantifying the mistake made considering two random variables as independent, MI can be thought of as a measure of general correlation between the two variables. Unlike the *Pearson correlation coefficient*, defined as

$$C(X,Y) = \frac{\langle (x - \langle x \rangle)(y - \langle y \rangle) \rangle}{\sigma_X \sigma_Y} \tag{2.23}$$

where σ_X is the standard deviation of X, MI does not require the dependence to be linear in order to be detected [97]. There are many examples in which the Pearson correlation coefficient is zero but the variables are manifestly stochastically dependent. An example of this is reported in Fig.2.4. X and Y are two random variables that are uniformly distributed on an annulus of mean radius r_0 and thickness δ. As the ratio δ/r_0 is decreased the dependence of the two variables grows stronger and appears clearly. If however, one tries to measure the correlation between X and Y employing naively the Pearson correlation coefficient $C(X,Y)$ the outcome would be 0 for any δ/r_0, as depicted in Fig2.5. On the other hand, MI detect immediately the dependence and gives a sharp response for $\delta/r_0 \to 0$. For the Pearson correlation

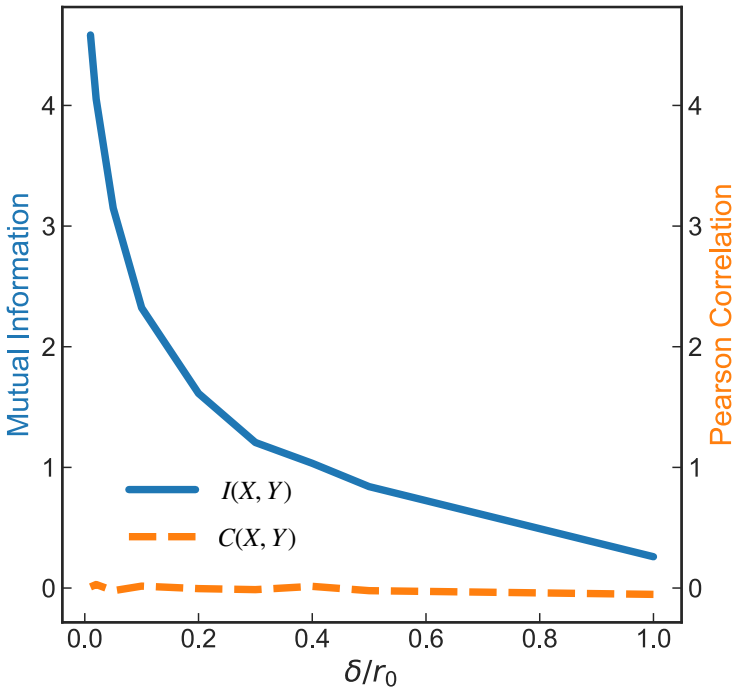

Figure 2.5: Comparison of the performance between the Pearson correlation coefficient $C(X,Y)$ and the mutual information $I(X,Y)$. Despite the fact that for small values of δ/r_0 a pattern in the joint distribution is obvious, a naive linear correlation is completely featureless in detecting it. On the other hand, the mutual information identify immediately and quite sharply the correlation between the two variables.

coefficient to detect the stochastic dependence, if it is non-linear, one needs to have some information about the expected kind of order. As an example, if one consider a distribution like the one in Fig.2.4 and measure the Pearson correlation coefficient between the variable X^2 and Y^2, for a small enough δ/r_0, one obtains $C(X,Y) \approx 1$. In all the cases in which an order agnostic approach is required (or at least preferable), MI is a more powerful and reliable tool for detecting stochastic dependence. Nevertheless, it must be said that this sensitivity comes with a cost. In fact, while the Pearson correlation coefficient can be estimated directly from a data sample even if the probability distributions of the variables are not known, MI requires knowledge of these distributions. If these are not known, their estimation is a very delicate (and sometimes uncertain) procedure. For this reason, the estimation of the MI requires a much higher computational cost compared to the one of a Pearson correlation coefficient computation. A few example of MI estimators are given in Appendix B.

The use of MI, as well as other information theory observables, founds its origins in communication and coding theory [42, 104]. However, lately its use has been extended employed also in physics due to its sensibility to non-linear correlation. For instance, MI has been used for detecting classical phase transitions for several classical system and topological transition in the XY model [82], the phase transition in a 2D disordered Ising model [147] and for evaluating the configurational entropy of liquid metals [66].

Soft matter physics, in particular, offers a promising ground to look at with the glass offered by MI as it is abundant in scenarios where often the expected "order" is not known and the possibility of non-linear effects between observables is quite remarkable. Therefore, in the works presented in this thesis, investigations carried out are based on or flanked by MI measures. In particular, in the first part of this thesis, MI has been employed as a measure of correlation between particles displacements in simple molecular liquids (trimers). In the second part of the thesis, MI has been used as an alternative, more sensitive, measure for detecting the presence of secondary relaxations in a slightly more complex liquid of long polymers (25-mers).

Chapter 3

Displacements correlations as sensed by mutual information

3.1 Research context

The nature of the solidification process observed at the glass transition (GT) temperature T_g by cooling supercooled viscous liquids is a topic of intense research [31, 45]. Starting with the seminal paper by Adam and Gibbs, who conjectured the presence of *cooperatively rearranging regions* in viscous liquids [2], there has been an increasing interest in identifying possible growing length scales as mobility decreases [87]. A broad classification in terms of either static or dynamic length scales is usually used. The free energy landscape determines static (thermodynamic) length scales, whereas dynamic length scales are set by the rules governing the system dynamics. These are extracted from finite-time behavior of time-dependent correlation functions and associated susceptibilities. Even if growing static length scales have been reported by experiments [4] and simulations [33], there is still debate if they control the glass transition [168]. On the other hand, the discovery of the spatial inhomogeneity of the dynamics in supercooled liquids, the so-called dynamic heterogeneity, revealed that more and more particles move in a correlated way, approaching T_g from above, and promoted the study of their characteristic dynamical length scales. It is still not clear to what extent dynamic correlations are the consequence or the primary origin of slow dynamics [87].

In this chapter, we investigate dynamic spatial correlations detected by mutual information (MI). In the framework of liquid-state physics MI has already been considered in *atomic* glass-formers as metric of the correlation between structural and dynamical quantities [55, 56, 83]: in particular the

propensity [56, 83]. Propensity refers to particle displacements starting from the same initial global configuration and is a tool to investigate the possible link between structure and dynamics [166].

In this work, we adopted the scheme of Ref. [56] and investigated by molecular-dynamics (MD) numerical simulations the propensities MI correlations in space and time of a model *molecular* glass-former. As a major result, we found *no growing dynamical correlations* on slowing down the microscopic mobility. This finding is strikingly different with respect to the outcomes of MI studies of atomic glass-formers where a clear *increase* has been reported [56].

3.2 Models and methods

We performed molecular dynamics (MD) simulations of fully-flexible, i.e. with no bond-bond bending potential, linear chains of trimers ($M = 3$) in the supercooled regime. All simulations were carried out with the open-source software LAMMPS [1, 122]. Non-bonded monomers interact with a truncated version of the Lennard-Jones potential introduced in Eq.1.7

$$U^{LJ}(r) = \epsilon \left[\left(\frac{\sigma^*}{r} \right)^{12} - 2 \left(\frac{\sigma^*}{r} \right)^{6} \right] + U_{cut}(r) \tag{3.1}$$

where $\sigma^* = 2^{1/6}\sigma$ is the location of the potential minimum which has depth ϵ. U_{cut} is chosen to ensure $U^{LJ}(r) = 0$ for any $r > r_{cut}$ and r_{cut} is set to the value of 2.5σ. Bonded monomers interact with each other via the harmonic potential

$$U^{b}(r) = k\,(r - r_0)^2 \tag{3.2}$$

where the constant k is set to $555.5\epsilon/\sigma^2$ and the rest length of the bond is $r_0 = 0.97\sigma$. All quantities are in reduced units: length in units of σ, temperature in units of ϵ/k_B and time in units of $\sigma\sqrt{m/\epsilon}$ where m is the monomer mass [96]. We set $m = k_B = 1$. The time step for the integration was chosen to be 0.003. All the investigated systems have $N = 3999$ monomers, i.e. 1333 chains.

The NVT (canonical) ensemble has been used for the equilibration runs. Temperature has been controlled via a Nosé-Hoover thermostat[79, 112]. For each run, the equilibration time lasted not less than $3\tau_{ee}$, where τ_{ee} is the end to end vector autocorrelation function decay time [7, 8, 21, 49]. After equilibration, the NVE (microcanonical) ensemble was employed for the data production employing at least sixteen independent runs. We built three sets of states varying both the density ρ and temperature T, each state being

characterized by the pair (ρ, T): set A = $\{A_1, A_2\}$ with A_1= (1.05, 0.60), A_2= (1.01, 0.47); set B = $\{B_1, B_2\}$ with B_1=(1.03, 0.49), B_2= (1.01, 0.435); set C = $\{C_1, C_2\}$ with C_1=(1.02, 0.42), C_2= (1.05, 0.51). The states of the same set exhibit the same relaxation time τ_α, i.e. $\tau_\alpha^{(A)} \simeq 42$, $\tau_\alpha^{(B)} \simeq 150$, $\tau_\alpha^{(C)} \simeq 1550$. The exact definition of the relaxation time will be given in Sec.3.3. The estimated glass transition temperature for this model, at pressure $p = 1$, is $T_g \approxeq 0.4$[139]. The correction to this estimate due, to the pressure difference (in this work the pressure ranges from 0.4 up to 4), is approximately $\Delta T \approx 0.01$[28].

From the equilibrated configuration of each state, in parallel to the usual production runs in the NVE ensemble, we also started production runs in the iso-configurational ensemble (ICE) [166]. Each ICE, henceforth labeled by μ, consists of a single initial spatial configuration of all the particles, each of them starting the time evolution with 1000 random assignments of the initial velocity, as drawn from the corresponding Maxwell-Boltzmann distribution of the state. We considered four ICEs for the states of the set C and two ICEs for the other two sets, in close agreement with other studies performed with about three times fewer particles than the present one [56]. The initial configurations of the ICEs were randomly taken by the set of NVE production runs. The reduced number of ICEs compared to the number of production runs in the NVE ensemble is due to the extremely time-consuming procedure to perform the MI evaluation. Arguments will be presented in Sec.3.3 to conclude that the phase space explored by all the ICEs of a single state is indistinguishable from the one explored by all the NVE runs. If the distribution functions which are involved in the MI definition (Eq.2.22) are unknown, one has to resort to complex estimators to perform the MI evaluation. Following previous studies [56, 83], we employed the Kraskov-Stögbauer-Grassberger estimator [90] (for full details on this estimator see Appendix B). The high number of velocity assignments in each ICE ensures proper convergence of the estimator.

We point out that two different kinds of averages are adopted in the present work: i) the usual ensemble average over the NVE ensemble to be denoted as $\langle X \rangle_{NVE}$. In the absence of any ambiguity, the NVE subscript is understood; ii) the average $\langle X \rangle_{ICEs}$, namely the average over the different velocities and all the monomers in a single ICE followed by the average over all the ICEs, i.e. all the initial configurations. Even if the two averages yield virtually indistinguishable results in the present study, i.e. $\langle X \rangle \simeq \langle X \rangle_{ICEs}$ within the errors, given the conceptual difference, it seems proper to distinguish between them. This notation will result a bit overabundant in this chapter while it will be necessary for Chapter 4.

3.3 Results and discussion

3.3.1 Relaxation and transport

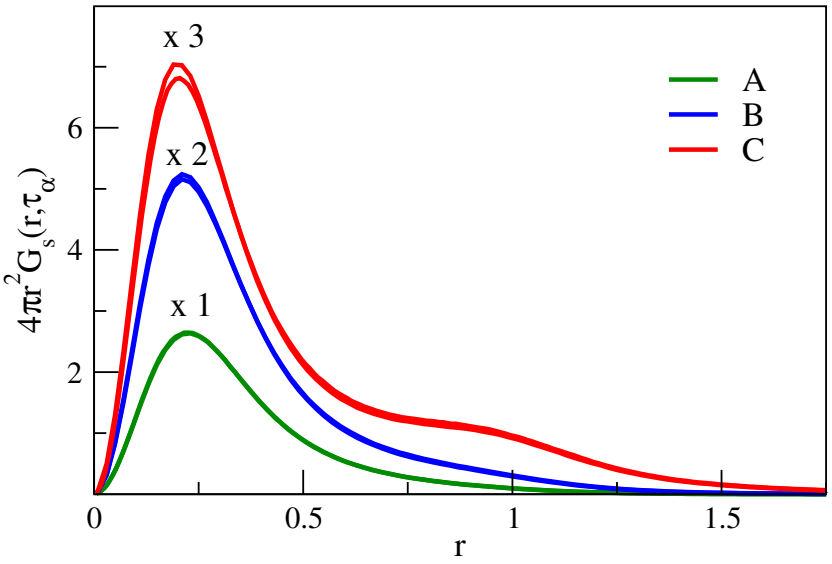

Figure 3.1: Self-part of the van Hove function $G_s(r, \tau_\alpha)$, Eq.3.3. The structural relaxation time τ_α is defined by means of the decay of the ISF (see text and Fig.3.3 for all the details). The states of the C set reveal a marked bimodal structure of the van Hove function function signalling patent heterogeneous dynamics.

We first characterize the relaxation and the mobility of the molecular liquid. One central quantity is the self part of the van Hove function $G_s(\mathbf{r}, t)$ [77]:

$$G_s^{(k)}(\mathbf{r}, t) = \frac{1}{N} \left\langle \sum_{i=1}^{N} \delta \left[\mathbf{r} + \mathbf{r}_i(0) - \mathbf{r}_i(t) \right] \right\rangle_k , \; k = NVE, ICEs \tag{3.3}$$

where $\mathbf{r}_i(t)$ is the position of the i-th monomer at time t and the brackets denote the average over the system replicas. In isotropic liquids the van Hove function depends on the modulus r of $\mathbf{r}$. The interpretation of $G_s(r, t)$ is direct: the product $G_s(r, t) \cdot 4\pi r^2$ is the probability that the monomer is at a distance between r and $r + dr$ from the initial position after a time t.

The second moment of the van Hove function is the mean square displacement (MSD):

$$\langle \delta r^2(t) \rangle_k = \frac{1}{N} \sum_{j=1}^{N} \left\langle ||\mathbf{r}_j(t) - \mathbf{r}_j(0)||^2 \right\rangle_k , \; k = NVE, ICEs \tag{3.4}$$

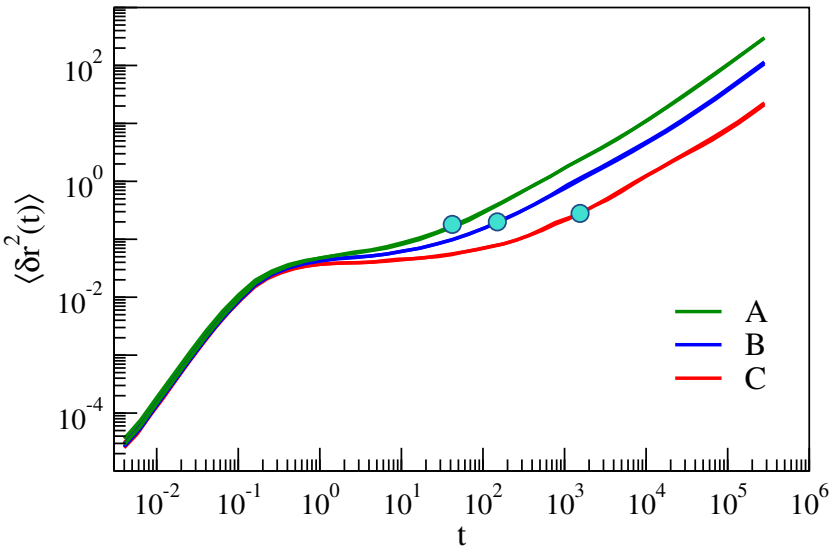

Figure 3.2: Monomers mean square displacement, Eq.3.4. Note that, if two ISF (Fig.3.3) and MSD curves coincide at short time ($t \sim 1$), they do the same up to τ_α at least. This is a manifestation of the known universal scaling between the fast vibrational dynamics and the long-time relaxation in viscous liquids [95, 131]. See text for details.

The spatial Fourier transform of the self part of the van Hove function yields the self part of the intermediate scattering function (ISF) [77]:

$$F_s^{(k)}(\mathbf{q},t) = \frac{1}{N}\sum_{j=1}^{N}\left\langle e^{i\mathbf{q}\cdot[\mathbf{r}_j(t)-\mathbf{r}_j(0)]}\right\rangle_k,\ k = NVE, ICEs \tag{3.5}$$

which in an isotropic liquid depends only on the modulus of the wavevector $q = ||\boldsymbol{q}||$. ISF provides a convenient relaxation function to study the rearrangements of the spatial structure of the fluid over the length scale $\sim 2\pi/q$. We define the structural relaxation time τ_α by the relation $F_s(q_{max}, \tau_\alpha) = e^{-1}$ where q_{max} is the maximum of the static structure factor (for the present study $7.14 \leq q_{max} \leq 7.22$).

Fig. 3.1 presents the self-part of the van Hove function $G_s(r,t)$ evaluated at τ_α of the three sets of states, computed within the NVE ensemble. It is seen that states with equal τ_α (the sets A, B, C) have coinciding $G_s(r,\tau_\alpha)$. This is a well-known property proven also in completely different systems [124, 130]. Most monomers displace by half a radius, $r \sim 0.25$. The states of the set C also exhibit a secondary peak at $r \sim 1$ (the monomer diameter) due to the presence of fast particles with jump dynamics, revealing strong heterogeneous dynamics [44].

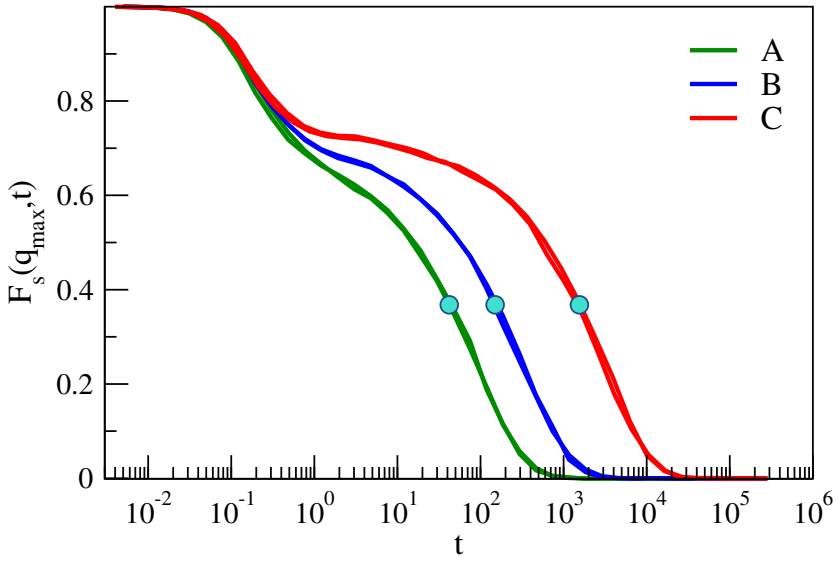

Figure 3.3: Intermediate scattering function, Eq.3.5, at q_{max}, the first peak of the static structure factor, of the six studied states. ISFs are groupable in three distinct pairs. The relaxation time τ_α of each pair is marked by a dot.

Fig.3.3 shows the monomer ISF of all the states under investigation. To better understand the relaxation process, the monomer MSD is also reported in Fig.3.2. ISF and MSD curves reported in Fig.3.3 and are computed within the NVE ensemble. The coincidence of the ISF and MSD curves of states belonging to the same set, over all the investigated time window will be commented at the end of the present Sec.3.3.1. At very short times (ballistic regime) MSD increases according to $\langle r^2(t)\rangle \cong (3k_BT/m)t^2$ and ISF starts to decay. At later times, the repeated collisions with the other monomers slow down the displacement of the tagged one, resulting in a quasi-plateau region, found in both MSD and ISF curves, progressively more marked as the temperature is lowered and/or the density increased. This signals the increased caging of the particle. The latter is released by the cage after an average time τ_α, leading to the ISF decay and the MSD increase due to diffusive motion for $t \gtrsim \tau_\alpha$. Fig.3.4 shows the NVE non-gaussian parameter (NGP) defined as:

$$\alpha_2^{(k)}(t) = \frac{3\langle \delta r^4(t)\rangle_k}{5\langle \delta r^2(t)\rangle_k^2} - 1,\ k = NVE, ICEs \tag{3.6}$$

$\alpha_2(t)$ vanishes if the displacement r is gaussian. It is a well-known metric of the dynamical heterogeneity, featuring the non-gaussian character of the displacements [31, 45, 132]. It is seen that the maximum of $\alpha_2(t)$ increases

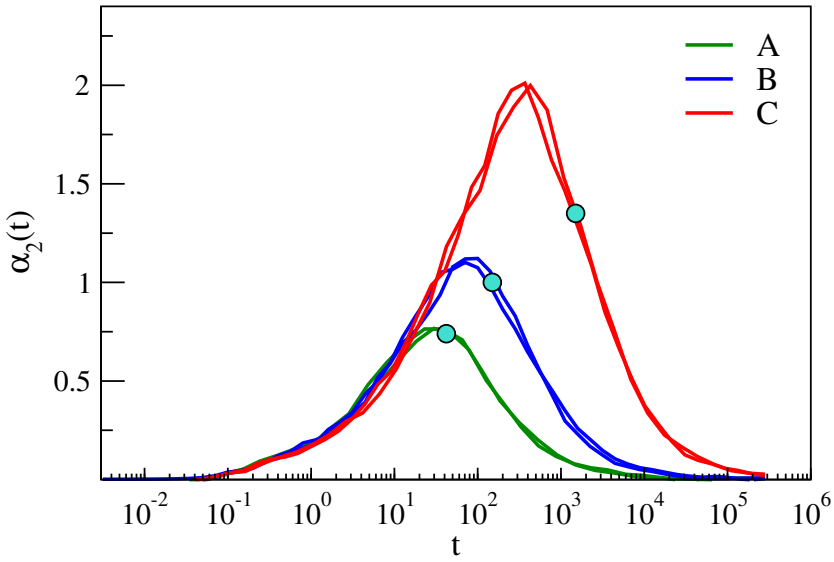

Figure 3.4: Non-gaussian parameter (NGP) of the six selected states. As ISF, MSD and Van Hove, NGP curves are groupable in three set. A dot marks the position of the structural relaxation time τ_α of each set.

with the relaxation time and states with equal relaxation time has virtually identical $\alpha_2(t)$ [95, 115]. The increasing peak height of $\alpha_2(t)$ proves that the states have significantly different dynamical heterogeneity.

It is worth noting that the six investigated states are designed to emphasize the noted universal scaling between the fast vibrational dynamics and the long-time relaxation in viscous liquids [24, 76, 95, 131]. The scaling states that, considering any ensemble-averaged time-dependent quantity $X(t)$, if two physical states exhibit equal value of $X(t)$ at very short times ($t \sim 1$, corresponding to a few picoseconds [93]), the time evolution of $X(t)$ in the two states is the same up to τ_α at least. Fig.3.3, Fig.3.2 and Fig.3.4 illustrate the scaling for ISF, MSD and NGP by showing that their curves, referring to six different states, are groupable in three separate pairs, each labeled by a specific τ_α value. The scaling also holds for the van Hove function [124, 130] and explains the grouping of the curves in Fig.3.1. In Chapter 4, the robustness of this scaling in the framework of MI correlations in the isoconfigurational ensemble will be also investigated.

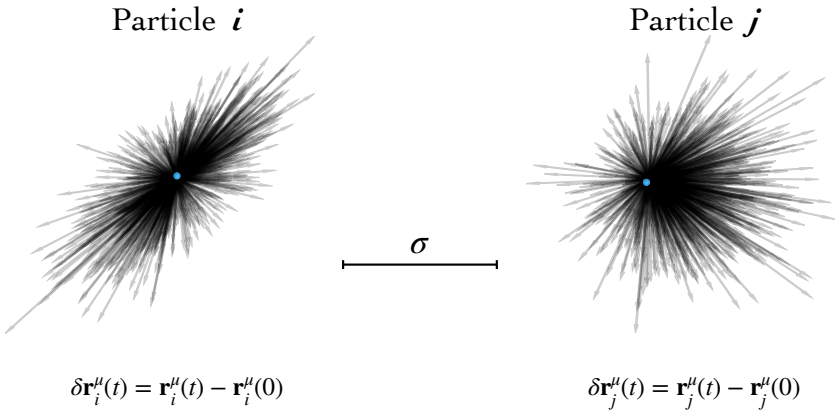

Figure 3.5: Pictorial 2D representation of the displacement distribution of a particle pair (i, j) for $t \simeq \tau_\alpha$. Every arrow is a displacement form the initial position (marked by a blue dot) computed considering the trajectory originated from a single random assignment of the initial velocity.

3.3.2 Mutual Information

Global distribution

In an iso-configurational ensemble μ, we considered the distribution of the i-th particle displacement at a given time t from the starting configuration

$$\delta\mathbf{r}_i^\mu(t) = \mathbf{r}_i^\mu(t) - \mathbf{r}_i^\mu(0) \tag{3.7}$$

where $\mathbf{r}_i^\mu(0)$ is the position of the i-th particle in the selected ICE starting configuration. Within the ICE, $\delta\mathbf{r}_i^\mu(t)$ can be considered a random variable whose realizations depends on the random assignment of the initial velocity. Hence, we can measure the statistical dependence between the displacements distributions of a particles pair (i, j), computing the MI $I_{ij}^\mu(t)$, evaluated, according to Eq.2.7, by the relation

$$I_{ij}^\mu(t) = \int_{\delta\mathbf{r}_i^\mu \in \Xi_i^\mu} \int_{\delta\mathbf{r}_j^\mu \in \Xi_j^\mu} p(\delta\mathbf{r}_i^\mu(t), \delta\mathbf{r}_j^\mu(t)) \log \frac{p(\delta\mathbf{r}_i^\mu(t), \delta\mathbf{r}_j^\mu(t))}{p(\delta\mathbf{r}_i^\mu(t))p(\delta\mathbf{r}_j^\mu(t))} \tag{3.8}$$

where Ξ_i is the set of all the possible displacement of the i-th particle in the selected ICE, $p(\delta\mathbf{r}_i^\mu(t))$ and $p(\delta\mathbf{r}_i^\mu(t), \delta\mathbf{r}_j^\mu(t))$ are respectively the marginal and the joint probability distribution. By measuring the mutual information between these displacement distributions, we obtain a value for the strength of the correlation in displacement of each pair of particles in the system as a function of time. Fig.3.6 presents representative plots of the distribution $p(I^\mu, t)$ of the MI values at time t for a single ICE of the liquid. Therefore,

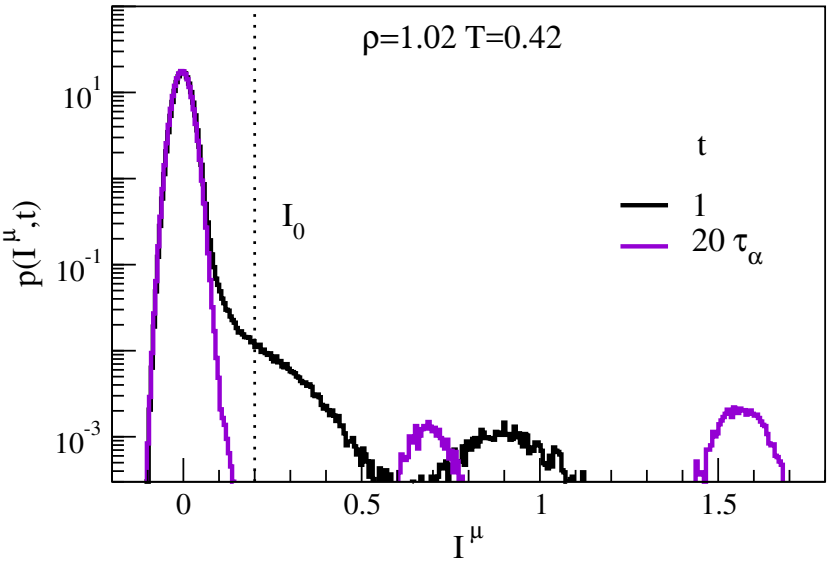

Figure 3.6: Representative plots of the MI distribution at time t for a single ICE of a selected state of the C set. The threshold $I_0 = 0.2$ above which MI values are considered significant [56] is also indicated.

$p(I^\mu, t)dI^\mu$ is the probability that the MI between two particles at time t is located in the range $[I^\mu, I^\mu + dI^\mu]$. The particles i and j are said to be correlated at time t if $I^\mu_{ij}(t) > I_0$ with $I_0 = 0.2$. The threshold value I_0 has been chosen in agreement with other studies [56] to filter out the contributions at small MI values where the MI estimator is less reliable [90]. Fig.3.6 shows that for $t \ll \tau_\alpha$ the distribution $p(I^\mu, t)$ exhibits a multi-modal structure above I_0 which develops as two well-separated peaks at $t \gg \tau_\alpha$. The two peaks stem from the permanent bonds linking a monomer to the other two present in the trimer, establishing permanent MI. Preliminary runs show that nine peaks are seen in decamers at long times. The multi-modal structure of $p(I^\mu, t)$ is missing in atomic liquids [56] because of the absence of bonds, limiting the reciprocal arrangement of any given pair of particles and thus establishing correlation in the displacements at long times.

In Fig.3.7 is reported the evolution of the distribution of the number of particles correlated to a central one at time t, $p(n, t)$, for the same state considered in Fig.3.6. In a time $t \sim 1$, the monomer hits the surrounding cage a few times [29]. The collisions trigger MI-correlations with a rather limited number of particles and $p(n, t)$ peaks at very small n values. As time goes by, the distribution displaces at larger n values for $t < \tau_\alpha$ due to the rapid exploration of the cage by the central particle establishing MI-correlations with a larger number of surrounding neighbors. For $t > \tau_\alpha$, following the

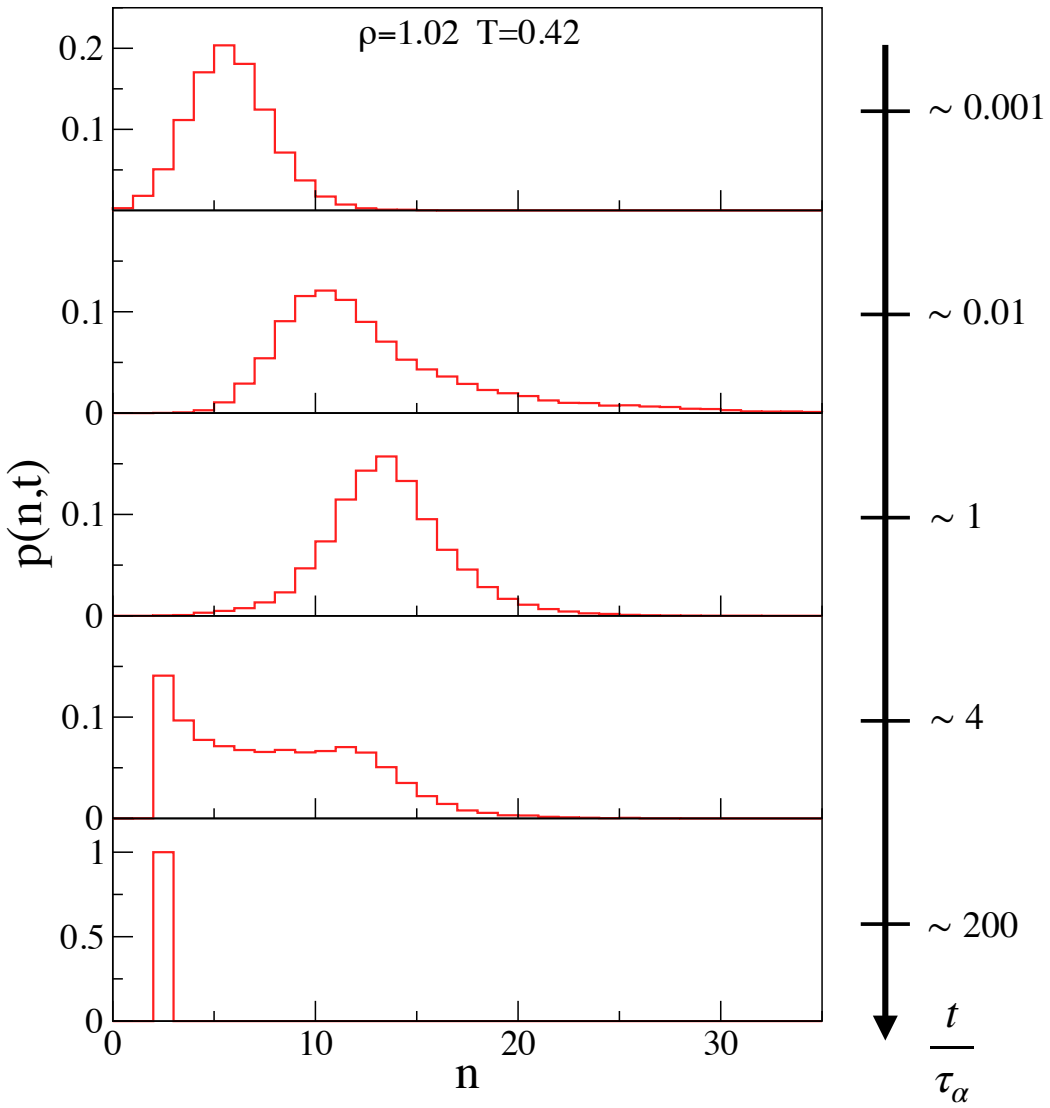

Figure 3.7: Probability that a central particle is MI-correlated with n surrounding ones at time t for the same state of Fig.3.6, exhibiting a relaxation time $\tau_\alpha^{(C)} \sim 1550$. The probability is averaged over all ICEs.

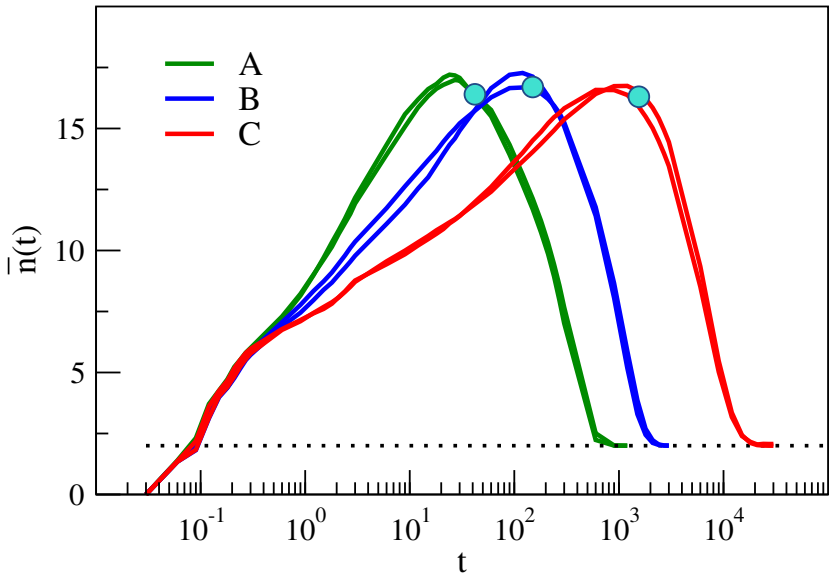

Figure 3.8: Time-dependence of the average number of particles correlated with a central one $\overline{n}(t)$. Color codes as in Fig.3.1. States with equal relaxation time, marked by dots, exhibit coincident time dependence of $\overline{n}(t)$and $R_g(t)$ (reported in Fig.3.9), thus supporting the universal scaling between the fast vibrational dynamics and the long-time relaxation in viscous liquids [76, 95, 131].

cage disappearance and the larger displacements (see Fig.3.3 and Fig.3.2), the MI-correlated particles decrease. For $t \sim 4\tau_\alpha$ the distribution exhibits a notable change of the shape with a clear bimodal structure. Similar behavior has been also reported in *atomic* liquids [56]. For $t \gg \tau_\alpha$ the distribution narrows and peaks at about $n \sim 2$, corresponding to the fact that in a molecule each particle has permanent correlations with two other monomers.

The present and the following chapter will deal with the characteristic of the distribution $p(n)$ in order to understand its time dependence and its behavior with the typical timescale of the system, τ_α. In this chapter we will focus on the average, keeping track of the distribution mean position and ignoring any peculiar behavior of the tails. On the other end, nn Chapter 4, we will focus on the standard deviation characterizing the width of the distribution and, therefore, keeping a close watch on its tails.

In Fig.3.8 plots $\overline{n}(t)$, the average number of correlated particles with a central one. Another variable to observe along with $\overline{n}(t)$ is the average distance between correlated particles, namely the gyration radius $R_g(t)$ [56], reported in Fig.3.9. The latter gives the mean size of the region of correlated displacement. Notably, states with *equal* relaxation time exhibit, within the errors, the *same* time dependence of $\overline{n}(t)$ and $R_g(t)$ in the whole range, cov-

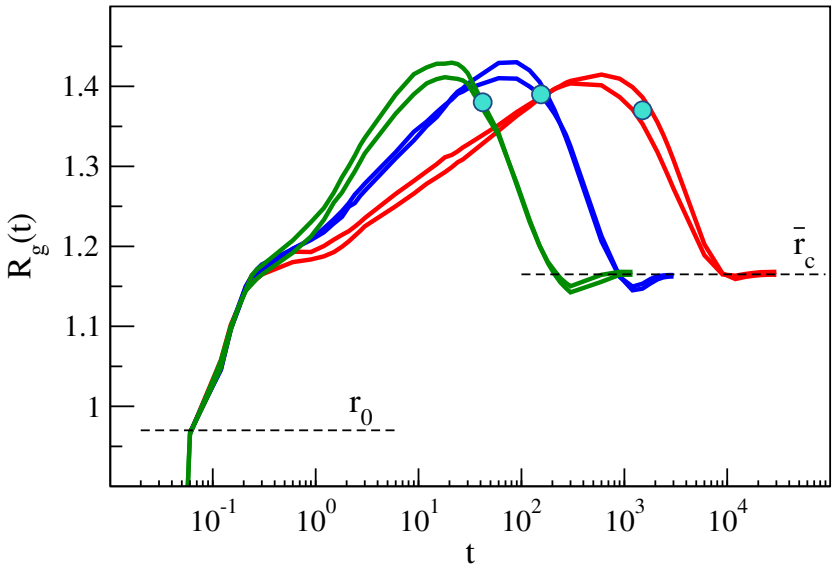

Figure 3.9: Time-dependence of the gyration radius of the clusters of correlated particles $R_g(t)$ [56]. r_0 and $\overline{r}_c$ denote the bond length and the average distance between the monomers belonging to the same molecule, respectively. Dots mark the position of the structural relaxation time τ_α

ering both vibrational and relaxation time scales. We interpret this finding as a manifestation of the aforementioned scaling between the fast vibrational and the slow dynamics in glassforming systems [24, 76, 95, 131]. Fig.3.8 shows that the average $\overline{n}(t)$ vanishes at short times indicating that correlation in the displacement are entirely caused by collision with neighbors. During the cage regime $\overline{n}(t)$ grows rapidly, peaking at $t \sim \tau_\alpha$ when on average the particles escape from the surrounding cage and start decorrelating from the original neighbors. $\overline{n}(t)$ eventually reaches at long time the plateau level corresponding to the fact that in a molecule each particle has permanent correlations with two other monomers. The gyration radius mimics the behavior of $\overline{n}(t)$. It starts at very short times at $R_g \sim r_0$, i.e. the bond length, and levels off at long times at the plateau $\overline{r}_c$, corresponding to the average distance between the monomers of a molecule, as evaluated by, e.g., the intrachain radial distribution function [30].

Fig.3.8 and Fig.3.9 show a central finding. It can be seen how a change in the relaxation time by a factor of ~ 40 does not change the maxima of the two metrics of the spatial correlations, i.e. the average number of correlated particles with a central one $\overline{n}(t)$ and the gyration radius R_g. This is in striking contrast with the behavior of atomic liquids where the maxima of both $\overline{n}(t)$ and R_g are seen to increase with the structural relaxation time

[56]. We have checked that changing I_0 in the range $0.1 \leq I_0 \leq 0.3$ does not affect this finding.

Intermolecular and intramolecular distribution

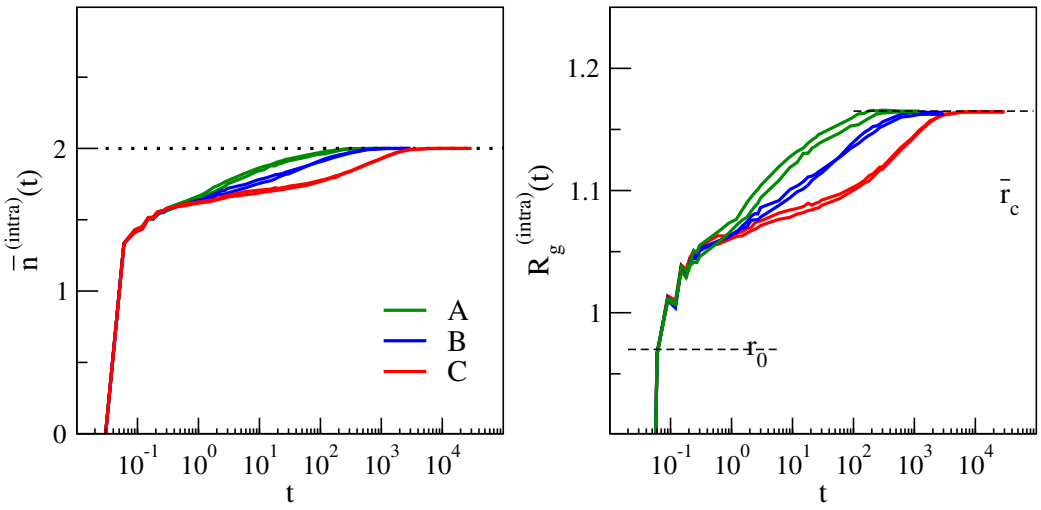

Figure 3.10: Left panel: time-dependence of the average number of particles correlated with a central one $\overline{n}(t)$ belonging to the same chain. Right panel: time-dependence of the gyration radius of the clusters of correlated particles $R_g(t)$ [56] among the ones in the same chain. r_0 and $\overline{r}_c$ as in Fig.3.8.

Fig.3.10 and Fig.3.11 provide further insight into the time evolution of the distribution of the correlated particles to a central one belonging respectively to the *same* molecule or *other* molecules. As before, we focus on the average and the gyration radius, i.e. the average distance between correlated particles. They are referred to as $\overline{n}^{(x)}(t)$, and $R_g^{(x)}(t)$ for intramolecular ($x = intra$) and intermolecular ($x = inter$) correlations, respectively. Fig.3.10 shows that the average number of correlated particles belonging to the *same* molecule grows with *two* distinct regimes. A *fast* increase, developing within $t \sim 1$, corresponding to the full exploration of the surrounding cage by the monomer [95], and a much *slower* growth to reach the asymptotic level, 2, which completes within the structural relaxation time τ_α. The gyration radius increases qualitatively above the bond length value, r_0, to reach the same asymptotic value of the global gyration radius, see Fig.3.8. Fig.3.11 refers to the correlation between a monomer and other ones belonging to *different* molecules. It is seen that the time evolution of the average number of correlated particles belonging to *different* molecules, $\overline{n}^{(inter)}(t)$, behaves qualitatively like the global average $\overline{n}(t)$ for $t \lesssim \tau_\alpha$. In particular, the maximum

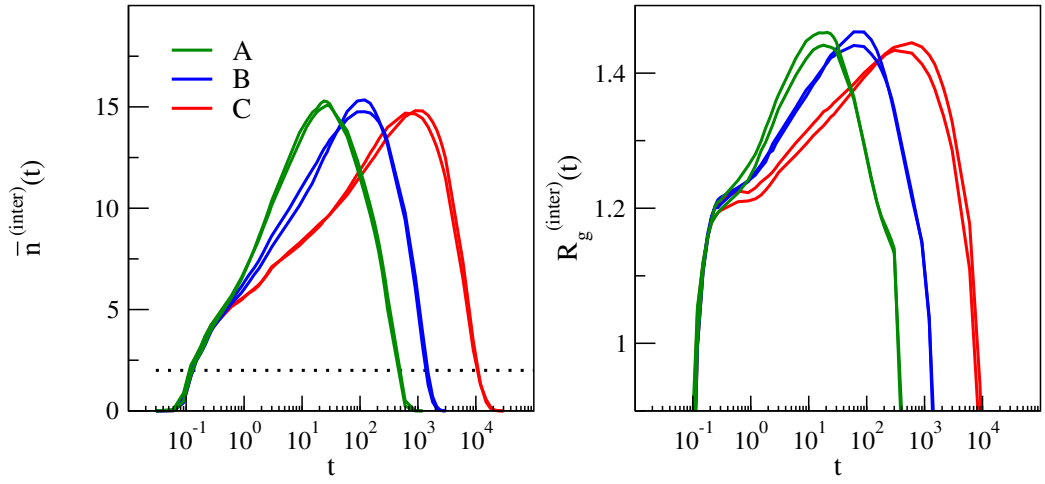

Figure 3.11: Left panel: time-dependence of the average number of particles correlated with a central one $\overline{n}(t)$ belonging to different chains. Right panel: time-dependence of the gyration radius of the clusters of correlated particles $R_g(t)$ [56] excluding the ones belonging to the same chain of the central.

value of $\overline{n}^{(inter)}(t)$, reached close to $t \sim \tau_\alpha$, does *not* increase by increasing the structural relaxation times and one has $\overline{n}^{(inter)}(\tau_\alpha) \simeq \overline{n}(\tau_\alpha) - 2$. This approximate relation points out that most particles correlate to a monomer belonging to a *different* molecule. Consistent with the latter finding, a near coincidence between the global and the intermolecular gyration radiuses is also observed $R_g^{(inter)}(t) \simeq R_g(t)$ for $t \lesssim \tau_\alpha$, including their maximum value. At long times, differently from $R_g(t)$, $R_g^{(inter)}(t)$ vanishes since the central particle has no permanent correlations with the ones of other molecules.

Molecular center-of-mass distribution

Instead of considering the molecular liquid as a collection of N monomers, we may picture it in a coarse-grained way as a collection of $N/3$ point particles, each localized at the molecular center of mass. The MI distribution between the molecular centers of mass is a subject of interest to investigate the MI correlations at the molecular level going beyond the local fast modes internal to the molecule itself. It could be also as a useful tool to compare the MI correlations of our monodisperse molecular liquid with the reported ones of polydisperse atomic liquids [55, 56, 83].

Fig.3.12 plots the average number $\overline{n}^{(cm)}(t)$. One can see how, as as in the case of $\overline{n}(t)$ (see Fig.3.8), the maximum of $\overline{n}^{(cm)}(t)$, does not increase by increasing the relaxation time. Notably, the maximum occurs at a time earlier than τ_α, which is close to - but not coincident with - the time where

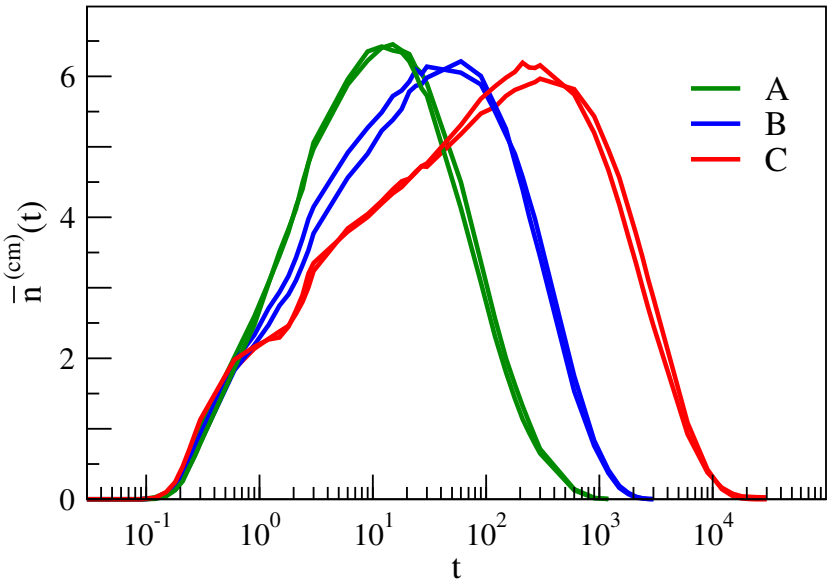

Figure 3.12: Time-dependence of the average number of center-of-mass correlated with a central one according to MI ($\overline{n}^{(cm)}(t)$). States with equal relaxation time exhibit coincident time dependence of $\overline{n}^{(cm)}(t)$ over all the time window, supporting the universal scaling between the fast vibrational dynamics and the long-time relaxation.

the maximum of the non-gaussian parameter, $\alpha_2(t)$, is located (see Fig.3.4).

Dynamical correlation lengths

To better scrutinize the previous finding, Fig.3.13 plots the average MI at τ_α between the central particle and a surrounding one at r distance for all the states under investigation. Apart from a mild modulation, in-phase with the radial distribution function, only a weak dependence on the state is seen, consistently with Fig.3.8. The slope ξ_I of the exponential tail in a log-lin plot provides a measure of the MI correlation length [56]. This parameter is reported as a function of τ_α in Fig.3.14. It is possible to observe that ξ_I increases very weakly on approaching GT (about 8.5% to be compared with $\sim$ 30% in atomic liquids in nearly the same range of relaxation time values [56]), in agreement with the findings of Fig.3.8 and Fig.3.13

It is interesting to compare the MI correlation lengths ξ_I with the spatial correlation lengths of the scalar and the vector displacement-displacement correlations. To this aim, we define the following correlation functions: [127,

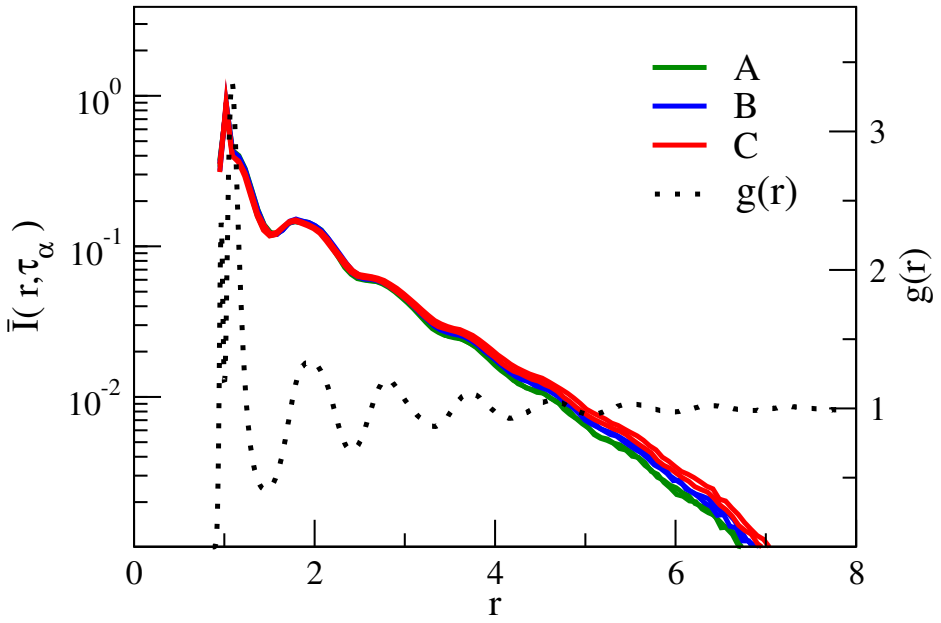

Figure 3.13: Average mutual information at τ_α between the central monomer and a surrounding one at r distance for all the states under investigation. The slope of the exponential tail defines the MI correlation length ξ_I.. Color codes as in Fig.3.8. The dotted line is the radial distribution function (negligibly state-dependent). The sharp peak at $r \sim r_0 \sim 0.97$ is due to bonded particles.

128]

$$C_{\vec{u}}(r,t) = \langle \hat{\mathbf{u}}_i(t_0,t) \cdot \hat{\mathbf{u}}_j(t_0,t) \rangle, \tag{3.9}$$

$$C_{\delta u}(r,t) = \frac{\langle \delta u_i(t_0,t) \delta u_j(t_0,t) \rangle}{\langle [\delta u(t_0,t)]^2 \rangle}. \tag{3.10}$$

An average over all the i-th and j-th monomers spaced by r is taken for granted. $\hat{\mathbf{u}}_k(t_0,t)$ is the versor of the displacement of k-th monomer in a time interval from t_0 to t_0+t, to be defined as:

$$\mathbf{u}_k(t_0,t) = \mathbf{r}_k(t_0 + t) - \mathbf{r}_k(t_0) \tag{3.11}$$

whereas the deviation from the displacement modulus average of the of k-th monomer in the same time interval is defined as:

$$\delta u_k(t_0,t) = |\mathbf{u}_k(t_0,t)| - \langle |\mathbf{u}(t_0,t)| \rangle \tag{3.12}$$

On increasing r, both $C_{\vec{u}}(r,\tau_\alpha)$ and $C_{\delta u}(r,\tau_\alpha)$ exhibit an exponential tail with slopes $\xi_{\vec{u}}$ and $\xi_{\delta u}$ in a log-lin plot, respectively [127, 128].

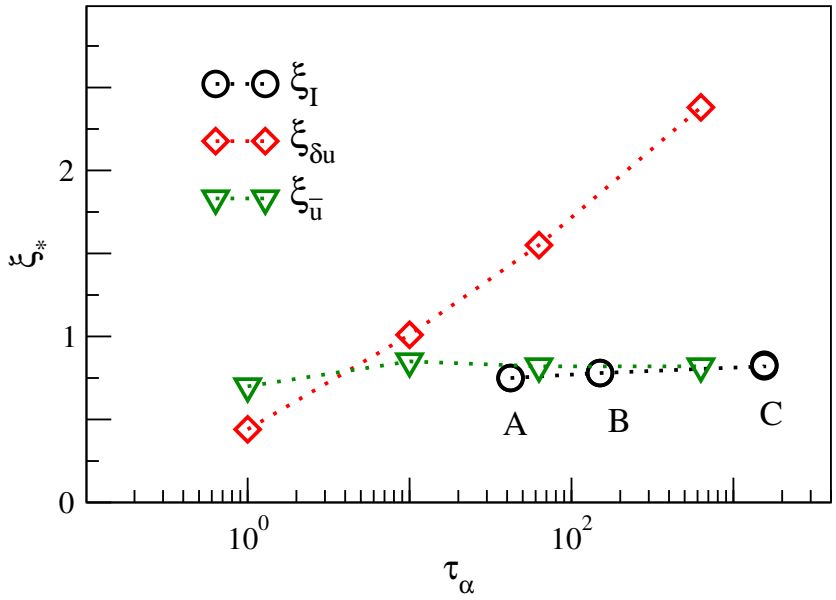

Figure 3.14: MI correlation lengths ξ_I superimposed to the ones of the modulus ($\xi_{\delta u}$) and the direction ($\xi_{\bar{u}}$) of the particle displacement in the NVE ensemble [127, 128]. Error bars are smaller than the symbol size.

Fig.3.14 shows that $\xi_I \sim \xi_{\bar{u}}$, i.e. the MI length is rather close to the one of the direction, whereas it is rather decoupled from the one of the magnitude of the displacement which exhibits a significant increase with τ_α. The predominance of the displacement directional correlation in the MI behavior could be explained by some sort of insensitivity of the measure to displacement modulus correlation. Such an insensitivity might derive directly from the MI computation. The fact that Eq.2.22 is invariant under affine changes supports this idea. As a consistency test, we have found that Eq.3.8 is invariant under the global scale change $\delta\vec{r}_k^{\,\mu}(t) \to \lambda\delta\vec{r}_k^{\,\mu}(t)$.

Another explanation could be that the MI-correlation of the displacement modulus is weaker and/or it decorrellates faster as compared to the displacement direction. This might be due to the ICE method itself in which the initial velocity random assignment could further undermine displacement moduli correlations. In fact, a recent study[19] showed that the Pearson correlation coefficient between particle displacement moduli in the ICE is rather low (average correlation $\lesssim 0.24$ at the nearest-neighbor distance even for the slowest investigated systems) indicating a fairly poor correlation. To control this aspect, we computed the MI directly between particle displacement moduli. The observed MI values were found to be of the same order as the estimator noise and therefore they were not considered significant. This could

mean that a more considerable numerical effort might be necessary for being able to detect a meaningful particle displacement moduli MI-correlation and to see its contribution to the overall MI-length scale.

3.4 Conclusions

We study by MD simulations the transport and the relaxation of a model molecular liquid in the NVE and the isoconfigurational ensembles by changing considerably *both the molecular mobility and the degree of dynamical heterogeneity*. We find that the time evolution of the MI spatial correlations complies with the scaling between the fast vibrational dynamics and the long-time relaxation. We focus on the MI correlation length which is observed to increase in atomic liquids on approaching the glass transition. We evidence that the MI correlations between monomers are largely due to inter-molecular correlations. We also find that, considering the liquid as a collection of monomers, the MI correlation length is weakly dependent on the structural relaxation time and virtually coincident with the length scale of the particle displacement direction correlation. Adopting the coarse-grained picture of the molecular liquid as a collection of point particles localized at the molecular centers of mass also leads to an alternative MI correlation length being nearly constant. Our findings suggest that the characteristics of the MI length scale are markedly system-dependent and pose the question about whether they can capture the key features of the dynamical heterogeneity and other quasi-universal aspects of fragile glassformers.

The findings of the investigation reported in this chapter have been published in the journal Soft Matter [160].

Chapter 4

Scaling of the heterogeneous dynamics

4.1 Research context

On approaching the glass transition, trapping effects due to the cage formed by the first neighbors are more and more prominent. The average escape time, i.e. the structural relaxation time τ_α, increases from a few picoseconds up to thousands of seconds. Particles are not completely immobilized by the surrounding cages but they wiggle in it with mean-square amplitude $\langle u^2 \rangle$ on the picosecond time scale $t^\star$. As already stated in Chapter1, being strictly related to the Debye-Waller (DW) factor, we will refer by synecdoche to $\langle u^2 \rangle$ as DW factor, too.

Despite the huge range of time scales, earlier [156] and later studies, both theoretical [12, 58, 76, 102, 108, 109, 169] and experimental [35], addressed the rattling process within the cage to understand the structural relaxation, rising a growing interest in the DW factor role [24, 34, 131, 148, 165, 167, 171]. In particular, correlations between DW factor and structural relaxation are found in bulk [95, 124, 129] and thin films [24] polymers, binary atomic mixtures [116, 130], colloidal gels [43], antiplasticized polymers [121, 144], water [113] and water-like models [73, 80]. DW factor also provided an alternative interpretation of the so-called thermodynamic (or temperature/density) scaling [123]. The correlation between structural relaxation and DW factor has been inspected in the experimental data concerning several glassformers in a wide range of fragility -considering the steepness index m defined by Angell [10] - ($20 \leq m \leq 191$), including polymers, van der Waals and hydrogen-bonded liquids, metallic glasses, molten salts and the strongest inorganic glassformers. The correlation is summarized by the universal master

curve [95, 131]:

$$\log \tau_\alpha = \mathcal{F}_{DW}(\langle u^2 \rangle) \tag{4.1}$$

$$= \alpha + \tilde{\beta}\left(\frac{\langle u_g^2 \rangle}{\langle u^2 \rangle}\right) + \tilde{\gamma}\left(\frac{\langle u_g^2 \rangle}{\langle u^2 \rangle}\right)^2 \tag{4.2}$$

$\langle u_g^2 \rangle$ is the DW factor at the glass transition. An analytical derivation for this relation, in the framework of the Hall-Wolynes model, is presented in Appendix C. It is worth mentioning the existence of alternative forms of Eq. 4.2; for example, Douglas and coworkers developed a localization model predicting the alternative master curve $\mathcal{F}_{DW}(\langle u^2 \rangle) \propto \langle u^2 \rangle^{-3/2}$ relating the structural relaxation time and the DW factor [53, 121, 144].

Further studies revealed that the master curve, Eq.4.1, is a manifestation of a more intimate correlation between the vibrational dynamics and the slow relaxation. Such a relation may be presented in the following terms. Let us consider a generic space- and time-dependent quantity $X(\mathbf{r}_1, t_1, \mathbf{r}_2, t_2)$ where $\mathbf{r}$ denotes a configuration of the liquid at a given time t, i.e., the set of all the positions of the elementary microscopic particles. For steady states $X(\mathbf{r}_1, t_1, \mathbf{r}_2, t_2)$ depends only on the time difference $t = t_2 - t_1$. Hence, let us set $t_1 = 0$ and define $X(\mathbf{r}_0, 0, \mathbf{r}_2, t) = X(\mathbf{r}_0, \mathbf{r}, t)$. If two states, have the same DW factor, the correlation function evaluated over the two states, has coincident time evolution, at least between the typical vibrational time scale $t*$ and τ_α. In other words, for $t^* \lesssim t \lesssim \tau_\alpha$ at least, it holds

$$\langle u^2 \rangle_{(1)} = \langle u^2 \rangle_{(2)} \;\Rightarrow\; X(\mathbf{r}_0, \mathbf{r}, t)_{(1)} = X(\mathbf{r}_0, \mathbf{r}, t)_{(2)} \tag{4.3}$$

In selected systems Eq.4.3 extends up to even longer times, for example in atomic binary mixtures and unentangled polymers where the diffusive regime is covered as well [124, 125, 129, 130]. Eq.4.3 has been tested for the intermediate scattering functions, mean square displacement, non-gaussian parameter [95, 117, 118, 130], van Hove function [124], transient elasticity [126] and displacement-displacement correlation functions [127, 128].

The role of the vibrational dynamics has been noted in systems with *heterogeneous dynamics*, namely glassformers close to the glass transition [125, 127–129] where the Stokes-Einstein relation fails [125, 129] and thin films with strong mobility gradient [24]. In these systems, distinct DW factors are found in regions with different relaxation and transport at *long* times. Other studies addressed vibrational dynamics (even if considered at a slightly longer time scales than vibrational one) to provide insight into the structural origin of long-time dynamic heterogeneity [165–167].

In this chapter, such a subject is considered from the point of view of the Mutual Information. In particular, we investigate the behavior of the standard deviation of the distribution $p(n, t)$, presented in the previous chapter,

focusing on dynamic heterogeneity related aspects. We recall that $p(n,t)$ is the probability, evaluated by considering all ICEs, that a generic central particle is MI-correlated with n surrounding ones at time t. Therefore the standard deviation of $p(n,t)$ is a measure of how heterogeneous in size are the regions of correlated motion. We will see how this measure can be associated with the propensity distribution at the same time t.

In particular, we investigate if: i) both the master curve Eq.4.2 and Eq.4.3 hold in the regions with different DW factors and relaxation partitioning the overall system and ii) there are structural signatures, especially at short times $t \sim t^*$, of the long-time dynamic heterogeneity. As to the latter aspect, we profit from previous studies on the local geometry and collective extended excitations driving the moves of a particle in the cage of its neighbors in dense liquids [29].

4.2 Results and discussion

4.2.1 Quantities of interest

In this chapter, we make use of the quantities reported in Chapter 3. In particular we will consider ISF, defined by Eq.3.5, and MSD, defined by Eq.3.4. It is important to stress the fact that we adopted two different kinds of averages: i)the familiar ensemble average over the NVE ensemble ii) the average over the random reassignment of initial velocities and over the starting spatial configuration.

In addition to the quantity of interest described in Chapter 3, we define the Debye-Waller factor $\langle u^2 \rangle$ as the MSD at t^* [95]:

$$\langle u^2 \rangle = \langle \delta r^2(t^*) \rangle \tag{4.4}$$

A proper choice of t^* is set by the position of the inflection point of MSD which for the present model is nearly constant, $t^* \simeq 1$ [95], corresponding to a few picoseconds [93].

Fig.4.1 gives a more detailed point of view of Fig.3.2. Particular emphasis has been given to the position of the structural relaxation time τ_α, the value of t^*, and the DW factor $\langle u^2 \rangle$. Fig.4.1, Fig.3.3 and Fig.3.4 offer, for the three pairs of states having equal DW factors, an example of the correlation between the DW factor and the long-time relaxation, that is Eq.4.3 with the identification $X = MSD, ISF, NGP$.

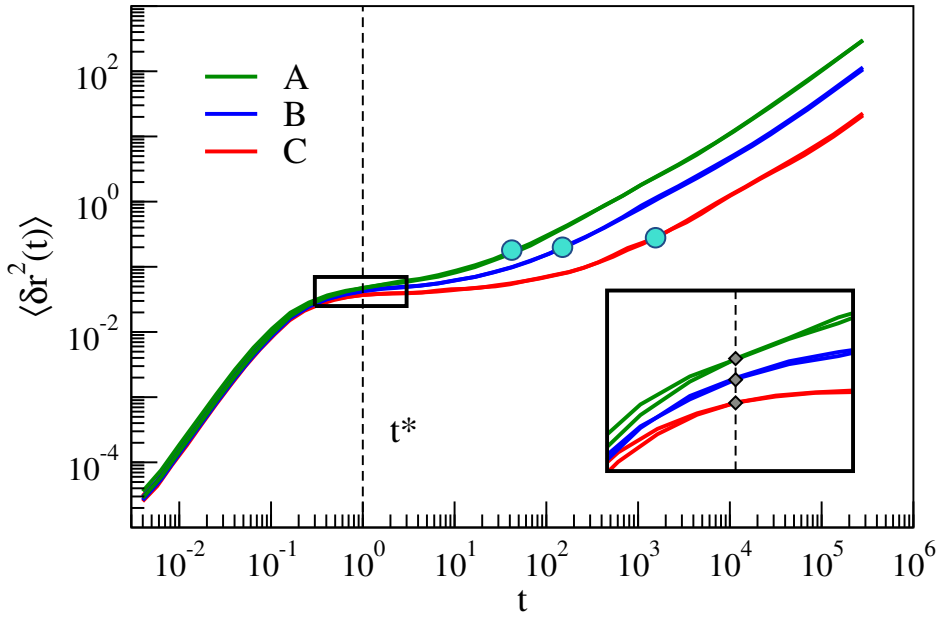

Figure 4.1: A more detailed view of Fig.3.2. Mean square displacement (MSD) of the six states of the present study. Inset: enlargement of the region inside the box, around t^*. The ordinate of the intersection (marked by gray diamonds) of the MSD curves with the (dashed) line $t = t^*$ is the DW factor $\langle u^2 \rangle$ of each given set. The initial difference, appreciable for $t < t^*$, between MSD curves of states of the same set, is due to the temperature difference among them.

4.2.2 Standard deviation of the number of MI-correlated particles

In the previous chapter, by means of the MI between particles, we computed $p(n,t)$, the distribution of the number of MI-correlated particles at a given time t. Fig.4.2 plots two characteristic parameters of the distribution $p(n,t)$, i.e. the average $\overline{n}(t)$ (top panel) and the standard deviation $\sigma(t)$ (bottom panel). As mentioned in Chapter 3, the average number of particles which are MI-correlated with a generic one, $\overline{n}(t)$, offers a measure of the average size of correlated regions at time t, whereas the standard deviation suggests how broad is the size distribution. The time dependence of the average, $\overline{n}(t)$, has been already discussed and interpreted in the previous chapter. Conversely to $\overline{n}(t)$, the behavior of the standard deviation, $\sigma(t)$, is rather complex. It peaks at two different times indicating the presence of two characteristic time scales other than τ_α: namely τ_{early} and τ_{late}. On increasing τ_α, these two characteristic time scales get longer but in a different way: τ_{early} exhibits the weaker increase and gets away from τ_α where τ_{late} approaches the latter.

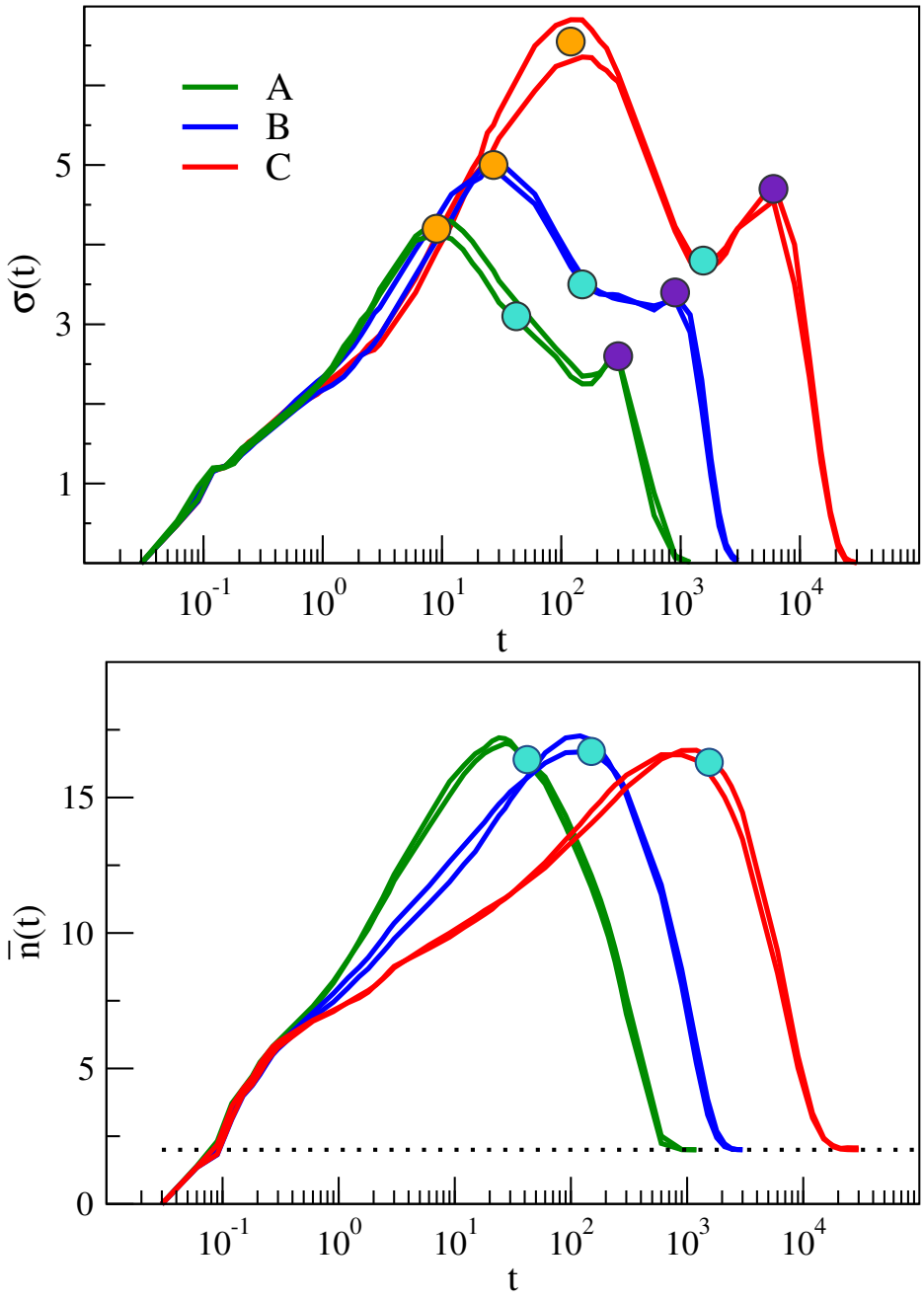

Figure 4.2: Top: time-dependence $\sigma(t)$, the standard deviation of the number of particles which are MI-correlated with a generic one. Note that the pairs of states belonging to the same set A, B, C exhibit the same behavior of both $n(t)$ and $\sigma(t)$. Sky-blue dots mark the position of τ_α. The two peaks of the standard deviation identify two time scales which are referred to as τ_{early} (orange dot) and τ_{late} (violet dot) also reported in atomic liquids [56]. Bottom: $\bar{n}(t)$, the average number of particles which are MI-correlated with a generic one, plotted for a direct comparison.

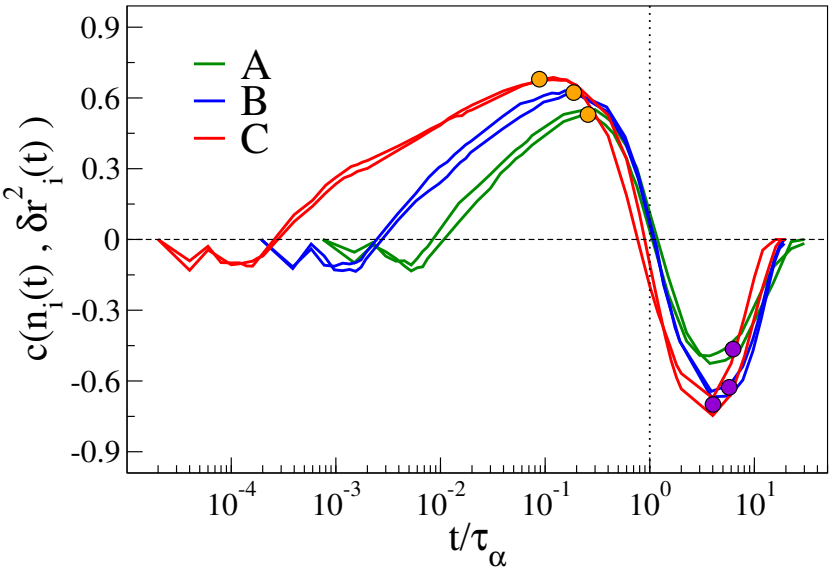

Figure 4.3: Pearson correlation between the number of MI-correlated particles around the generic i-th particle at time t and its propensity at the same time. Orange and violet dots mark τ_{early} and τ_{late}, respectively, as defined in Fig.4.2 (right).

The complex pattern of the standard deviation is close, but *not* identical, to the one observed in atomic liquids [56]. A remarkable difference is that in our molecular liquid the peak at τ_{early} grows in height on increasing τ_α and the ratio between the heights of the peaks at τ_{early} and τ_{late} is fairly constant. Instead, in atomic liquids the peak at τ_{early} is absent for states with fast relaxation ($\tau_\alpha \lesssim 10$) and grows more than the peak at τ_{late} when the relaxation slows down [56]. As a last remark about Fig.4.2 we note that the pairs of states with *equal* DW factor, and then equal relaxation time, exhibit the *same* dependence of $\overline{n}(t)$ and $\sigma_n(t)$ from very fast to slow time scales. We interpret the finding as novel support to the general validity of Eq.4.3.

In order to characterize the monomers on the basis of the number of their MI-correlated particles, we investigated the Pearson correlation coefficient $c(n_i(t), X)$, where $n_i(t)$ and X are the number of MI-correlated particles with the generic i-th monomer at time t and X is the quantity of interest. Beyond an average over all the monomers, the coefficients are also averaged over all the initial configurations. First, we consider the Pearson correlation between $n_i(t)$ and the propensity at the same time, i.e. the square displacement of the i-th particle in a time t starting from the initial configuration. Fig.4.3 plots the related time evolution. It is seen that the Pearson correlation is

maximum at $t \approx \tau_{early}$ and minimum at $t \approx \tau_{late}$. This clearly indicates that the monomers with a higher number of surrounding MI-correlated particles than the average have higher mobility than the average at short times ($t < \tau_\alpha$) and lower mobility at longer times. This finding suggests the existence of two modes of relaxation with different mobility: an high mobility mode with characteristic time scale $\sim \tau_{early}$ and a low mobility mode with characteristic time scale $\sim \tau_{late}$. This conjecture is further developed and substantiated in the next section. Notably, the time dependence of the correlation coefficient is the same in each pair of states with the same DW factor and relaxation time in agreement with Eq.4.3.

4.2.3 Early and late-relaxing fractions

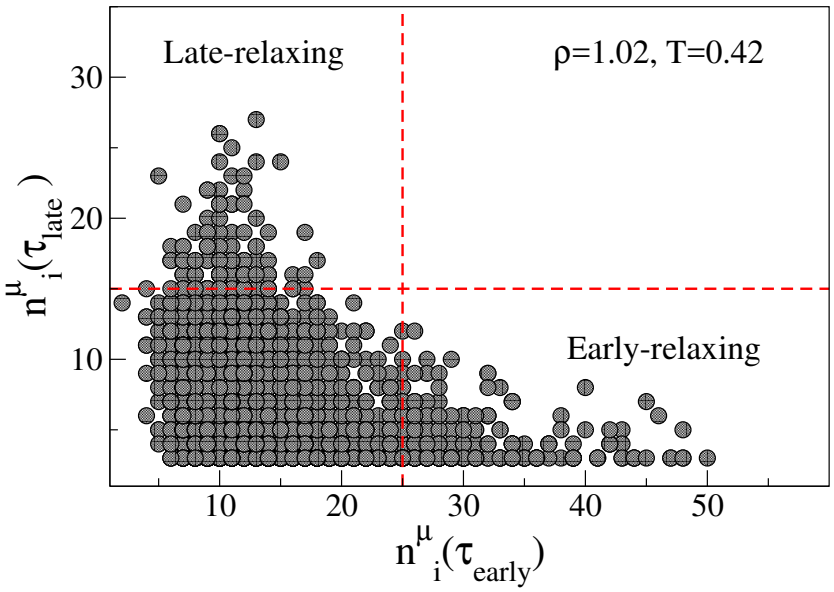

Figure 4.4: Correlation plot between the number of MI-correlated particles surrounding the i-th particle at times τ_{early} and τ_{late}, respectively $n_i^\mu(\tau_{early})$ and $n_i^\mu(\tau_{late})$ $(i = 1, \cdots, N)$. The definition of τ_{early} and τ_{late} is given in Sec.4.2.2 and shown in Fig.4.2. The red dashed lines are positioned at the average value of $n_i^\mu(t)$ plus two times the standard deviation. They divide the plot in four sectors. Particles falling in the lower-right sector and upper-left sectors are said *early*- and *late*-relaxing, respectively. When moving from τ_{early} to τ_{late}, an early-relaxing particle decreases the number of MI-correlated particles, whereas - with rare exceptions - a late-relaxing particle does the opposite.

In the previous section, we concluded that particles showing an high number of correlated partners at $t \approx \tau_{early}$ tend to be the ones with higher mo-

bility at the same time, while particles with an high number of correlated partners at $t \approx \tau_{late}$ tend to be the ones with lower mobility at the same time. To gain further insight, it is possible to look directly at the dynamics of particles presenting a number of correlated partners n in the tail of the distribution $p(n,t)$ for $t = \tau_{early}$ and $t = \tau_{late}$.

Fig.4.4 presents, for a single ICE of the state C_1 (the same shown in fig.3.6), the correlation plot of the number of correlated particles surrounding the i-th particle at times τ_{early} and τ_{late}, respectively $n_i^\mu(\tau_{early})$ and $n_i^\mu(\tau_{late})$, for all the monomers $i = 1, \cdots, N$. A similar pattern is found in atomic liquids [56] and, in close analogy, we focused our attention on the two fractions of monomers exhibiting the largest number of MI-correlated particles. More precisely, the two fractions are formed by the monomers with a number of correlated particles exceeding the average value of $n_i^\mu(\tau_{early})$ and $n_i^\mu(\tau_{late})$ by two times the standard deviation. Such a severe criterion is chosen to ensure as little as possible contamination from the normal particles population (i.e. with close to average correlated particles at both times) while maintaining a reasonable number of particles in the two fractions. The two population will be referred to as *early*- and *late*-relaxing particles, respectively. Early-relaxing particles exhibit high number of correlated partners at $t = \tau_{early}$ *decreasing* at the longer time τ_{late}. Late-relaxing particles do the opposite, i.e. they exhibit a low number of correlated partners at $t = \tau_{early}$ *increasing* at τ_{late}.

Fig.4.5 characterizes the early-relaxing and late-relaxing monomers for the two states with slower relaxation (set C). Similar features are seen for the A and B groups of states. The top and bottom panel of Fig. 4.5 show ISFs and MSDs, respectively, restricted to the early- and late-relaxing populations and compare them to the global curves considering all the monomers. It is seen that early-relaxing particles exhibit faster relaxation and higher mobility than the global system whereas the opposite conclusion is reached for late-relaxing particles. In particular, as conjectured in ref. [56], the restricted ISFs curves show that τ_{early} and τ_{late} (denoted as the two peaks in the standard deviation in Fig. 4.2) are just the relaxation times of the early-relaxing and late-relaxing populations. Note that for very long times, $t \gg \tau_{late}$, the restricted MSDs merge signaling the dynamical homogenization of the system. In agreement with Eq.4.3, the time dependences of the ISFs and MSDs restricted to the early- and late-relaxing populations are found to be the same within the errors in the two states of the C set.

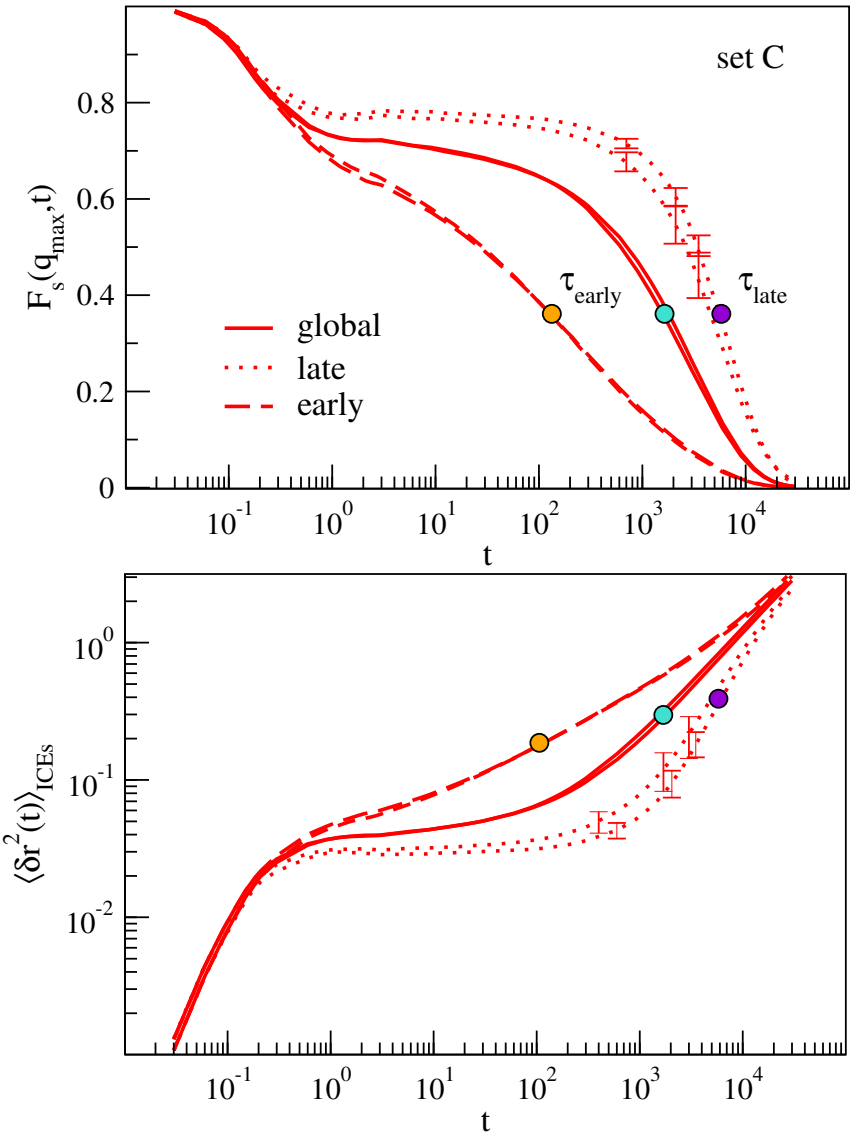

Figure 4.5: Characterization of the early-relaxing and late-relaxing monomers for the two states with slower relaxation (set C). Orange and violet dots mark τ_{early} and τ_{late}, respectively, as defined in Fig.4.2. Top panel: relaxation functions by either considering all the monomers or restricting to the early-relaxing and late-relaxing monomers. The latter two functions drop to $1/e$ at τ_{early} and τ_{late}, respectively. Bottom panel: mean square displacements of all the system and restricted to the early-relaxing and late-relaxing monomers. The former exhibits faster mobility than the latter at intermediate times recovering a homogeneous, identical behavior for $t \gg \tau_{late}$. Notice that the curves referring to the same quantity are independent of the state, in agreement with Eq.4.3.

4.2.4 Vibrational scaling of the early and late-relaxing fractions

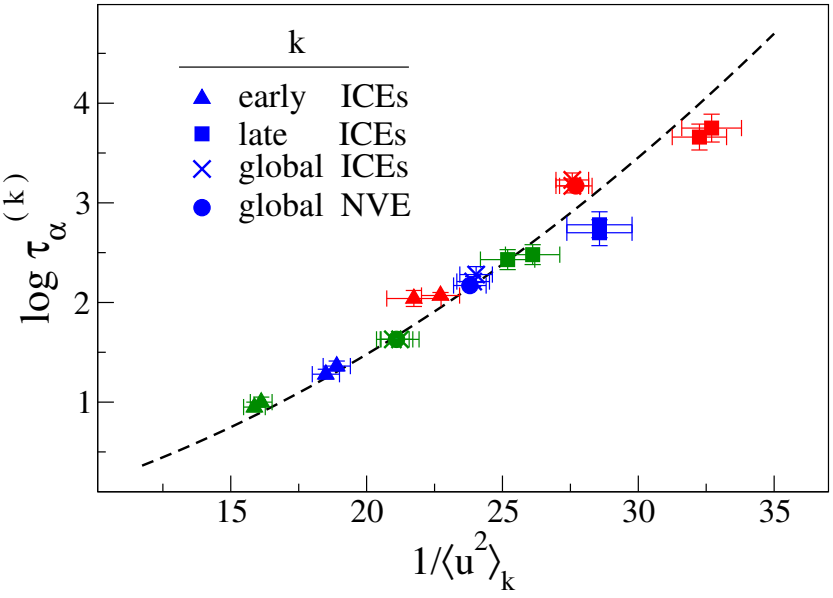

Figure 4.6: Vibrational scaling of the structural relaxation time $\tau_\alpha^{(k)}$ vs. DW factor $\langle u^2 \rangle_k$ for the states of the A, B and C sets. Color code as in Fig.4.2. The figure shows the scaling, originally found by considering the global relaxation, $\mathrm{k} = \{\mathrm{global}, \mathrm{NVE}\}$, [95] leading to the master curve Eq.4.5 (dashed line) [95]. Clearly such a scaling applies, with *no adjustable parameter*, to the early- and the late-relaxing fractions, $\mathrm{k} = \{\mathrm{early}, \mathrm{ICEs}\}$ and $\mathrm{k} = \{\mathrm{late}, \mathrm{ICEs}\}$, respectively. Error bars are affected by the limited size of the early- and late-relaxing fractions (about 6% and 2% of the total population of particles, respectively).

In order to test if the master curve Eq.4.2 holds for the early-relaxing and late-relaxing fractions, we recast Eq.4.2 as

$$\log \tau_\alpha = \alpha + \beta \frac{1}{\langle u^2 \rangle} + \gamma \frac{1}{\langle u^2 \rangle^2} \tag{4.5}$$

For the present model, irrespective of the non-bonding potential and the chain length, one finds $\alpha = -0.424(1), \beta = 2.7(1) \cdot 10^{-2}, \gamma = 3.41(3) \cdot 10^{-3}$ [95]. We remind that Eq.4.2 has been obtained originally by considering the global relaxation of a bulk system [95]. The results are shown in Fig.4.6. It is seen that the scaling also holds for the early-relaxing and late-relaxing fractions with *no adjustable parameter* over about three decades in relaxation time. It is worth noting that the extension of the master curve, Eq.4.5

with *no adjustable parameter*, to systems with remarkable mobility distribution has been also demonstrated in supported molecular thin film exhibiting strong mobility and relaxation gradients across the layers with monomer-size thickness [24].

4.2.5 Structure influence on the early-relaxing and late-relaxing fractions

As mentioned before, ICE is a tool to investigate eventual connection between the structure at a given instant and the subsequent dynamics. Therefore, it is quite natural to investigate if, and in what measure, the structure of the initial configuration has an influence on the early-relaxing and late-relaxing fractions. We first resort to a suitable definition of their local density and, later, to a detailed description of their spatial arrangement.

Fig.4.7 presents the time evolution of the Pearson correlation between the number of MI-correlated particles with the generic i-th central one at time t and the local density of its surroundings at the initial time, ρ_i^{local}. The latter quantity is evaluated in a sphere of radius $r_0 = 1.45$, centered on the i-th particle. The quantity r_0 is about the position of the first minimum of the radial distribution function (virtually independent of the state). Therefore, the evaluation in the sphere of radius r_0 is performed in order to restrict the computation to the first shell around the tagged particle. We see that states belonging to the same set (A,B,C) exhibit the same time dependence of the correlation. The time dependence is similar to the one observed in atomic liquids [56]. For $t < \tau_\alpha$ a negative correlation is observed which indicates a slight tendency for the early-relaxing particles to be located in regions with *lower* local density. We notice that the negative correlations start to decrease in modulus at $t \simeq \tau_{early}$ and vanish very close to τ_α. For $t > \tau_\alpha$ the correlation is positive suggesting that late-relaxing particles tend to be located in regions with higher local density with respect to the bulk (however note that the correlations are evaluated considering all the particles). The positive correlations start to decrease at $t \simeq \tau_{late}$. Fig.4.7 supports the conclusion that τ_{early} and τ_{late}, the times where the standard deviation of the number of correlated particles is maximum (Fig. 4.2), are to be interpreted as the lifetimes of the early- and late-relaxing fractions, respectively, as also suggested by Fig.4.5. On *increasing* the relaxation time τ_α by moving from the A set of states to the C set, Fig.4.7 clarifies that: i) the width of the region with negative correlation widens (in units of τ_α) whereas the region with positive correlations does not, ii) the magnitude of both the positive and the negative correlations do *not* change appreciably. The region with a

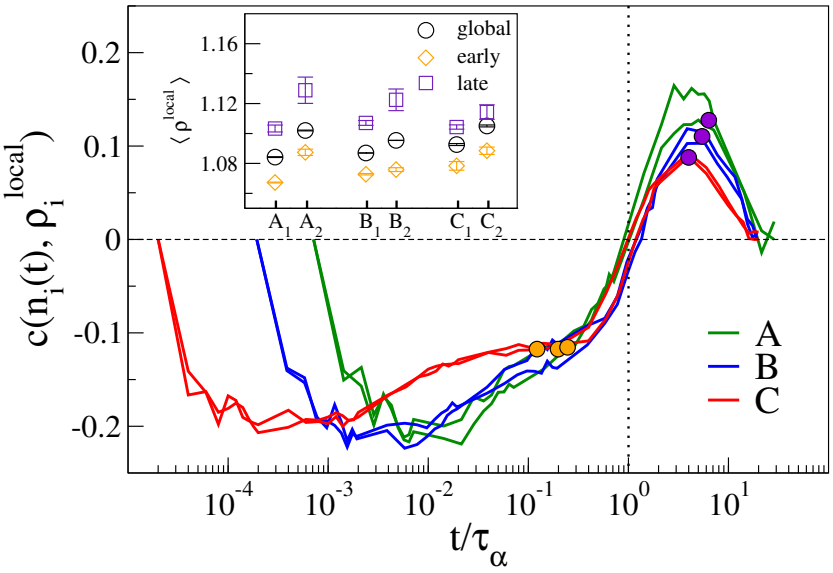

Figure 4.7: Pearson correlation between the local density around the generic i-th particle in the *initial* configuration of the ICEs and $n_i(t)$, the number of MI-correlated particles at time t. Orange and violet dots mark τ_{early} and τ_{late}, respectively, as defined in Fig.4.2. For $t < \tau_\alpha$ particles with higher MI-correlation belong to sites with initial lower density. For $t > \tau_\alpha$ particles with higher MI-correlation belong to sites with initial higher density. Inset: comparison between the density and the average local density at the sites where the early and late-relaxing particles are located for all the six investigated states. Late-relaxing monomers are located in denser sites than early-relaxing ones.

negative Pearson correlation between particles with high MI-correlations and local density is expected to be contributed by early-relaxing particles whereas late-relaxing particles should come up with positive Pearson correlations. In fact, the inset of Fig.4.7 shows that the average local density of the early-relaxing particles is lower than the global one and the opposite holds true for the late-relaxing ones.

On increasing the relaxation time moving from the A set of states to the C set, the deviations of the local densities from the global one tend to decrease. This suggests that packing effects alone are unable to provide insight into more subtle details as the relative shift of τ_{early} and τ_{late} with respect to τ_α noted in Fig.4.2. In that respect, we now investigate the role of the kind of spatial arrangements of the correlated particles.

As a further measure of local structure, we employ the *topological cluster classification* (TCC) of a tagged particle surrounding [101], which has already been adopted to investigate the structure of a large variety of system, ranging

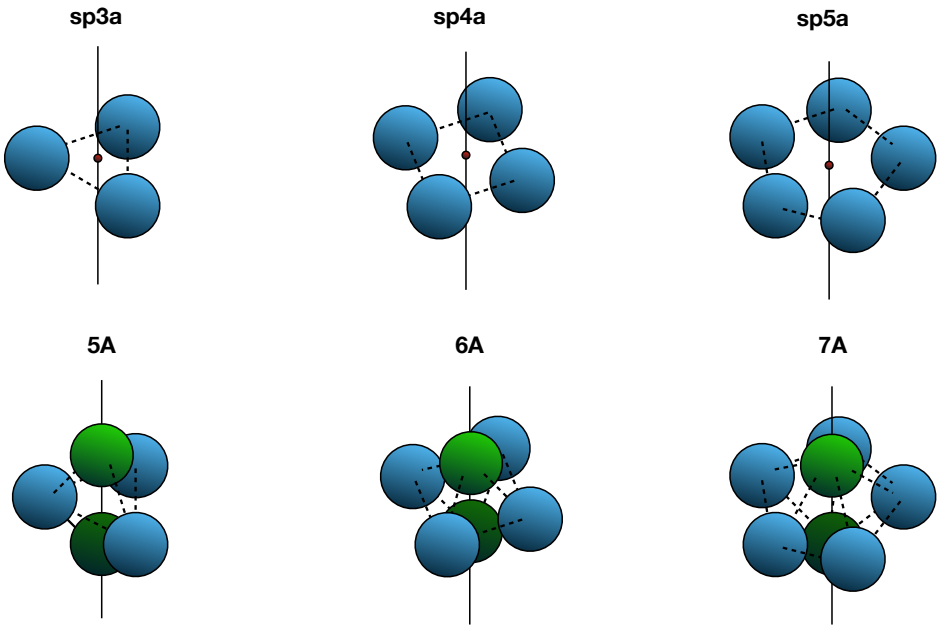

Figure 4.8: A few example of the topological cluster detected with TCC [101]. On top, the most relevant shortest path ring clusters; on the bottom some of the most significant globular clusters.

from simple liquid to colloid-polymer mixtures [136, 137, 154]. TCC relies on a modified Voronoi decomposition to identify the neighborhood topology and compare the latter with the one of isolated equilibrated clusters. In particular, we analyze the structure of the initial spatial configuration and identify the topological clusters owning each particle. It is important to remind that a particle can be owned by more than one cluster, even of the *same* kind.

Fig.4.9 shows the Pearson correlation between the generic i-th particle with $n_i(t)$ MI-correlated surrounding particles at time t and $M_{i,\kappa}$, the number of different kinds of clusters, labeled by the κ identifier, owning the i-th particle in the initial configuration, for a state of the C set. The complete list of identifiers and the corresponding description of the clusters is given in Ref. [54, 101]. The high numbers of curves signals that the kinds of cluster with some Pearson correlation is not low.

In order to devise a viable procedure to compare the six states forming the A, B and C sets, we highlighted the kind of clusters which maximize the modulus of the Pearson correlation at both τ_{early} and τ_{late} in all the six states. These clusters are believed to be better correlated to the dynamics in a state-independent way. Fig.4.9 shows that for $t < \tau_\alpha$ particles, with higher number of MI-correlated partners than the average, belong to quasi-planar clusters of

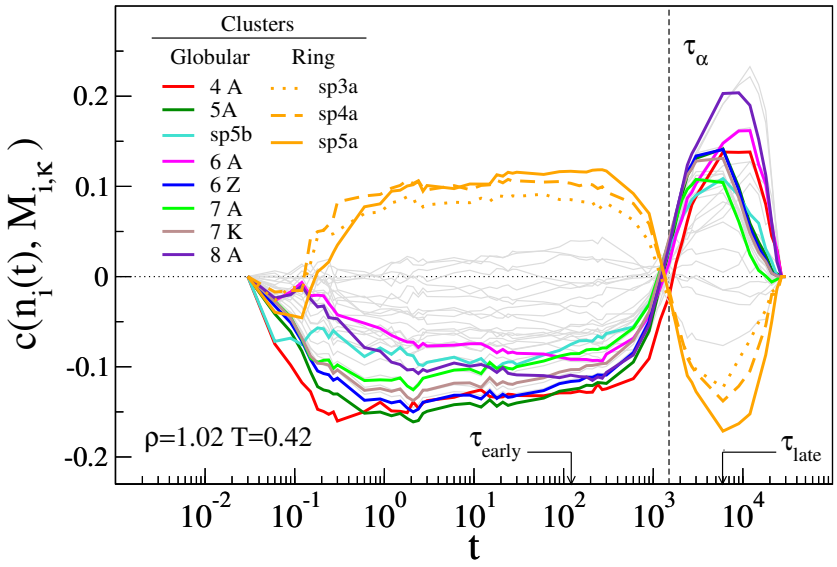

Figure 4.9: Pearson correlation between $n_i(t)$, the number of MI-correlated particles with the generic i-th particle at time t, and the number of clusters with κ identifier owning the i-th particle in the initial configuration, $M_{i,\kappa}$. The analysis is performed for a state of the C set. The highlighted curves correspond to the set of clusters which maximize the modulus of the Pearson correlation at both τ_{early} and τ_{late} in *all* the six states of the sets A, B, C. Their κ identifiers, according to the taxonomy of refs. [54, 101], are listed in the legend. The procedure reveals correlation with ring structures at short times whereas at long times, among others, globular structures like the tetrahedron (4 A), the triangular bi-pyramid (5 A), the octahedron (6 A) and the pentagonal bi-pyramid (7 A) are signaled. The grey curves signal the presence of several other kinds of clusters with some Pearson correlation.

3, 4 and 5 particles known as *shortest path ring* which are associated to lower local density [56]. This agrees with Fig.4.7. Differently, for $t > \tau_\alpha$ highly correlated particles belong to globular clusters like the tetrahedron (4 A), the triangular bi-pyramid (5 A), the octahedron (6 A), the pentagonal bi-pyramid (7 A) and other complex structures with a higher number of particles [101]. Some of the aforementioned structures are graphically represented in Fig. 4.8.

It must be pointed out that some of our selected clusters are also revealed in atomic liquids [56]: for example, the ring clusters sp3, sp4 and sp5, are detected in the early-relaxing population. Instead, globular clusters like 10B and 12D, detected in the late-relaxing population of atomic liquids do not pass our selection criteria owing to a low Pearson correlation. Moreover, long long-lived clusters in hard-sphere systems like icosahedron (13A) [135]

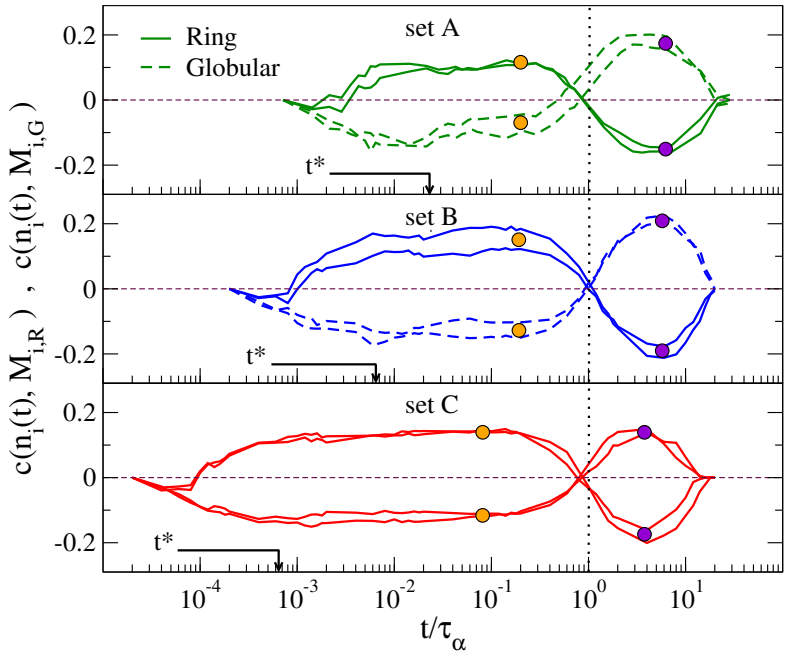

Figure 4.10: Pearson correlation between $n_i(t)$, the number of MI-correlated particles with the generic i-th particle at time t, and the number of either ring (planar) or globular clusters identified in Fig.4.9 owning the i-th particle in the initial configuration, $M_{i,R}$ and $M_{i,G}$, respectively. Orange and violet dots mark τ_{early} and τ_{late} (violet dot), respectively.

are barely detected in our molecular system.

Even if the above selection procedure captures significant structural features of the clusters owning the particles with high MI correlation, it still exhibits some small state-dependence, since the magnitude of the Pearson correlation of the selected clusters still depends on the state. In order to reduce this effect, we consider the Pearson correlation between $n_i(t)$, and the number of either ring (planar), $M_{i,R}$, or globular clusters, $M_{i,G}$, identified in Fig.4.9 owning the i-th particle in the initial configuration. The results are shown in Fig.4.10. Interestingly, this less detailed characterization offers additional insight. As to the relative shift of τ_{early} and τ_{late} with respect to τ_α noted in Fig.4.2, one sees that τ_{early} and τ_{late} provide not only a measure of the relaxation time of the early-relaxing and the late-relaxing fractions, but they also offer a measure of the lifetime of selected subgroups, i.e the ring and the globular clusters respectively. Furthermore, Fig.4.10 recovers the property defined by Eq.4.3, i.e. states with the same DW factor exhibit rather close behavior of specific time-dependent observables at all times, from vibrational time scales to long times. In particular, we observe

it holds considering the Pearson correlation, presented in Fig.4.10, (less apparent in the B set) between particles with high number of MI-correlated particles and the number of their inclusions in specific sets of either planar or globular clusters. This finding suggests that Eq.4.3 is, at least in part, enforced by structure. A similar indication was reached by considering the scaling between elasticity and relaxation [126]. The validity of Eq.4.3, recovered in Fig.4.10 stands in harmony with all the other quantities presented in this study, i.e. global ISF and MSD (Fig.3.3 and Fig.4.1), average and standard deviation of the global distribution of MI-correlated monomers (Fig.4.2), Pearson correlation coefficients of the number of MI-correlated particles with propensity (Fig.4.3) and local density (fig.4.7). The above finding further substantiate our previous conclusion that physical states with identical vibrational properties, as quantified by the Debye-Waller factor, manifest strong dynamic similarity at long times, i.e at least the structural relaxation time [24, 73, 80, 95, 113, 123, 131, 144].

4.2.6 Clustering of early and late-relaxing fractions

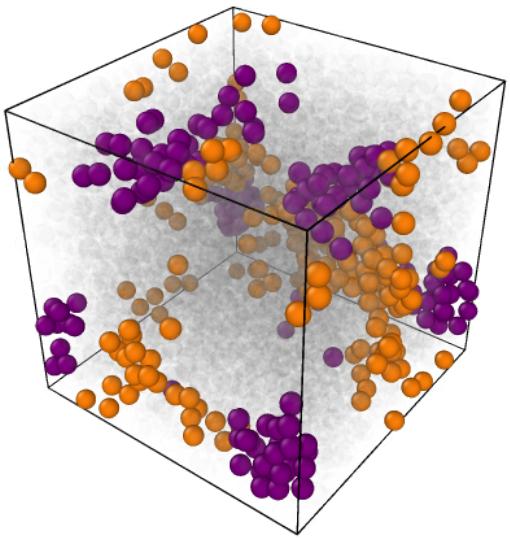

Figure 4.11: A typical distribution of the two fractions of particle, *early* (orange particles) and *late* (violet particles) in an ICE starting configuration of the slowest thermodynamic state considered ($\rho = 1.02$ ant $T = 0.42$). Their spatial distribution points out their tendency to be organized in local clusters.

We now focus on the spatial distribution of the particles composing the

two populations *early* and *late*, in each ICEs starting configuration. Recently the spatial analysis of the correlated motion has been related to the presence of *string-like motion* [50, 51, 149]. The latter implies the presence of mobile regions of the sample with a fractal dimension $d < 3$, and growing in size on approaching the glass transition, understood within the Adam-Gibbs theory[2]. We want to test if the two isolated populations exhibit some spatial arrangement that can be understood within this context. Let us consider, for instance, the initial configuration of a single ICE of one of the thermodynamic states, belonging to the C set, reported in Fig.4.11. The *early* population is colored in orange while the *late* one in purple. For both populations, we observe a tendency to form localized clusters. To formally characterize this behavior it is necessary to give an operative definition of "localized clusters" and then catalog each particle belonging to the given population according to this definition. To do so, we employed a classical "bottom-up" clustering algorithm based on the spatial distance between monomers. For each population, *early* or *late*, the algorithm can be described by the following steps:

1. initialize an empty cluster;
2. choose a particle belonging to the selected population and include it in the cluster;
3. look for particles of the same population within a distance d and include them in the cluster as well;
4. repeat step 2 for all the new particles in the cluster; if there are no new members the cluster is complete;
5. restart from step 1 and excluding from the algorithm the already cataloged particles.

Therefore, a cluster is defined as a set of particles of the same population whose distance from at least one other member of the cluster is less than d. We chose the distance d as the first minimum of the radial distribution function. For the present study $1.44 \leq d \leq 1.46$. Changing reasonably the value of d does not affect the resulting division in clusters.

In Fig.4.12 is reported the effect of slowing down the dynamics of the system on $\langle M \rangle$, the detected clusters average size. The average $\langle ... \rangle$ is taken considering all the detected clusters in a given ICE and then considering all the investigated ICEs for the given thermodynamic state. On the abscissa, the structural relaxation time, τ_α. It is seen that changing the relaxation time by a factor ≈ 40 strongly affect the cluster size for both the populations.

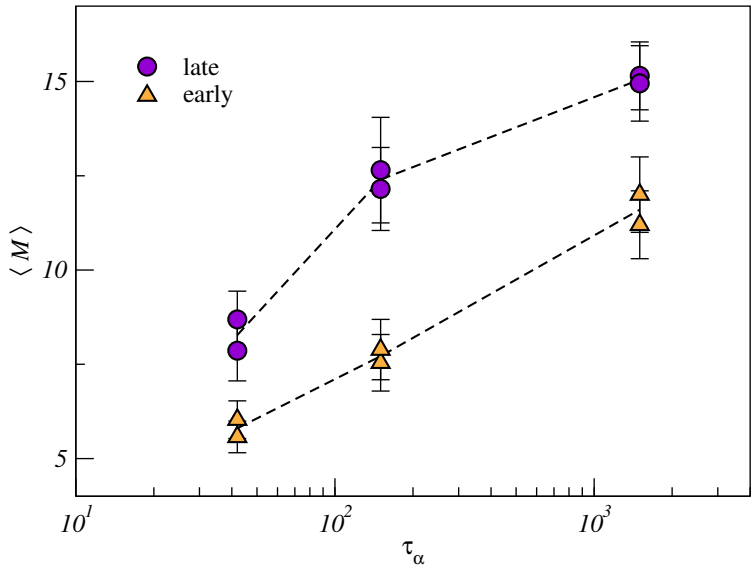

Figure 4.12: Average clusters size as a function of the structural relaxation times for the three investigated states. Both the *early* population (higher propensity and faster relaxation) and the *late* one (lower propensity and slower relaxation) form localized clusters of increasing size with the relaxation time τ_α.

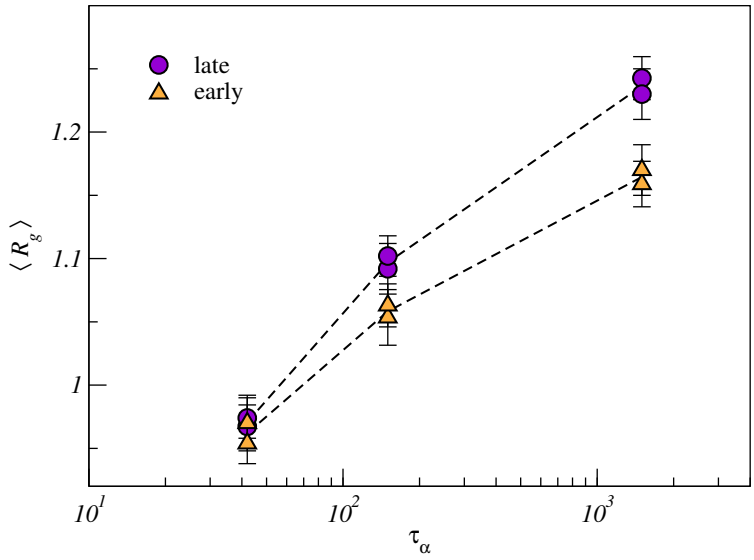

Figure 4.13: Average clusters gyration radius $\langle R_g \rangle$ versus the structural relaxation time for the three investigated states. Both populations show an increasing $\langle R_g \rangle$ with τ_α, but the *early* fraction exhibits a slower growth with respect to its *late* counterpart.

To further characterize the clusters of *early* and *late* particles, we computed their gyration radius R_g. The latter is defined for a cluster cl of size M as

$$R_g^{cl} = \left[\frac{1}{M} \sum_{i \in cl} (\mathbf{r}_i - \mathbf{r}_{cm})^2 \right]^{\frac{1}{2}} \tag{4.6}$$

where $\mathbf{r}_{cm}$ is the cluster center of mass. Fig.4.13 shows the average gyration radius $\langle R_g \rangle$ as a function of the structural relaxation time τ_α. Again, we observe a growth for the clusters gyration radii of the two populations. It is interesting to note that *early* clusters exhibit a slightly slower growth of R_g with respect to their *late* counterparts in the explored window of relaxation times. In fact, the average gyration radius of *early* clusters grows of about 21% to be compared with the one of *late* clusters that grows of about 29%.

The growth of the two populations average cluster sizes with the relaxation time, as well as the one of the clusters gyration radii, is a clear manifestation of the increasing dynamical heterogeneity. In addition to this, states with equal structural relaxation time shows equal markers of the dynamical heterogeneity. This fact is in perfect harmony with the noted scaling relation between the fast vibrational dynamics and the slow heterogeneous one [131].

Putting in direct relation the growth of the size of the cluster with the respective growth of its gyration radius, it is possible to have an insight on the typical spatial arrangement of clusters belonging to different families, *early* or *late*. In Fig.4.14 the scatter plot of the size versus the respective gyration radius, for all the detected clusters in all the states considered in this work, is reported . Fitting the distribution with the relation

$$M = cR_g^d \tag{4.7}$$

where c is a scaling factor, it is possible to obtain d, the fractal dimension of the cluster. In Fig.4.14 the example of an ideal spherical cluster, having $d = 3$, is also plotted for comparison. It can be seen that clusters composed by *early* particles tend to be *less-than-bidimensional* with a dimensionality that is slightly less than 2 ($d = 1.87(2)$). Conversely, *late* particles are arranged in clusters with a dimensionality very close to the one of a sphere: $d = 2.45$ when the fit is done considering al the detected cluster, higher if the fit is carried out excluding very small clusters ($d = 2.63(2)$ fitting in the range $M \geq 3$ and $d = 2.98(2)$ fitting in the range $M \geq 5$). This finding is consistent with the result of the analysis discussed in Sec. 4.2.5 and also the one carried out in Ref.[56] where the correlation with peculiar planar (for *early* particles) and globular (for *late* particles) topological structures[101] is observed.

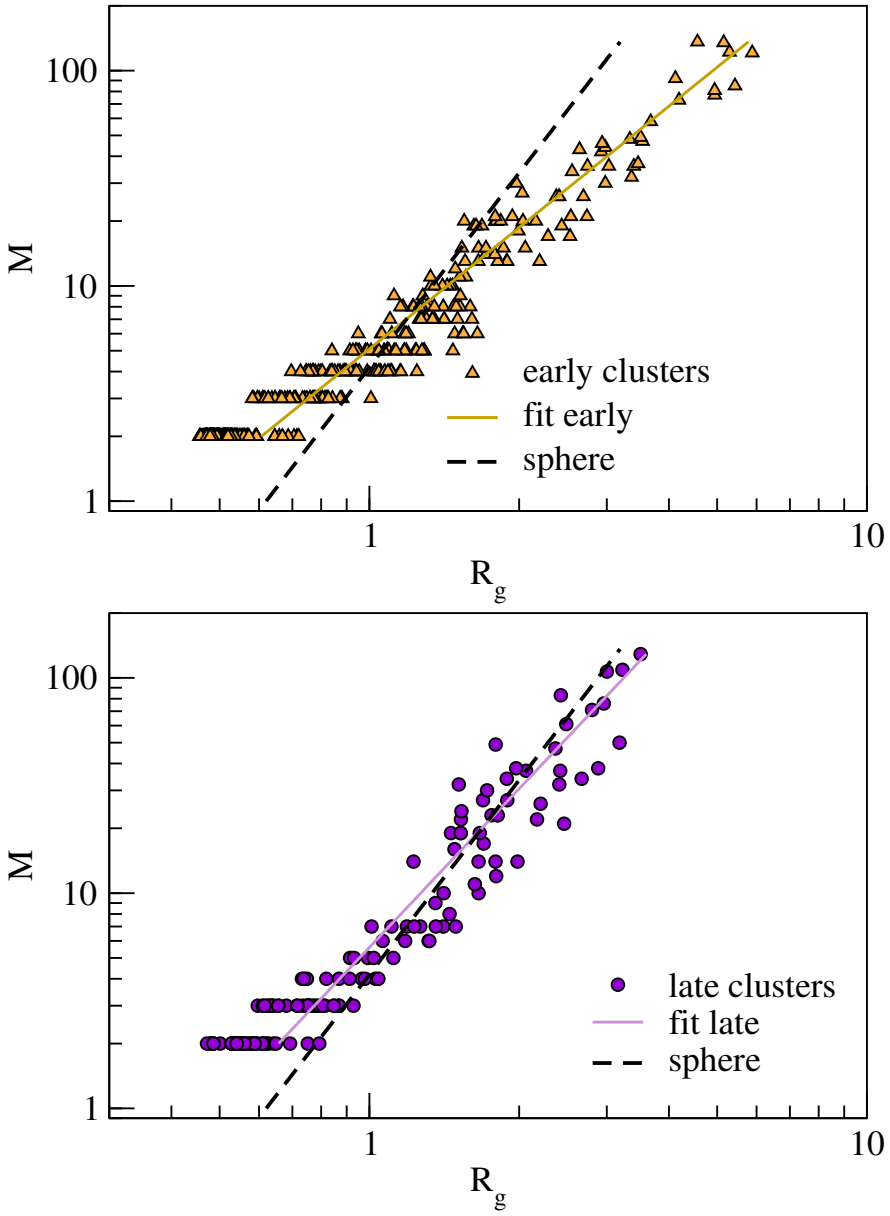

Figure 4.14: Scatter plot of the size M versus the respective gyration radius R_g for all the detected clusters in all the states considered in this work. *Early* clusters in the top panel and *late* ones in the bottom panel. Every point in both the panels corresponds to a single cluster detected in a starting configuration of a given ICE of a given thermodynamic state. The black dashed lines correspond to the growth of the size M of a spherical object with radius R_g. The best fit curves reported in both panel are obtained considering all the points in the graph.

The observation that the highly mobile, early population forms cluster of fractal dimension $d < 2$ makes it nearly impossible not to think of *stringlets*, the unidimensional elementary units of a larger cooperative rearranging region, whose average length grows exponentially approaching the glass transition. Even though we did not perform an analysis to directly detect string-like motion, our results are indeed compatible with its presence. Stringlets are usually observed among the mobile fraction of the system[149] (obtained by considering for example 5-7% of particles with the greater displacement). For this reason, the previous result is not particularly surprising as we have shown that our choice of isolating the particle population based on the number of correlated partners at peculiar times, selects as a consequence a mobile fraction of the whole sample. Yet, our procedure adds a novel point of view on potentially string-like moving particles characterizing them as particles belonging to, not only to the upper-bound of the mobility distribution but also belonging to the upper bound of the number of MI-correlated partners at early times distribution.

4.3 Conclusions

The heterogeneous dynamics in a mildly supercooled molecular liquid has been investigated by MD simulations. The analysis revealed MI correlation between particle displacements which allowed the identification of two particles fractions (*early* and *late*) with different mobility and relaxation. The two fractions exhibit vibrational scaling of their relaxation with master curve not differing from the one found for the bulk, thus confirming results found for other systems with strong dynamic heterogeneity, as thin molecular films. An analysis of the local structure in terms of local density is carried out to look for correlation with the two fractions. Such analysis evidenced a tendency for the early fraction to be located in less dense areas of the system while the late fraction in more dense ones. Yet, packing effects alone are unable to clarify entirely finer aspects of the dynamics of the two fractions. A more refined analysis suggests excitation of planar and globular structures at short and long times, respectively. The observation that states with equal DW factor have identical behavior of any other time-dependent quantity, at least up to τ_α, has been further confirmed also for other bulk quantities and extended to fraction-specific properties, in addition to the already known cases of MSD, ISF and NGP.

We also investigate the spatial organization of the *early* and *late* fractions. We find evidence of the tendency of the two fractions to form localized clusters, whose size increases with the structural relaxation time. The aver-

age gyration radius of these clusters, which offers a natural length scale for the dynamical heterogeneity, is compatible with the progressive solidification on approaching GT. This length scale provides a solution to the issue of observing a MI-correlation length poorly growing on approaching the glass transition[160] reported in Chapter 3. Moreover, the cluster analysis carried out directly on the *early* and *late* population offers a neat view on the cluster dimensionality, evidencing the tendency for fast *early* particles to be arranged in less-then-bidimensional cluster while the slow *late* ones tend to form globular (tridimensional) clusters.

The findings of the investigation reported in this chapter in the sections 4.2.2, 4.2.4 and 4.2.5 have been published in the European Physical Journal E [162].

Chapter 5

Scaling in presence of an emergent β-relaxation process

5.1 Research context

On approaching the glass transition, molecular rearrangements occur via both the primary mode, referred to as structural or α relaxation, and the faster secondary (β) processes as evidenced by mechanical, electrical, and thermal properties of materials [13, 103, 110]. Although it has been the topic of a large number of phenomenological and theoretical studies, as well as of experiments and simulations [37, 75, 85, 99, 107, 110, 111], there is still no definitive microscopic description available for the β relaxation. There is a special class of secondary relaxations involving translation or reorientation of the molecular unit as a whole, well different from the trivial ones, related to intramolecular degrees of freedom, such as the motion of pendant groups in polymers. This special class of β processes, called Johari Goldstein (JG), to honor the researchers that first noticed it [85], is universal in glass formers [107, 110, 111] and has been shown [107] to have strong relation to structural α-relaxation, being both governed by intermolecular interactions. A number of experimental results indicate that this JG β relaxation is sensitive to the thermodynamic variables underlying the glass transition [110, 111]. In this aspect, it mimics the α relaxation, being strongly pressure dependent. It also shows the invariance of the ratio τ_α/τ_β to variations of pressure and temperature, keeping τ_α constant. For these reasons, JG β-relaxation can be considered as the precursor of the structural relaxation, which has a slower dynamics due to cooperativity involving many body dynamics [37, 107].

In this Chapter we investigate whether the presence of well resolved secondary relaxation could disprove the universal correlation between the vi-

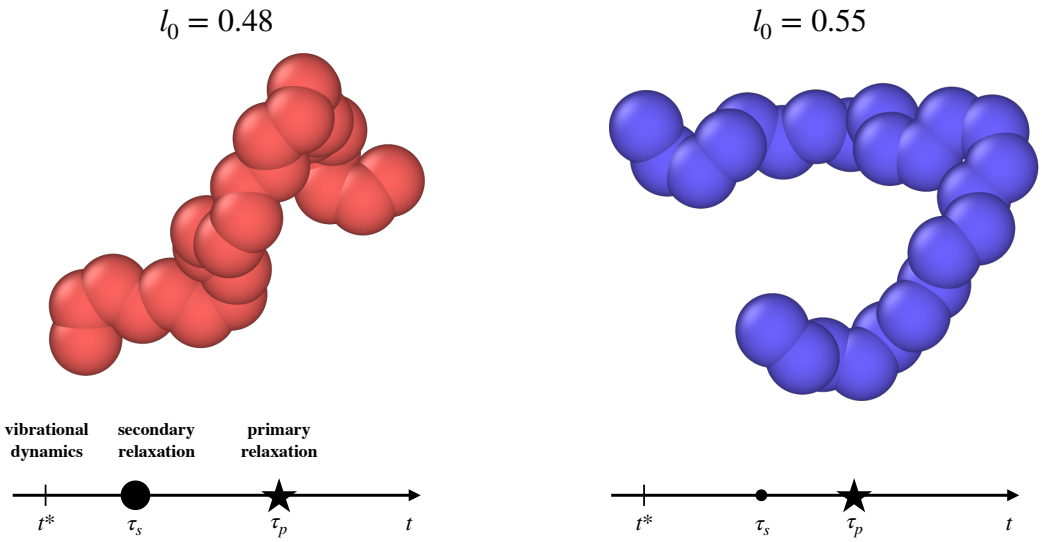

Figure 5.1: Pictorial view of the two kind of polymeric chains under consideration. l_0 denotes the bond length. The time axis signal, in a qualitative way, the location of the dynamical processes of interest. The size of the dot of the secondary relaxation is proportional to the strength of the relaxation. The exact definition of the symbols is given in Sec.5.3.

brational dynamics and the primary relaxation observed by experiments and numerical simulations in highly viscous liquids [95, 131]. This research is motivated by the fact that the timescale of the secondary relaxation ($\overline{\tau}_s$) is *intermediate* between the vibrational timescale (t^*), a few picoseconds, and the structural relaxation time of the primary relaxation ($\overline{\tau}_p$) which reaches about hundreds of seconds close to the glass transition:

$$t^* \ll \overline{\tau}_s < \overline{\tau}_p. \tag{5.1}$$

The exact definitions of the symbols in Eq.5.1 will be given in Sec.5.3. Here, we are interested in the secondary relaxation observed in the *main chain* of *linear* polymers without side groups. This class fits the definition of JG relaxation [111]. There is consensus that in linear chains the JG process involves local motion of the polymer backbone.

Recently, the investigation of JG relaxation by using MD simulations has been facilitated by the development of coarse-grained models of linear polymers having fixed bond length and bond angles constrained to 120° [26, 27, 64]. It is also worth mentioning studies of the JG relaxation in asymmetric diatomic molecules [62, 64].

5.2 Model and Numerical Methods

We investigate two coarse-grained models of linear polymer chains. Such coarse-grained models take a cue from models perfected in a series of work[26, 27] by Bedrov and Smith to effectively simulate 1,4 Polybutadiene melts. The polymer melts are constituted by $N_c = 512$ linear chains made of $M = 25$ monomers each, resulting in a total number of monomers $N = 12800$. Non-bonded monomers at a distance r interact via a Lennard-Jones potential:

$$U^{LJ}(r) = \epsilon \left[\left(\frac{\sigma^*}{r} \right)^{12} - 2 \left(\frac{\sigma^*}{r} \right)^{6} \right], \tag{5.2}$$

where $\sigma^* = 2^{1/6}\sigma$ is the minimum of the potential, $U^{LJ}(r = \sigma^*) = -\epsilon$. The potential is truncated at $r = r_c = 2.5\sigma$ for computational convenience. Adjacent bonded monomers interact with each other via the harmonic potential

$$U^{bond}(r) = k_{bond} \left(r - l_0 \right)^2 \tag{5.3}$$

where the constant k_{bond} is set to $2000\epsilon/\sigma^2$ to ensure high stiffness. We consider two distinct cases, corresponding to rest bond length l_0 set to either $l_0 = 0.48\sigma$ or $l_0 = 0.55\sigma$. The rationale behind our choice of the two bond lengths relies on the finding that previous Molecular-Dynamics (MD) simulations of the present model [27], investigating the rotational dynamics, revealed the steep *increase* of the separation between the primary and the JG relaxations by *decreasing* the bond length below $l_0^\star = 0.5\sigma$ (corresponding to 2Å in Fig. 3 of Reference [27]). Therefore, one anticipates that the JG relaxation is much more apparent if $l_0 = 0.48\sigma$ with respect to $l_0 = 0.55\sigma$. A bending potential

$$U^{bend}(\alpha) = k_{bend} \left(\cos\alpha - \cos\alpha_0 \right)^2 \tag{5.4}$$

with $k_{bend} = 2000\epsilon/\sigma^2$ and $\alpha_0 = 120°$, is introduced to maintain the angle α formed by two consecutive bonds nearly constant (see Fig.5.1 for typical chain conformations) [94].

All the data presented here are expressed in reduced MD units: length in units of σ, temperature in units of ϵ/k_B, where k_B is the Boltzmann constant, and time in units of $\tau_{MD} = (m\sigma^2/\epsilon)^{1/2}$. We set $\sigma = 1$, $\epsilon = 1$, $m = 1$ and $k_B = 1$.

Simulations were carried out with the open-source software LAMMPS [1, 122]. Equilibration runs were performed at constant number of monomers N, constant vanishing pressure $P = 0$ and constant temperature T (NPT ensemble). Temperature and pressure have been controlled via a Nosé-Hoover

thermostat and barostat. The glass transition temperature of this model is significantly higher with respect to the previous model's one. This is largely due to the chain bending stiffness adding constraints to the dynamics and therefore making rougher the potential energy landscape[139, 158]. An approximate estimate of the glass transition temperature of this model can be achieved considering a fairly similar model[106] for which one obtains $T_g \approx 0.8$. For each state the equilibration lasted at least for $3\tau_{ee}$, being τ_{ee} the relaxation time of the end-to-end vector autocorrelation function [7–9, 21, 49, 96]. Production runs have been performed within the NVT ensemble (constant number of monomers N, constant volume V and constant temperature T) instead of the usual NVE ensemble (constant energy E). This choice has been dictated by the exigence of a sharp control on the temperature to achieve a meaningful comparison between the two investigated systems. Additional short equilibration runs were performed when switching from NPT to NVT ensemble. No signatures of crystallization were observed in all the investigated states.

As a final remark, we point out that our adoption of a monodisperse polymer model where all the chains have equal length is not expected to limit our conclusions. In fact, the vibrational scaling collapses in a single master curve both the MD results of monodisperse polymer models and the experimental data on polymers which, expectedly, refer to polydisperse systems [95].

5.3 Results and discussion

5.3.1 Bond reorientation

Since in linear chains the JG process involves local motion of the polymer chain backbone [110, 111], we focus on the most elementary relaxation process, that is, the reorientation of the bond linking two adjacent monomers of the same chain. To this aim, we consider the unit vector along the m-th bond of the n-th chain at time t

$$\mathbf{b}_{m,n}(t) = \frac{1}{l_0}(\mathbf{r}_{m,n}(t) - \mathbf{r}_{m+1,n}(t)), \tag{5.5}$$

where $\mathbf{r}_{m,n}(t)$ denotes the position of the m-th monomer in the n-th chain at time t. Hence, we define the bond correlation function (BCF) $C(t)$ [20]

$$C(t) = \frac{1}{N_c}\frac{1}{M-1}\sum_{n=1}^{N_c}\sum_{m=1}^{M-1}\langle \mathbf{b}_{m,n}(t)\cdot\mathbf{b}_{m,n}(0)\rangle. \tag{5.6}$$

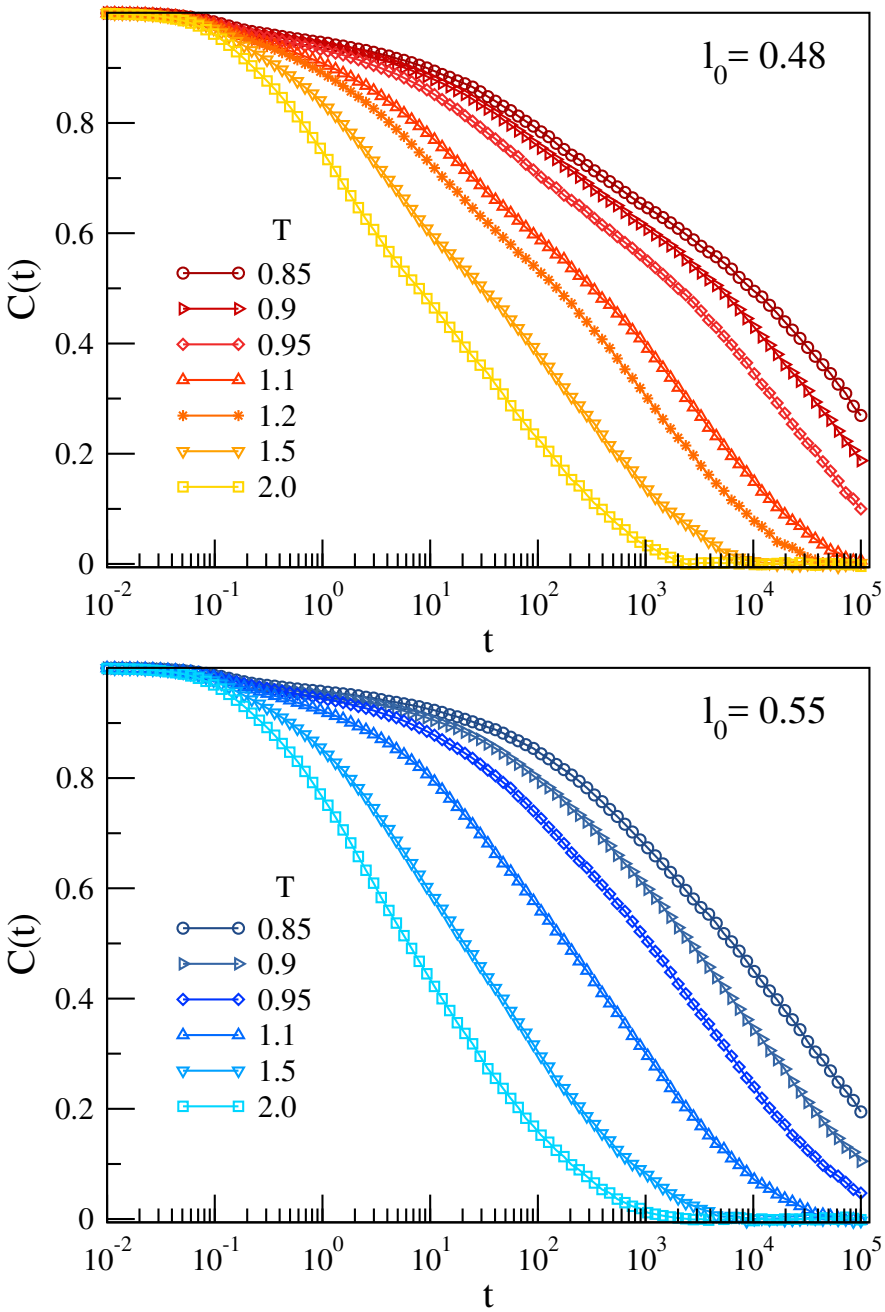

Figure 5.2: Temperature dependence of the BCF of the chains with different bond length. If $l_0 = 0.48$, a two-step decay –evidencing two distinct relaxations– is observed.

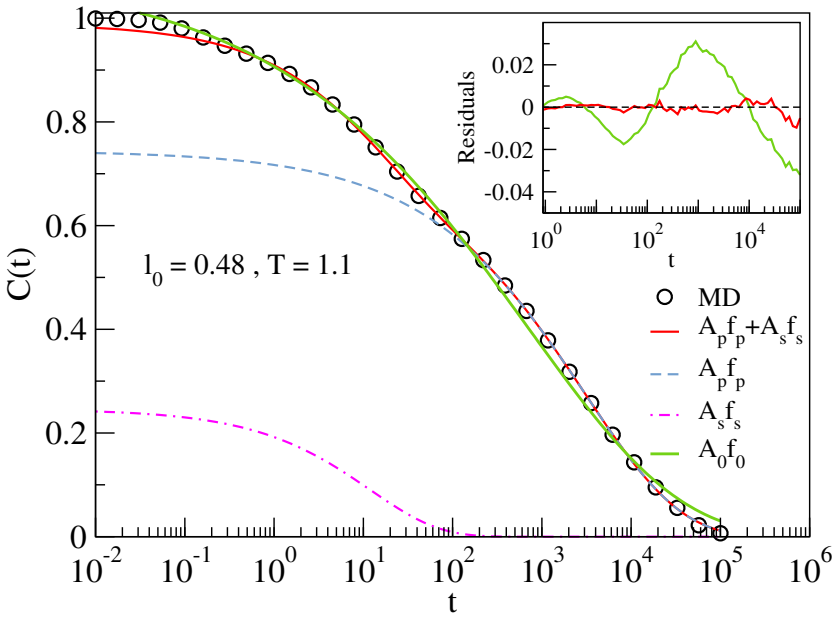

Figure 5.3: Illustrative example of the best-fit results via the double-relaxation function Eq.5.7. The best-fit with the single-relaxation function $A_0 f_0$ with f_0 in the form of Eq.5.8 is also shown. Inset: residuals of the best-fit with the double- and single- relaxation functions.

The brackets $\langle \cdots \rangle$ denote a suitable ensemble average. $C(t)$ decreases in time (by definition $C(0) = 1$), finally vanishing at long times when the bond orientation has explored all the unit sphere.

Fig.5.2 plots the correlation function $C(t)$ for the two polymer melts with chains having different bond length. In agreement with previous studies [26, 27], we found that the chains having shorter bond length exhibits a characteristic two-step decay, which is a signal of the presence of two distinct relaxation processes.

To gain more insight, we analyzed the correlation function $C(t)$ under the assumption that it is well represented by the weighted sum of two components, that is, a fast secondary process and a slower primary one

$$C(t) = A_p f_p(t) + A_s f_s(t) \tag{5.7}$$

where $f_p(t)$ and $f_s(t)$ are two decaying functions with amplitudes A_p and A_s, respectively. The explicit form of $f_i(t)$ is taken as a stretched exponential

$$f_i(t) = \exp\left[-\left(\frac{t}{\tau_i}\right)^{\beta_i}\right], \qquad i = p, s \tag{5.8}$$

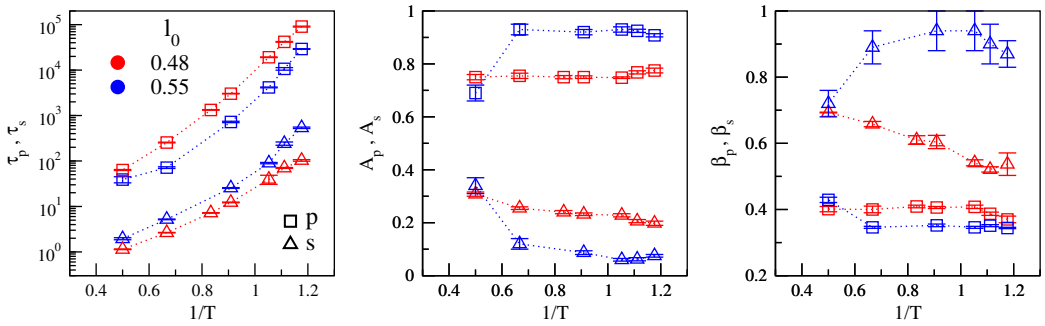

Figure 5.4: Plots of the temperature dependence of the best-fit parameters by using Eq.5.7 and Eq.5.8 (color codes as in Fig.5.1). From left to right: apparent relaxation times, relaxation strengths and stretching exponents.

where τ_i denotes the relaxation time and β_i the stretching exponent (as normally $\beta_i \leq 1$). We fit the MD data concerning the correlation function $C(t)$ with Eq.5.7 excluding the time window $t \leq \hat{t}$ where the decay of the function is controlled by the ballistic motion of monomers ($0.6 \leq \hat{t} \leq 1$ with $\hat{t}$ decreasing slightly by increasing T).

The analysis in terms of a sum of two stretched exponential decays, Eq.5.7 and Eq.5.8, conforms with most studies of primary and secondary relaxations in MD simulation [26, 27, 64, 65, 145] and in some experiments performed in time domain [74, 173]. Hence, it facilitates the comparison between our results and the ones present in literature.

We have also considered the use of alternative functions to fit the secondary relaxation. For instance, we tested the Mittag Leffer function (with 2 fitting parameters like the stretched exponential), corresponding to the time-domain counterpart of the Cole-Cole function and usually used in studies of dielectric spectroscopy to describe the secondary process [78, 120]. Yet, we found no significant differences in terms of relaxation times and strengths with respect to the analysis with the sum of stretched exponentials.

Fig.5.3 shows an example of the result of the best-fit of $C(t)$ considering Eq.5.7 and Eq.5.8 for a representative state of the model. For comparison, the best-fit with a single stretched exponential decay is also shown. The residuals $C^{MD}(t) - C^{\text{fit}}(t)$ plotted in the inset of Fig.5.3 prove the poor performance of the single-relaxation curve to fit the MD data.

Fig.5.4 presents the temperature dependence of the parameters extracted from the best-fit of data with Eq.5.7 and Eq.5.8. It is seen that the reduction of the bond length has two major effects: i) an *increased* separation of the relaxation times τ_s and τ_p ii) an *enhanced* amplitude of the secondary relaxation with respect to the primary one. It is also worth noting that the

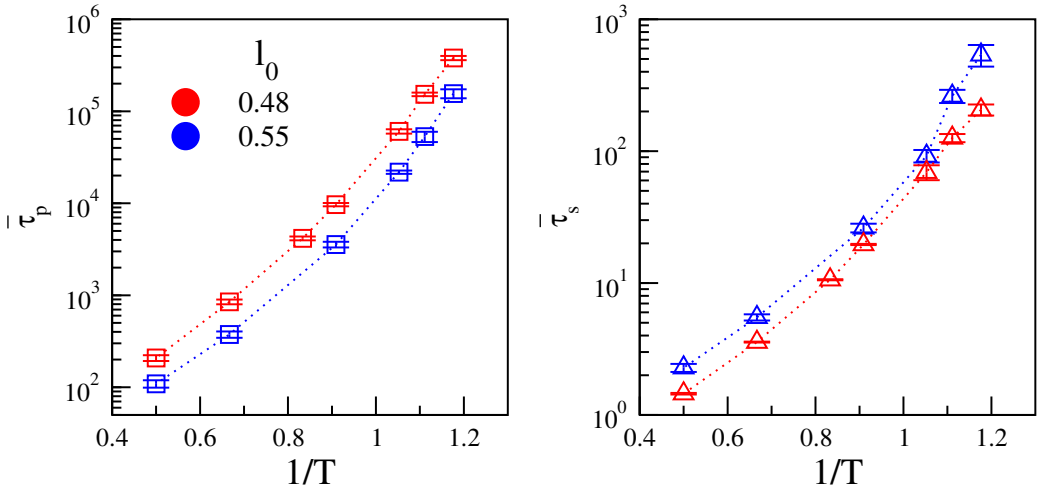

Figure 5.5: Arrhenius plots of the average relaxation times of the primary ($\overline{\tau}_p$, left) and secondary ($\overline{\tau}_s$, right) relaxations. Color code as in Fig.5.1.

primary relaxation is less stretched in the model where the secondary relaxation is more apparent ($l_0 = 0.48$) compared to the case in which it is weak ($l_0 = 0.55$). The differences are small but significant, that is, larger than the errors on the stretching exponents. Stretched relaxation is usually associated with the presence of dynamical heterogeneities, namely the spatial distribution of mobilities, which may differ by orders of magnitude in regions only a few nanometers away. In this framework, our results suggest that the presence of a not negligible secondary relaxation process slightly decreases the degree of dynamical heterogeneity of the system. This aspect will be addressed in Chapter 6.

To get rid of the temperature dependence of the stretching exponent β, we define the average relaxation time for the primary and the secondary relaxations, $\overline{\tau}_p$ and $\overline{\tau}_s$ respectively, as the time-integral of the corresponding relaxation function (f_p and f_s) leading to

$$\overline{\tau}_i = \frac{\tau_i}{\beta_i}\,\Gamma\left(\frac{1}{\beta_i}\right), \qquad i = p, s \tag{5.9}$$

The temperature dependence of the average relaxation times of the two polymer models are shown in Fig.5.5. For both systems the primary relaxation time (left panel in Fig.5.5) grows more than three orders of magnitude in the range of temperature from $T = 2.0$ to $T = 0.85$, exhibiting a non-Arrhenius upward concavity which is typical of fragile glassformers [10]. Conversely, the growth of the secondary relaxation time (right panel in Fig.5.5) is less pronounced (approximately two and a half decades in the same tempera-

ture range) and the deviations from an Arrhenius behavior are weaker, in particular for the system with stronger secondary relaxation ($l_0 = 0.48$, red symbols).

5.3.2 Monomer mobility

With the aim of further characterizing the dynamics of the two polymer melts with chains having distinct bond lengths, we now consider the monomer mobility, as quantified by the mean square displacement (MSD)

$$\langle r^2(t)\rangle = \frac{1}{N}\sum_{i=1}^{N}\langle \|\mathbf{x}_i(t) - \mathbf{x}_i(0)\|^2\rangle, \tag{5.10}$$

where $\mathbf{x}_i(t)$ is the position of the i-th monomer at time t. Fig.5.6 shows MSD curves for the two systems at all the investigated temperatures. At very short times (ballistic regime) MSD increases according to $\langle r^2(t)\rangle \cong (3k_BT/m)t^2$. At later times a quasi-plateau region becomes apparent when the temperature is lowered. This signals the increased trapping of a particle in the cage of its neighbors. Once escaped from the cage, due to the presence of the chain connectivity, the monomers undergo a sub diffusive motion $\langle r^2(t)\rangle \propto t^\delta$ with $\delta < 1$ (Rouse regime) [49]. At very long times, monomers displace in a diffusive way ($\delta = 1$). Diffusion is hardly seen in our simulations since, due to the length of the chains, it occurs at the limit of the accessible timescales.

5.3.3 Cage dynamics and correlation with primary and secondary relaxations

To identify a characteristic timescale of the cage dynamics we consider the slope of MSD in the log-log representation

$$\Delta(t) \equiv \frac{\partial \log\langle r^2(t)\rangle}{\partial \log t}. \tag{5.11}$$

The slope $\Delta(t)$ is plotted in the insets of Fig.5.6. $\Delta(t)$ tends to 2 at very short times, due to the ballistic motion. Then, it drops to a minimum value signaling effective trapping in the cage. Later, $\Delta(t)$ increases—staying less than 1 due to the Rouse sub-diffusion—with a progressive approach to the unit value characterizing the diffusive regime. The minimum occurs at $t^* \approx 1$ independently of both the system and its physical state. It offers a convenient definition of the monomer DW factor $\langle u^2\rangle$, which, let us recall, can be defined as the MSD at t^*[95, 131]

$$\langle u^2\rangle \equiv \langle r^2(t = t^\star)\rangle. \tag{5.12}$$

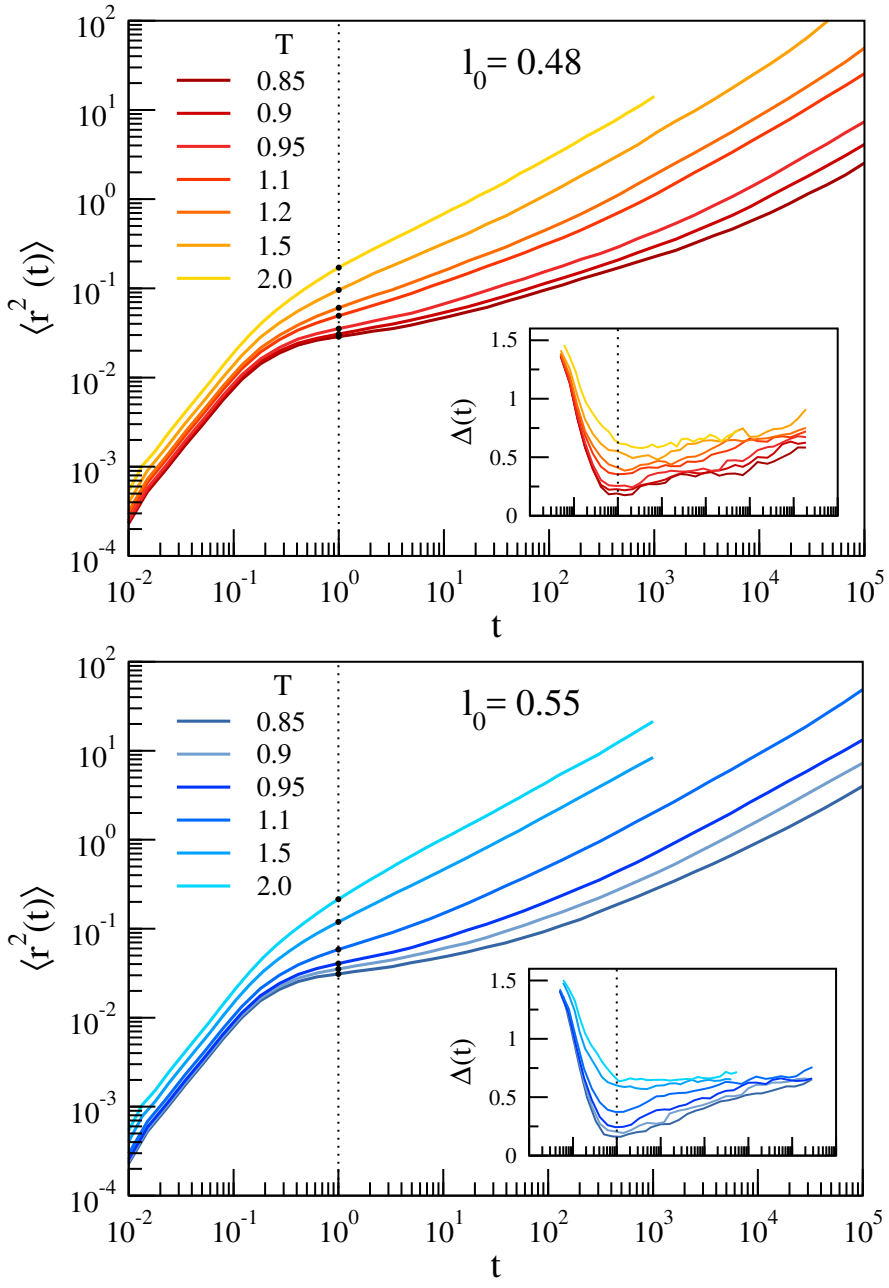

Figure 5.6: Monomer mean square displacement (MSD) of the two polymer melts with chains having bond lengths $l_0 = 0.48$ (top) and $l_0 = 0.55$ (bottom). Inset: corresponding MSD slope $\Delta(t)$, Eq.5.11. The vertical dashed lines mark the time $t^* \approx 1$ where $\Delta(t)$ reaches the minimum, locating the time where caging is more effective. t^* is found to be independent of both the system and its physical state. The black dots indicate the values of $\langle u^2 \rangle$, Eq.5.12.

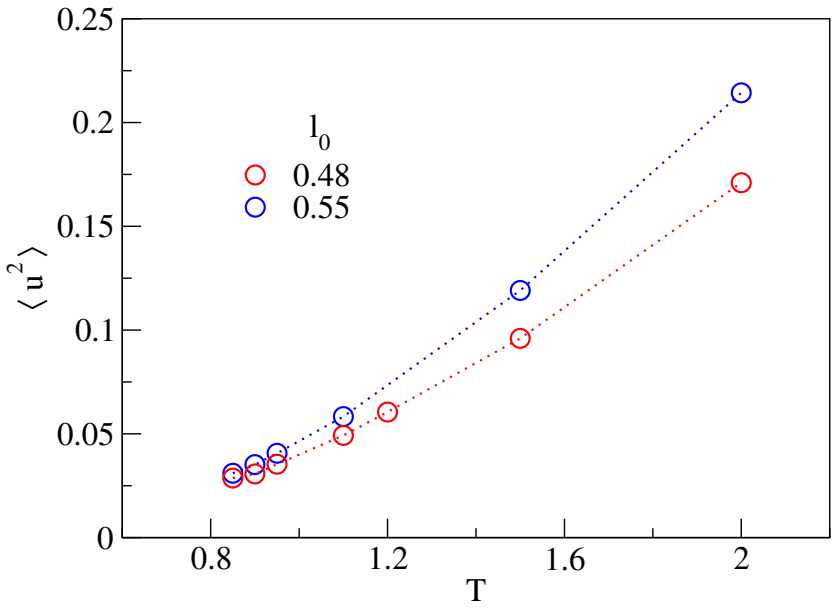

Figure 5.7: Temperature dependence of the Debye-Waller factor $\langle u^2 \rangle$. Color code as in Fig.5.1.

The position of $\langle u^2 \rangle$ is marked in Fig.5.6 with black circles. We remind that the DW factor provides a measure of the rattling motion of the monomer in the cage of the first neighbors. The temperature dependence of DW is reported in Fig.5.7. The dependence is *not* linear evidencing that, even at very short time scales, that is, $t^* \approx 1$ (corresponding to a few picoseconds [95], see also Reference [117]), the rattling of the monomer in the cage is *not* harmonic. Notably, the two systems exhibit different curves for $\langle u^2 \rangle$. In particular, at fixed temperature the system with chains having longer bond length exhibits larger DW factor.

We are now in a position to test the correlation between the vibrational dynamics and the relaxation. Recently, this correlation has been examined in great detail as far as the *primary* relaxation is concerned [95]. It was found that numerical models not providing appreciable secondary relaxations exhibit striking agreement with experimental data of polymers where the presence of JG relaxation is known, like 1,4 Polybutadiene, Polyvinylchloride and Polymethylmethacrylate [14, 107, 110, 111]. This finding needs clarification since the secondary relaxation acts at an intermediate time scale between the fast vibrational dynamics and the primary relaxation and it could, in principle, interfere with the correlation.

To address this aspect, Fig.5.8 plots the correlation between the average relaxation times and the DW factor. As major result, it is clearly seen

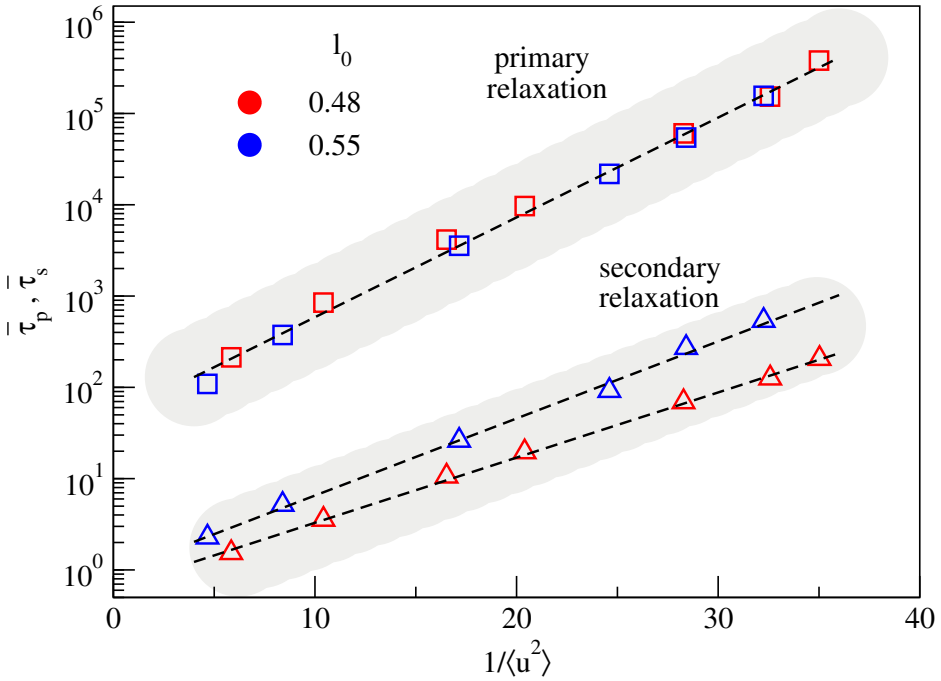

Figure 5.8: Average relaxation times $\overline{\tau}_p$ and $\overline{\tau}_s$ versus the inverse Debye-Waller factor. The correlation between the vibrational dynamics and the primary relaxation time $\overline{\tau}_p$ is unaffected by the changes of both the strength and the relaxation time of the secondary relaxation, see Fig.5.4. Color code as in Fig.5.1.

that the correlation between the fast vibrational dynamics and the primary relaxation is *not* affected by the presence of the secondary relaxation. In fact, data concerning the systems exhibiting either strong ($l_0 = 0.48$) or weak ($l_0 = 0.55$) secondary relaxation exhibit the *same* master correlation curve $\overline{\tau}_p$ vs $\langle u^2 \rangle$. Notably, this coincidence takes place even if the correlation curves $\overline{\tau}_s$ vs $\langle u^2 \rangle$ do depend on the bond length.

Moreover, we observe that the correlation between the primary relaxation and the DW factor of *distinct* systems is usually seen in terms of the reduced DW factor $\langle u^2 \rangle / \langle u_g^2 \rangle$ to get rid of specific system-dependent aspects, $\langle u_g^2 \rangle$ being the DW factor at the glass transition temperature [95]. Fig.5.8 shows that the correlation of the two systems under investigation is rather high by considering the unscaled DW factor. This suggests that, even if the glass transition of the two systems is *different* due to the different temperature dependence of the primary relaxation times, see Fig.5.5(left), the DW factor at the glass transition of the two systems is *equal* within the errors.

5.3.4 Alternative probe functions of secondary relaxation

Correllation functions

The present study reveals the JG relaxation via the BCF $C(t)$, Eq.5.6. We pose the question of the JG sensitivity of alternative relaxation functions. We focus here on the familiar intermediate scattering function (ISF) [77, 95] and the torsional autocorrelation function (TACF) [27]. Bearing in mind that ISF is defined as [77]:

$$F_s(q,t) = \frac{1}{N}\langle \sum_{i=1}^{N} e^{i\mathbf{q}\cdot(\mathbf{x}_i(t)-\mathbf{x}_i(0))}\rangle. \tag{5.13}$$

In an isotropic liquid, the ISF depends only on the modulus of the wavevector $q = ||\mathbf{q}||$ and features the rearrangements of the spatial structure of the fluid over the length scale $\sim 2\pi/q$. As alternative relaxation function, the segmental relaxation has been characterized by TACF [27]:

$$TACF(t) = \frac{1}{N_c}\frac{1}{M-3}\sum_{n=1}^{N_c}\sum_{m=1}^{M-3}\frac{\langle|\varphi_{m,n}(t)||\varphi_{m,n}(0)|\rangle - \langle|\varphi_{m,n}(0)|\rangle^2}{\langle|\varphi_{m,n}(0)|^2\rangle - \langle|\varphi_{m,n}(0)|\rangle^2}, \tag{5.14}$$

where $|\varphi_{m,n}(t)|$ is the modulus of the m-th dihedral angle of the n-th chain at a given time t [27, 92]. The dihedral angle features the torsion of a given bond. Terminal bonds are not subject to torsion, therefore in a chain of length M there are $M-3$ dihedral angles. A graphical representation of this angle is given in Fig.5.9: φ is given from the intersection of the two planes defined by four consecutive monomers in a chain: the first plane is defined considering the first set of three monomers while the second one is defined by the last set of three.

Fig.5.10 compares the BCF $C(t)$ with TACF at the lowest investigated temperature ($T = 0.85$, where the primary and the JG relaxation are expected to have the largest separation). A distinctive feature of $C(t)$ at that temperature is the presence of the step at $t \sim 4 \cdot 10^3$, signalling the secondary relaxation, see Fig.5.10. The step is clearly visible when $C(t)$ drops $\sim 40\%$ only. Fig.5.10 shows that the same step is also observed in TACF but when more than $\sim 90\%$ of the decay has been completed. Namely, it is harder to be observed. Fig. 5.11 plots ISF for different wavevectors in a range including $q = q_{max} \sim 2\pi/\sigma$, corresponding to the maximum of the static structure factor. It is seen that there is no evidence of the two-step decay observed in the BCF $C(t)$ at the same temperature, see Fig.5.10. The results presented in Fig.5.10 and Fig.5.11 are not unexpected. Previous MD

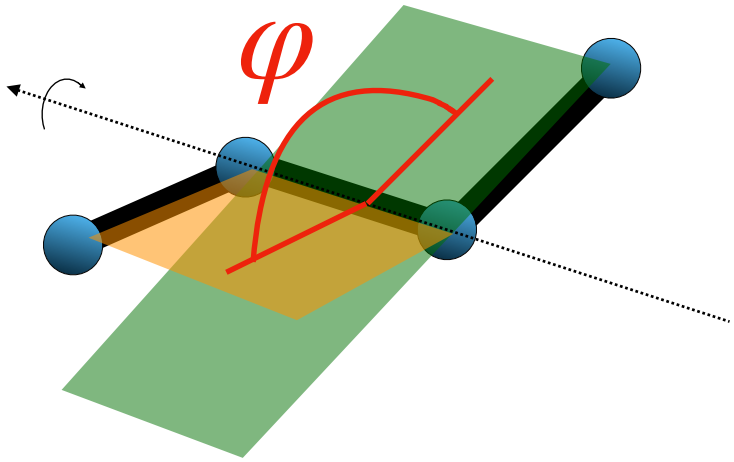

Figure 5.9: Representation of the dihedral angle, φ, characterizing the torsion of the central bond. Angles formed by two adjacent bonds are kept fixed by the bending potential described in Eq.5.4.

studies [26] performed by using the same model of the present work (dubbed FRC model in Reference [26]) reported that ISF needs lower temperatures to reveal a two-step process in the relaxation. This suggests that ISF has lower JG resolution.

The ability to resolve in a limited time and temperature range both the primary and the secondary relaxation is related to their relative separation in time scale as well as to their relative strength. Concerning ISF, timescale separation is possible exploring high wavevector q, in order to be more sensitive to local and restricted dynamics, but the relative strength is also affected by this choice [15]. As recently shown [38], the microscopic density correlation function is dominated at short times by spatial fluctuations of some molecules within the cage formed by the nearest neighbors, that is, by rattling motions within the cage. Conversely, at longer times, part of the relaxation strength is related to large spatial fluctuations extending at least up to the intermolecular distance, i.e. outside the cage. The faster type of motion has been identified as the secondary, while the slower and more intense is the primary one. Timescale separation is usually larger for orientational dynamics, that entails for primary motions a much larger timescale than the intermediate scattering functions (as shown also in Fig. 5.8). In contrast, for the secondary relaxation only local and fast rearrangements are probed by both observables (if the correct wavevector q is chosen). Again, $C(t)$ is much more sensitive than ISF to the presence of secondary relaxation because the relative strength is dominant. Indeed, secondary processes are characterized by rare (but not negligible) and fast rearrangements, resulting

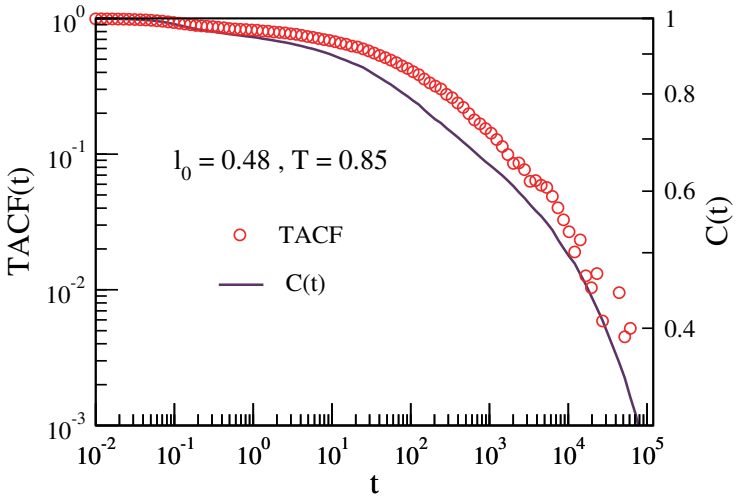

Figure 5.10: Comparison between the torsional autocorrelation function (TACF) and the bond-orientation correlation function, $C(t)$ for the system with stronger secondary relaxation ($l_0 = 0.48$) at the lowest investigated temperature ($T = 0.85$). Notice the step observed in both functions at $t \sim 4 \cdot 10^3$, signalling the secondary relaxation, see Fig.5.2, top. The step is much more apparent in $C(t)$, occurring when the latter is dropped of $\sim 40\%$ only. The same feature is observed in TACF when more than 90% of the decay has been completed.

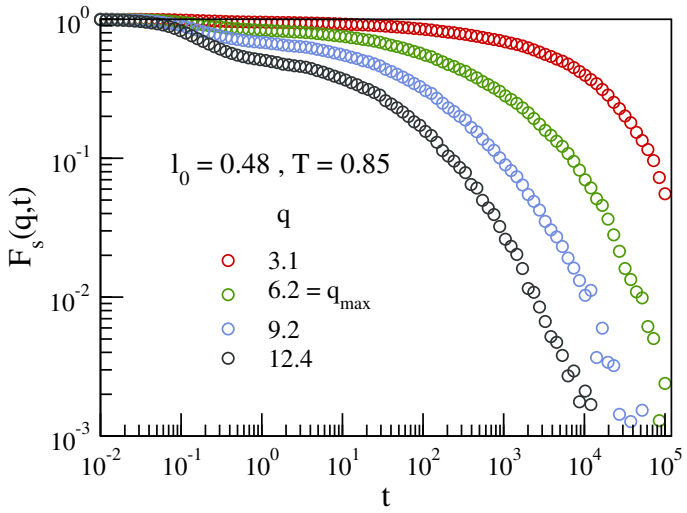

Figure 5.11: Intermediate scattering function (ISF) for different wavevectors in a range including $q = q_{max}$, corresponding to the maximum of the static structure factor, for the system with stronger secondary relaxation ($l_0 = 0.48$) at the lowest investigated temperature ($T = 0.85$). No apparent two-step decay is seen.

in large-amplitude angle motions, which bring a considerable decorrelation of the orientation function [64]. For these reasons orientational correlation function is usually much more sensitive to detect and resolve secondary motions with respect to intermediate structure function or density autocorrelation function. This has been demonstrated by experiments and numerical simulation studies [63, 133, 157].

Mutual information

A valid and very promising alternative way to probe for the presence of a secondary relaxation is provided by mutual information. The nature of secondary relaxations and in particular of JG-relaxation, predisposes it to non-linear correlation between intra-chain degrees of freedom. In our model for example, the JG relaxation involves a local motion of the chain backbone. To uncover its presence, we focused on the reorientation of the bond linking two adjacent monomers in the polymeric chain. However, the reorientation of a given bond at any given time t is not independent from the one of neighbors bonds in the chain. This gives rise to non-linear correlation effects in the bond reorientation. Such effects escape detection when using simple correlation function as $C(t)$. Thus, mutual information might improve the resolution of the same measure.

As in the case of $C(t)$, we focus on the bond reorientation but now we consider the unit vector $\mathbf{b}(t)$, at any given time t, a random variable whose realization are all the unit vectors lying on all the bonds present in the system. We therefore compute the mutual information

$$I(\mathbf{b}(t), \mathbf{b}(0)) \tag{5.15}$$

As in Chapter 3, we employed the Kraskov-Stögbauer-Grassberger estimator (see Appendix B) to compute the mutual information between the vector $\mathbf{b}(t)$ and its origin $\mathbf{b}(0)$. We remind that this quantity represents the amount of information on the bond orientation at $t = 0$ that is passed to the orientation of the same bond at a later time t. Fig.5.12 plots $I(\mathbf{b}(t), \mathbf{b}(0))$ for the system with the stronger secondary relaxation process at all the investigated temperature. $I(\mathbf{b}(t), \mathbf{b}(0))$ presents a faster decay with respect to $C(t)$ but it has better resolution on the two relaxation processes. After a violent drop at very short time, due to the starting monomers ballistic motion, $I(\mathbf{b}(t), \mathbf{b}(0))$ presents two clear regimes corresponding to the primary and secondary relaxation already evidenced by $C(t)$. A comparison of the performance of MI in detecting the double relaxation with respect to the correlation function $C(t)$ for the system with $l_0 = 0.48$ at the lower investigated temperature is

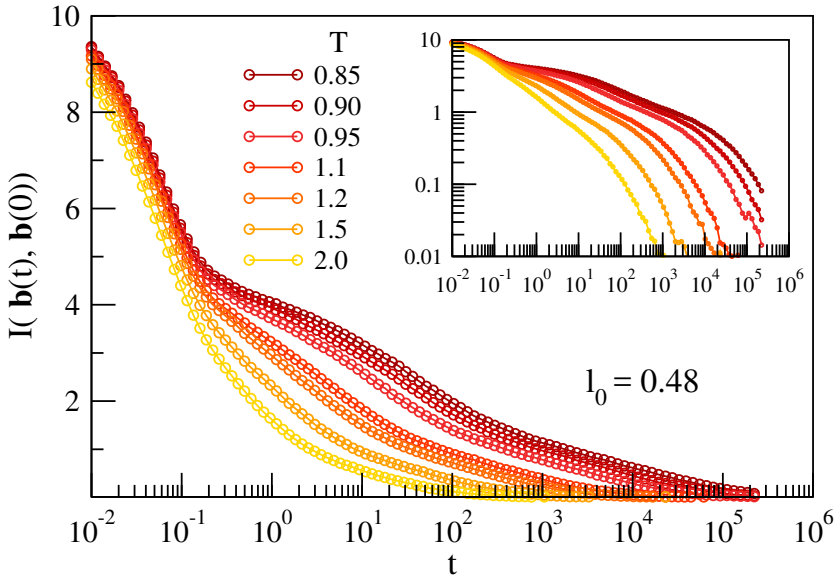

Figure 5.12: Main panel: mutual information (measured in *nats*) $I(\mathbf{b}(t), \mathbf{b}(0))$ between the bond orientation in the starting configuration and the one after a time lapse t for the system with stronger JG-relaxation ($l_0 = 0.48$) at all the investigated temperature. Inset: a log-log plot of the main panel evidencing the double relaxation.

reported in Fig.5.13. For a clearer comparison, Fig.5.13 plots the normalized mutual information

$$\hat{I}(\mathbf{b}(t), \mathbf{b}(0)) = \frac{I(\mathbf{b}(t), \mathbf{b}(0))}{I(\mathbf{b}(0), \mathbf{b}(0))} \tag{5.16}$$

designed to satisfy $\hat{I}(\mathbf{b}(0), \mathbf{b}(0)) = 1$. A first major difference can be observed at very short time where $\hat{I}(\mathbf{b}(t), \mathbf{b}(0))$ present a more abrupt decay with respect to $C(t)$. This is not surprising, as, being $C(t)$ a cumulant, it is unable to capture the decorrelation due to the bond reorientation distribution. At intermediate and long time, we find the two relaxation processes, highlighted in Fig.5.13 by black dashed lines. Remarkably the two relaxation processes appear in both curves at approximately the same time scale. But the secondary relaxation contributes to the 30-40% of the total decay of $\hat{I}(\mathbf{b}(t), \mathbf{b}(0))$ (approximately 70% if one excludes the huge initial drop), in contrast to the correlation function $C(t)$, in which it contributes to the 10-20% of the total decay.

To obtain further insight to the MI performance, we consider the imaginary part of the susceptibility associated to the two quantities $C(t)$ and $\hat{I}(\mathbf{b}(t), \mathbf{b}(0))$. The associated frequency-dependent susceptibility is defined

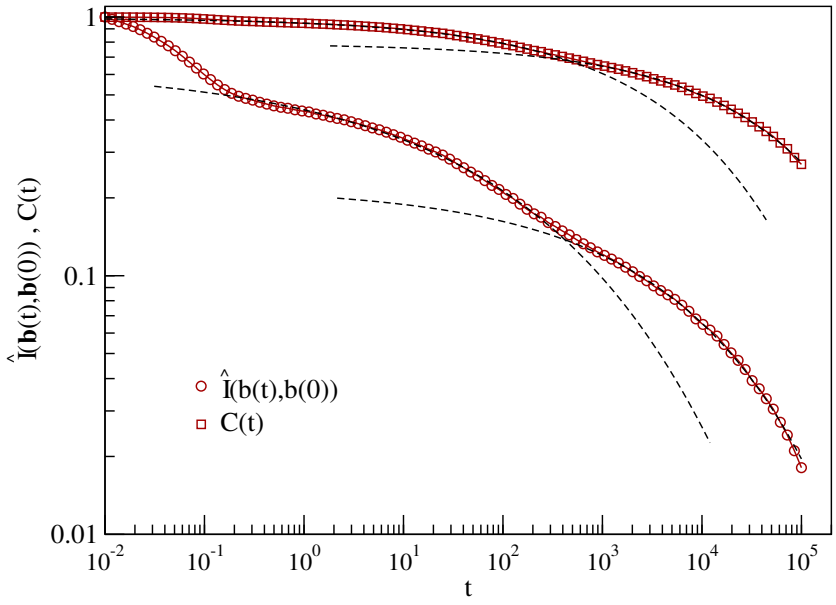

Figure 5.13: Comparison of the correlation function $C(t)$ to the normalized mutual information $\hat{I}(\mathbf{b}(t), \mathbf{b}(0))$, defined in Eq.5.16. Dashed lines superimposed to the curves of $C(t)$ and $\hat{I}(\mathbf{b}(t), \mathbf{b}(0))$ mark the decays corresponding to the two relaxation processes.

as

$$\chi(\omega) = \chi' + i\chi'' = 1 + i\omega \int_0^\infty dt\, e^{i\omega t}\Phi(t) \tag{5.17}$$

where $\Phi(t)$ can be $C(t)$ or $\hat{I}(\mathbf{b}(t), \mathbf{b}(0))$. In Fig.5.14 is reported the comparison of the imaginary part of the susceptibility, $\chi''_{MI}(\omega)$ the one associated with the mutual information (top panel) and $\chi''_C(\omega)$ the one associated with the correlation function $C(t)$ (bottom panel). Although it is not possible to see two split peaks, it is yet possible to note that the major contribution in the imaginary part of the susceptibility associated to the mutual information, $\chi''_{MI}(\omega)$,is given by high frequencies which instead are suppressed in $\chi''_C(\omega)$. Standing out the high and intermediate frequencies contribution, the mutual information offers a natural vantage point of view for detecting the presence of secondary relaxations.

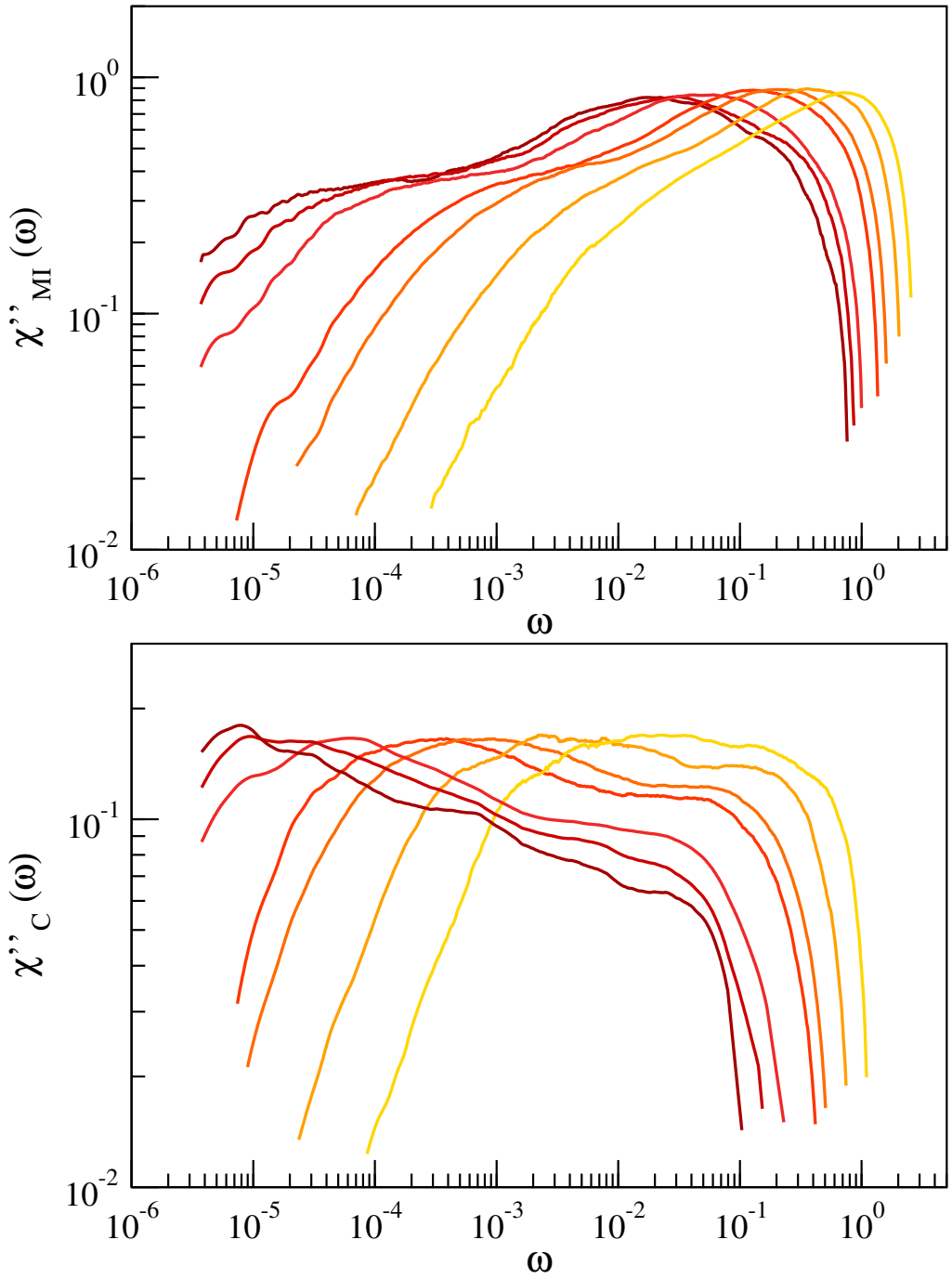

Figure 5.14: Imaginary part of the susceptibility χ'' associated to the two quantities $\hat{I}(\mathbf{b}(t), \mathbf{b}(0))$ (top) and $C(t)$ (bottom) for the system with stronger secondary relaxation at all the investigated temperature.

5.4 Conclusions

We have studied by MD simulations of two melts of polymer chains with different bond length, resulting in rather different strength of the secondary JG relaxation. Our interest is the correlation between the fast vibrational dynamics, as sensed by the Debye-Waller factor, and the slow primary relaxation in the presence of JG relaxation. Multiple relaxation processes were searched by using the bond-orientation correlation function, $C(t)$. We find that changing the bond length alters both the strength and the relaxation time of the secondary relaxation, as well as the correlation with the DW factor. On the other hand, it leaves unaffected the correlation between the vibrational dynamics and the primary relaxation. This finding is in harmony with previous studies reporting that numerical models *not showing secondary relaxations* exhibit striking agreement with experimental data of polymers where the presence of JG relaxation is known [95].

The present result fits into the context of the recent debate about the universality of the correlation between fast and slow degrees of freedom. Actually, a relation between viscous flow and vibrational properties in glass-forming materials has been found in recent studies examining the fragility and the nonergodicity factor, as obtained from scattering techniques in the glassy state [140] and extrapolated to the glass transition region [153]. These two quantities were found strongly correlated only once the effect of secondary relaxation processes, if present, was correctly accounted for. With regards to this issue, it is noteworthy to mention that DW factor as defined in Eq.5.12 is the best definition of cage vibration amplitude, devoid of any further decorrelation due to JG relaxation.

We also carried out an analysis of the performance of alternative probe functions of secondary relaxation. This analysis evidenced that among correlation functions, BCF provides the most efficient probe of secondary relaxation. Its performance is bested only by MI measures that separate better the contribution coming from the two relaxations, being able to take into account non-linear correlation effects.

The findings of the investigation reported in this chapter have been published in the journal Polymers [161].

Chapter 6

Dynamical Heterogeneity in the presence of an emergent β-relaxation process

6.1 Research context

Dynamical heterogeneity (DH) is a central concept to understand the glass-formers dynamics [59, 143]. As mentioned in Chapter 1, DH is characterized by the formation of transient domains, cluster of monomers, with rather different mobility.

There is a general consensus on its connection with the fast heterogeneous vibrational dynamics and slow structural relaxation [131]. In particular, microscopical pictures conjecturing the link between the short-time dynamical heterogeneity and the structural relaxation involve thermally-induced hopping over saddle point in the potential energy landscape [68, 138, 150]. Whether there exists a similar link between the short-time dynamic heterogeneity and the JG β-relaxation, it is still matter of debate [170].

In the framework of the potential energy landscape (PEL), it is common to distinguish the transitions that happens between shallow minima, defined by inherent structures (ISs), from transition that happens between deeper minima, that are usually called metabasins (MBs)[47]. Minima corresponding to ISs lives in the surroundings of MBs. In this view, *intrabasin* transitions, which happen between ISs, are associated with local rearrangements and first neighbors cage deformations whereas *intrabasin* transition, that take place between different MBs, involve collective rearrangements of small number of particles. The latter are spatially heterogeneous events and are directly connected to self-diffusion and to the structural relaxation itself.

JG secondary relaxation was believed to be related to intrabasin transitions and therefore it was not obviously relevant to the dynamic heterogeneity. However, recent studies argued that, instead, JG relaxation appears to involve interbasin transitions[41, 99], in a similar way to structural relaxation. Therefore, as conjectured by Goldstein[69], it also should be related to dynamical heterogeneity.

In this chapter, we consider again the systems already studied in Chapter 5, with the knowledge that a secondary JG relaxation emerges as the length of the bond is decreased. Here we focus on the DH of the system as sensed by the non-gaussian parameter. We investigate whether the presence of a well-resolved secondary relaxation could disturb or alter the DH of the system.

6.2 Results and discussions

In the previous chapter, we examined a polymer system showing an emergent secondary relaxation process as its bond length is decreased, ascribable to local rearrangement of the polymer chain backbone. To shed light on the two distinct relaxations, we considered the bond orientation correlation function $C(t)$, defined in Eq.5.6. $C(t)$ evidenced a different behavior when changing the bond length l_0 of the polymers forming the system, from $l_0 = 0.48$ up to $l_0 = 0.55$. In particular, a two step decay becomes evident in the case of the system with a shorter bond. To distinguish the contribution coming from each relaxation process we fitted $C(t)$ with a sum of two stretched exponential (see Sec.5.3). From the analysis of the stretching exponent, we conjectured the possibility that the presence of a not negligible secondary relaxation process could change the degree of dynamical heterogeneity of the system. However, the analysis of the stretching exponent alone is not sufficient to provide robustness to our conjecture. A more detailed view can be obtained looking directly to the DH itself.

6.2.1 Heterogeneous dynamics probed by non-gaussian parameter

Among the most suitable observables to provide a solid quantitative insight into DH, there is the non-Gaussian parameter (NGP) [172]. In fact, the non-Gaussian nature of the probability distribution of particles displacements in the supercooled temperature regime in glass-forming liquids is believed to be one of the major hallmarks of DH on approaching glass transition [32].

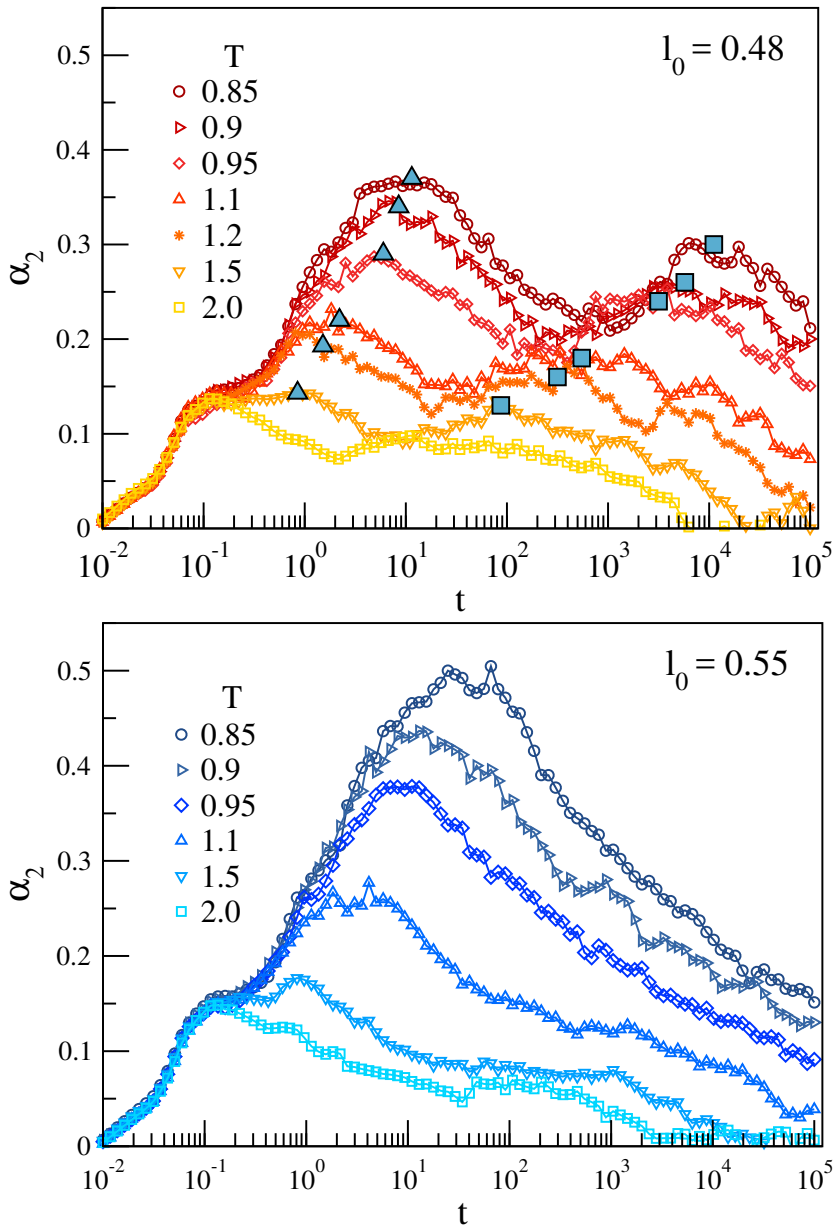

Figure 6.1: Temperature dependence of the NGP for the two studied systems. The one with a shorter bond length l_0 shows a bimodal structure organized in two peaks vanishing at high temperature.

Let us remind that NGP is defined as

$$\alpha_2(t) = \frac{3}{5}\frac{\langle r^4(t)\rangle}{\langle r^2(t)\rangle^2} - 1 \tag{6.1}$$

NGP vanishes if the monomer displacement $r(t)$ in a time t is a gaussian random process [77] whereas the positive value signals the presence of highly mobile monomers displacing in a time t more than the expectations by the gaussian distribution. Fig.6.1 shows the temperature dependence of NGP in the two polymer melts under study. We see that they are quite similar at high temperature, being rather small at short and long times. This is interpreted as consequence of the gaussian character of the ballistic and diffusive motion, respectively. A small peak is observed at $t \sim 0.1$, when the monomer hits the cage of the first neighbors[44]. For $t \lesssim 0.2$ the time evolution of $\alpha_2(t)$ is nearly *temperature-independent*. At longer times, $\alpha_2(t)$ depends on temperature in a more marked way and exhibits a pattern which is rather different in the two polymeric systems. In fact, the melt with chains having longer bond length exhibit a single peak increasing by lowering the temperature, whereas, the one with shorter bond length shows a clear bimodal structure developing in two well resolved peaks.

By comparing Fig.6.1 with Fig.5.6, a clear correspondence between the

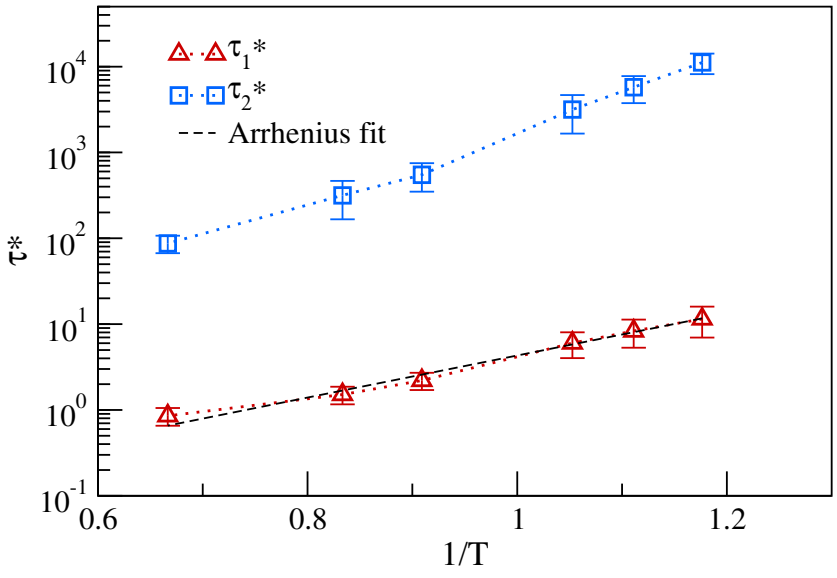

Figure 6.2: Temperature dependence of the two NGP peaks. The temperature dependence of the first peak (red triangles) is compatible with an Arrhenius behavior thus indicating its relation to the JG-relaxation. Peaks position and error bars are obtained considering a parabolic fit within the relevant intervals.

peaks position of the NGP, $\alpha_2(t)$, and the knees observed in $C(t)$ is seen. This strongly suggests that the two peaks observed in NGP for $t \gtrsim 0.2$ have to be associated to the presence of the primary and the secondary relaxation. This interpretation is consistent with the missing bimodal pattern in the system with longer bond length where the secondary relaxation is not well resolved. We stress that the marked change of the time evolution of $\alpha_2(t)$ is just due to a rather limited change in the bond length ($\sim 14\%$). The different nature of the two processes detected by NGP in the system with shorter bond length is also apparent in their distinct temperature dependence, being more marked for the peak observed at longer times (see Fig.6.2). In particular, the temperature dependence of the first peak position is compatible with an Arrhenius behavior indicating its connection with the JG-relaxation process. This lead us to think that the presence of a JG-relaxation process is somehow related to a mechanism that helps recover a homogeneous gaussian character of the particles displacements distribution.

6.2.2 Equal temperature comparison

Non-gaussian parameter

For a better understanding of this topic, it is convenient to compare directly the relevant observables for the two systems, $l_0 = 0.48$ and $l_0 = 0.55$, at the same temperature. In particular, we focus on the lowest investigated temperature, $T = 0.85$, where the separation between the two relaxation times is at its maximum.

Fig.6.3 compare the NGP curves of the two investigated system. This plot allows to identify three well defined time windows within the whole observed time interval:

- **region I** for $t \lesssim 2$, in which the two NGP curve have equal time dependence
- **region II** for $2 \lesssim t \lesssim 7 \times 10^2$, in which the system with a stronger JG-relaxation shows a lower NGP, i.e. a weaker DH. In particular, after reaching a lower maximum, it reaches a local minimum. The system with longer bond length shows instead a normal behavior[115]
- **region III** for $t \gtrsim 7 \times 10^2$, in which the DH of the system with stronger JG-relaxation grows again to the point of exceeding the one of the other system. It then reaches a second maximum and finally decays. Conversely, the NGP of the system with longer bond length decreases monotonously

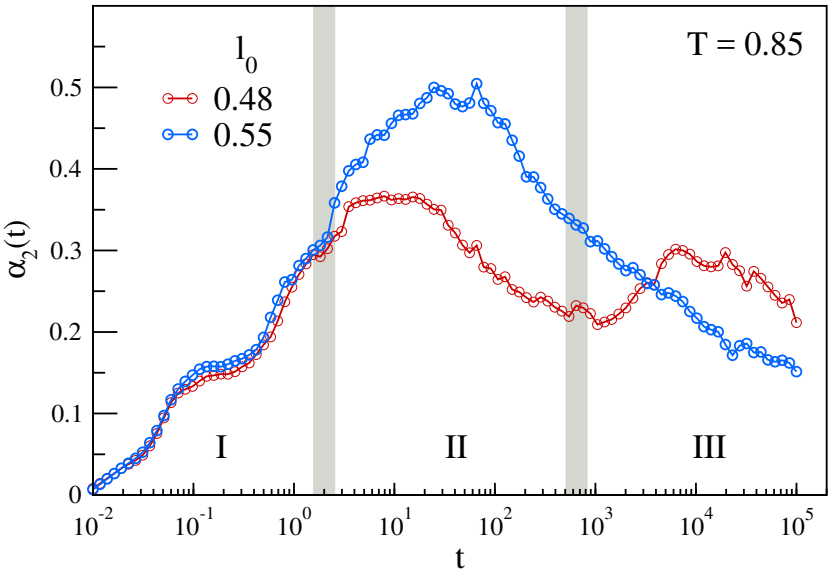

Figure 6.3: Direct comparison of the NGP curves for the two studied system, $l_0 = 0.48$ and $l_0 = 0.55$, at the lowest investigated temperature $T = 0.85$. This comparison allows a division of the investigated time interval in three time region on the basis of the mutual behavior of the two NGP curves: a first region in which the time dependence is coincidental, a second one, in which the system with shorter bond shows a lower DH, and a third one in which the DH of the system with short bond length grows again to the point of exceeding the other system one.

We now are in a position that allow us to investigate on the microscopical origin of this DH reduction mechanism by analyzing the behavior of backbone rearrangement, relaxation and transport relevant observables (such as BCF, ISF and MSD) within the aforementioned time windows.

Bond correlation function

Fig.6.4 shows a direct comparison of the BCF for the two system a the same temperature, $T = 0.85$ the lowest investigated. In the first time window the decay of $C(t)$ for the two system is comparable. At later times, instead, the effect of changing the bond length appears. In fact, in the second time region the system with shorter bond ($l_0 = 0.48$) presents a faster decay of the bond orientation correlation function. This faster decorrelation showed by the first system is ascribable to the JG relaxation itself, made quicker by the shortness of the bond length which facilitates local segment reorientation. As a matter of fact, we observe that, trivially, a shorter segment is able to rearrange its orientation more easily than a longer one within the same available volume.

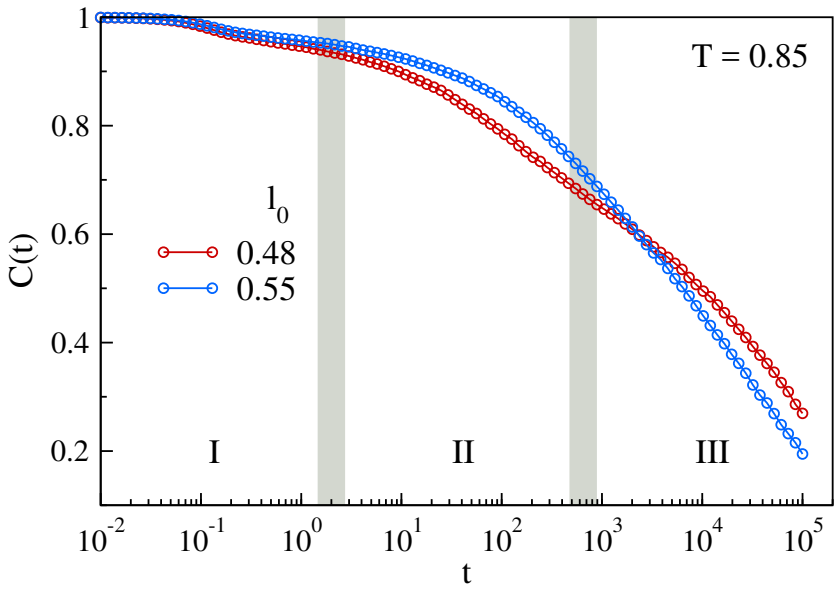

Figure 6.4: Comparison of the bond orientation correlation function for the two studied system, $l_0 = 0.48$ and $l_0 = 0.55$, at the lowest investigated temperature $T = 0.85$. The three time region obtained analyzing the NGP behavior are also evidenced.

In the third time region, a slower decay rate of $C(t)$ is observed for the $l_0 = 0.48$ system. Such a slowdown is accompanied by an increase of DH as probed by NGP (see Fig.6.3). This suggests that the shortness of the bond predispose the formation of transient condition that allow a fast yet partial reorientation of the bond vector at short time. Further decorrelation is achieved only al later time as the latter condition is overcome. This aspect will be discussed later in this chapter.

Intermediate scattering function

The behavior of the bond orientation correlation function in the time regions evidenced by the NGP, is partially reflected on the intermediate scattering function (ISF), defined by Eq.5.13, which is a single-particle observable, as opposed to $C(t)$. A comparison of the two systems ISFs at the same temperature is reported in Fig.6.5. ISFs are almost superimposable in the first and in most of second region.

At $t \approx 1$, the $l_0 = 0.48$ system ISF shows a higher plateau compared to the $l_0 = 0.55$ system ISF. This can be explained by the fact that the shorter bond results in a higher packing of the central monomer and thus in a slower initial dynamics. At intermediate time, in the second time region, the JG-relaxation

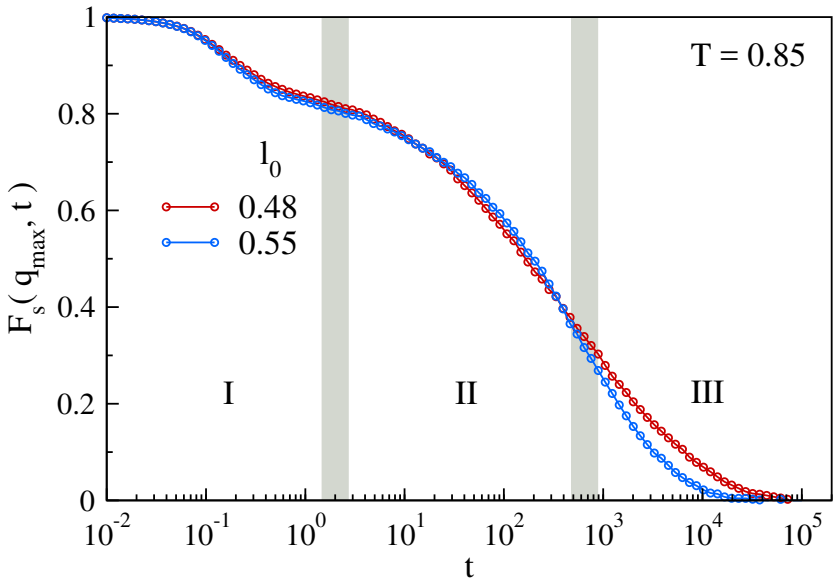

Figure 6.5: Comparison of the intermediate scattering function for the two studied system, $l_0 = 0.48$ and $l_0 = 0.55$, at the lowest investigated temperature $T = 0.85$. The three time region obtained analyzing the NGP behavior are also evidenced.

comes into play. As discussed before, in this time region, the bonds of system with shorter bond-length decorrelate faster from the starting configuration. This faintly reflects on the ISFs curves: in this regime $l_0 = 0.48$ system ISF slightly stands below its counterpart of the $l_0 = 0.55$ system.

Hence, the condition that gives rise to a JG relaxation allowing rapid reorientation of the bonds forming the polymer chain, appears to slightly facilitate at the same time the rearrangement of the particles at the monomers diameter length scale.

Parallel to the behavior of $C(t)$ and concomitantly to the increase of the NGP, in the third region, the system with $l_0 = 0.48$ shows a slower ISF decay when compared to the system with $l_0 = 0.55$. This implies that, in the system with a shorter bond length, at long times, the slowdown of the bond reorientation dynamics affects the rearrangement of the spatial structure of the system at the monomers diameter length scale.

Mean square displacement

This matter can also be addressed considering MSD, defined as in Eq.5.10, for which a behavior similar to the one of the ISF is observed. Figure 6.6 reports the two systems MSD curves at the lowest investigated temperature.

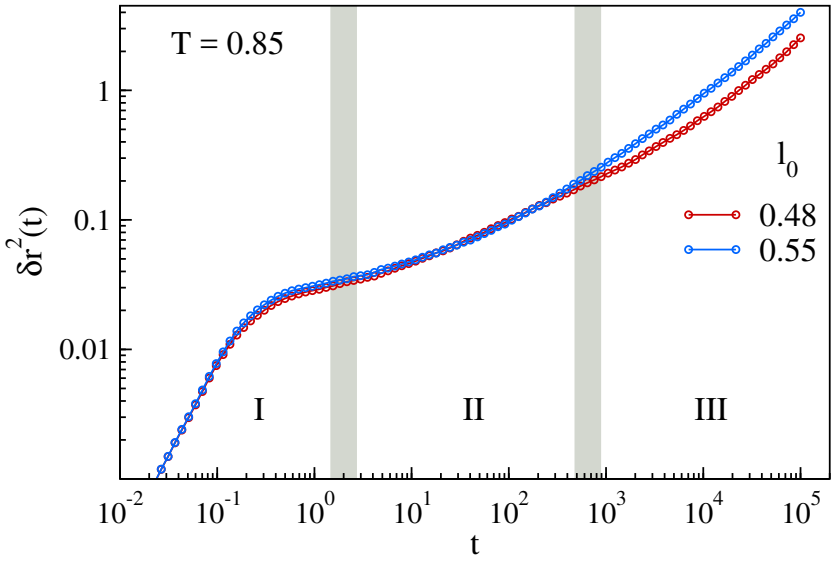

Figure 6.6: Comparison of the mean square displacement curves for the two studied system, $l_0 = 0.48$ and $l_0 = 0.55$, at the lowest investigated temperature $T = 0.85$. The three time region obtained analyzing the NGP behavior are also evidenced.

In the first region of the observed time interval, at very short times, the two MSD curves coincide, trivially because the two systems have the same temperature. Around $t \approx 1$, the $l_0 = 0.48$ system exhibits a slightly lower MSD (resulting in the lower $\langle u^2 \rangle$ discussed in Chapter 5). This might be explained, as already discussed for the ISF plateau, considering the higher packing due to the shorter bond length. In the second time region, the effect of JG-relaxation becomes relevant in the system with shorter bond, thus the acceleration in the bonds reorientation carries with it the MSD filling the initial small gap with the longer bond system. In the third and last region, as seen in ISF, we observe a considerable separation between the two systems MSD. In particular, the shorter bond system shows a delayed diffusive regime with respect to the other.

As a final remark, note that the position of the minimum between the two maxima of the NGP, corresponding to the starting point of the third time region, marks exactly (in order of figures): i) the inflection point of the bond reorientation correlation function $C(t)$ (see Fig.6.4); ii) the time at which ISF (see Fig.6.5) and MSD (see Fig.6.6) curves separates.

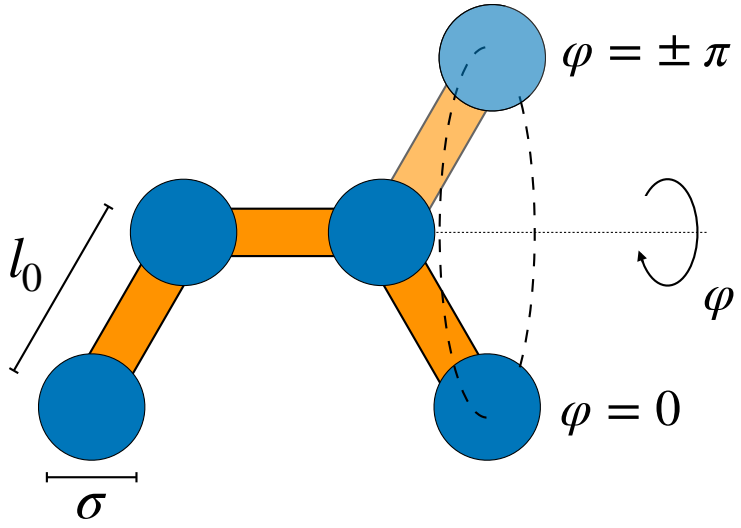

Figure 6.7: Schematic representation of a segment of the polymeric chain model adopted in this work. Depicted length are not in scale to evidence the segment conformation. The dihedral angle φ is given by the intersection of the two planes defined by the first and last three monomers of the considered chain segment.

6.2.3 Microscopical picture

As proven by the previous analysis, the presence of a JG-relaxation mechanism, i.e. the rearrangement of the chain backbone, has a considerable influence on monomers displacement distribution, strongly affecting the non-Gaussian behavior and thus the DH, and averages changing ISF and MSD time dependence. The mechanism that makes possible such a connection should of course be sought on the parameter that we tuned in order to turn on the JG-relaxation, i.e. the bond length.

Let us consider a segment of our polymeric chain formed by 4 subsequent monomers. We remind that angles between bonds are kept constant at $2\pi/3$ by the bending potential defined in Eq.5.4. As a consequence, the only degree of freedom able to rearrange the polymeric chain backbone is the torsional one. Let us now freeze the first three monomers and consider only the motion of the last segment. This allows to consider the reorientation of this last bond in terms of the dihedral angle φ formed by the two planes defined by the first and last three monomers of the segment considered. Fig.6.7 presents a graphical representation of the considered chain segment giving particular emphasis to the dihedral angle φ, defined in Sec.5.3.4.

Let us now consider the LJ interaction between the first and last monomer of the considered segment as the dihedral angle φ is changed. The distance between the first and last monomer can be easily be written as a function of

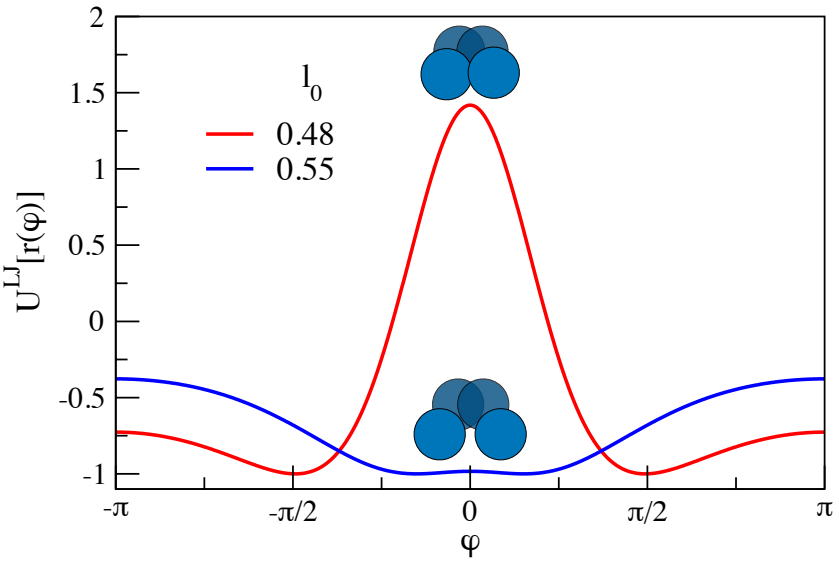

Figure 6.8: Effective torsional potential generated by the Lennard-Jones interaction between the first and last monomer of the considered segment. An abrupt change in the potential is noted varying the bond length l_0 from 0.55 to 0.48 with the appearance of considerable energy barrier.

φ

$$r_{f-l}(\varphi) = \left[\frac{3}{2}(1-\cos\varphi)+4\right]^{\frac{1}{2}} l_0 \tag{6.2}$$

Considering the monomers as soft balls of radius σ (the 0 of the LJ potential), we note that, in the case of $l_0 = 0.48$ and $\varphi = 0$, the first and last monomer do interpenetrate, since we have $r_{f-l}(\varphi = 0) < \sigma$, while for the $l_0 = 0.55$ they do not. In Fig.6.8 is reported the φ-dependence of the Lennard-Jones interacting potential between the first and last monomer $U^{LJ}[r_{f-l}(\varphi)]$. Note that this potential actually acts as an effective torsional potential influencing the time evolution of the φ angle and therefore the reorientation of the last bond. We observe that for $l_0 = 0.48$, $U^{LJ}[r_{f-l}(\varphi)]$ shows an high energy barrier of approximately 1.5. Such an energy barrier is the one that obstacles a complete reorientation of the bond separating as a consequence the primary and secondary relaxation. The effect of this energy barrier reflects also on monomers displacements. In fact, in this model, due to the bending potential, keeping fixed the angle between two adjacent bonds, the singe monomer displacement is strongly tied to the motion of the segment itself.

At short times, neither the easier rotation nor the energy barrier play a relevant role in monomer displacement distributions and averages. The only relevant effect seen is the reduction of the DW factor as the bond length

is lowered, as a consequence of the higher packing. Considering instead intermediate times, we observe an increase in the role of rotation facilitation due to the shortness of the bond, i.e. $C(t)$ decay faster in the short bond system. This does not reflect on observables related to average on monomers displacement, like ISF or MSD, while it affects the ones depending on their distribution. $l_0 = 0.48$ system monomers, drawing more easily from the bond rotational degreed of freedom, can move more freely within this time region, recovering, as a consequence, part of gaussianity of their displacements distribution. Such a recovery indicates the suppression of the hopping-like motion featuring the right tail of the displacement distribution (the Van Hove function). Therefore, it can be directly associated to a lowering of the DH of the system [32]. At long times and especially at low temperatures, the torsional energy barrier, present in the $l_0 = 0.48$ system, inhibits the rearrangement of the chain backbone, reducing the overall segmental mobility and therefore hindering the monomers motion. As a consequence, we observe a slowdown in observables related to the averages of monomers displacements and an increasing NGP. It is worth highlighting that the marked evidence of the JG-relaxation presence and its effects disappear as the temperature is raised above the energy barrier (see Fig.6.1 and Fig.5.2).

As a further evidence of the microscopical mechanism discussed above, we consider directly the torsional autocorrelation function (TACF). TACF, defined as Eq.5.14, offers the opportunity to look directly how the dihedral angle φ decorrelate over time.

In Fig.6.9, the comparison between the two systems TACF curves at the lowest investigated temperature is reported. The torsional dynamics of the system with shorter bond is of course faster as compared to the one of the other system. This does not allow an immediate comparison of the two curves leading to a sharp understanding of the role of the torsional energy barrier.

Therefore, to obtain a meaningful comparison, its possible to resort to a fit procedure. We assume that the fast secondary relaxation of the TACF can be represented, at least before the third time-region, by a stretched exponential in the form

$$f(t) = Ae^{-\left(\frac{t}{\tau}\right)^{\beta}} \tag{6.3}$$

This relaxation function choice complies with most MD simulation studies dealing with torsional degrees of freedom [26, 27]. At short-intermediate times, the presence of the energy barrier in the system is not yet become relevant. Thus, the behavioral difference between the two TACF curves is due only to the angular velocity difference resulting from changing the rotating segment length. As a consequence, we can consider a fit of the two curves imposing the amplitude A and the stretching exponent β to be equal for

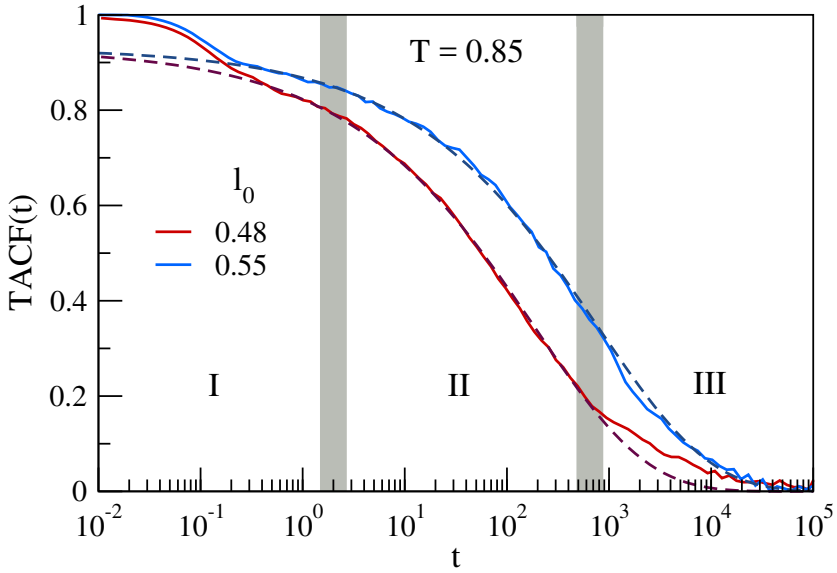

Figure 6.9: Comparison of the TACF curve of the $l_0 = 0.48$ system and the time-rescaled one of the $l_0 = 0.55$ system both at the temperature $T = 0.85$. The three time windows obtained analyzing the NGP behavior are also evidenced. Darker dashed lines represent best fit curves with a single stretched exponential function obtained forcing the amplitude A and the stretching exponent β to be the same in both cases. The fit is carried out considering the third time-window and the fast initial decorrelation due to ballistic monomers motion.

the two system, thus leaving free only the relaxation time τ. The result of this fit is reported in Fig.6.9 (darker dashed lines). As already pointed out in Sec.5.3.4, we observe that the TACF curve of the $l_0 = 0.48$ system shows a deviation from a single stretched exponential behavior at long time, whereas the one of the $l_0 = 0.55$ system is very much compatible with Eq.6.3 even at long times. The deviation from Eq.6.3, happening with a sudden change of slope, by the system with shorter bond length, signals the moment in which the torsional energy barrier has become relevant to the dynamics. Furthermore, we note that the deviation coincides precisely with the start of the third time region, hence corresponding to a novel increase of the NGP and to the separation of the ISF and MSD curves of the two system.

6.3 Conclusions

We have studied by MD simulations two melts of polymer chains with different bond length. Shortening bond length gives rise to a well resolved secondary JG relaxation. Our interest is focused in the connection of the JG

relaxation with the system dynamical heterogeneity. We probed dynamical heterogeneity employing the non-gaussian parameter. We find that the latter is strongly affected by the presence of the JG relaxation. In particular, we observe that NGP shows a bimodal behavior by displaying two peaks at times compatible with the change of slope of the bond-orientation correlation function, $C(t)$, thus evidencing their connection respectively with a faster JG and a slower structural relaxation. The temperature dependence of the two peaks evidence an Arrhenius-like behavior for the first peak and a super-Arrhenius-like behavior for the second one, hence reinforcing their link to the two relaxation processes. Furthermore, we observe that, considering equal temperature, the system with stronger secondary JG relaxation shows a lower DH at short-intermediate times as compared to the other system. At long times, the opposite happens: the DH is higher in the system with stronger JG relaxation.

By comparing the behavior of the time dependence of NGP with ISF and MSD in the two systems, we are able to track down the effect of JG relaxation on the structural relaxation and mobility. We also offer a microscopical picture of the mechanism that gives rise to JG relaxation explaining also its connection with the DH of the system: we observe that shortening the bond length gives rise to a effective torsional energy barrier. This conjecture is supported by the analysis of the TACF.

Outlook

In this Chapter, the main results of the studies presented in the Thesis are briefly summarized, and possible future developments of the work are discussed.

The first research carried out during my Ph.D. involved the study of monomers vectorial displacements correlations in a molecular liquid approaching the glass transition by means of mutual information. The molecular liquid under consideration is a melt of fully-flexible trimers.

Chapter 3 Displacement correlation detected by mutual information were analyzed with the purpose of characterizing the size of the correlated motion. We did this considering the number of correlated particles with a tagged one, the gyration radius of the correlated cluster and the mutual information length scale. None of these quantities is seen growing on approaching the glass transition. However, the mutual information length scale is found coincident to the correlation length obtained considering the correlation function of the displacements direction. This indicates that either mutual information is sensitive only to the direction of the displacement or the decorrelation coming from the latter is predominant to the point of obscuring the information on the displacement modulus.

Chapter 4 Here displacements correlation detected by mutual information are considered from the point of view of their distribution. Such an analysis evidenced two particle fractions with different mobility and relaxation. The two fractions average amplitudes of the particle rattling motion within the cage of the first neighbors and their respective relaxations exhibit a scaling relation that complies with the one observed in bulk systems. An analysis of the local structure, in terms of local density and local particle arrangement, was carried out to look for correlation with the two fractions. Further analysis on the two fractions spatial distribution evidenced their tendency to form localized cluster of growing size on approaching the glass transition. The latter obser-

vation provides a solution to the issue of observing a MI-correlation not growing on approaching the glass transition. In fact, the average gyration radius of these clusters offers a natural length scale for the dynamical heterogeneity. The fractal dimension of the clusters was also computed. We observed that the fast fraction is arranged in less-then-bidimensional clusters while the slow one is arranged in globular (tridimensional) clusters.

The second research tackled during my Ph.D. faced the problem of introducing a secondary relaxation timescale between the fast vibrational one and the slow one dictated by the structural relaxation. The viscous liquid employed for this research is a polymer melt of 25-mers with very short, nearly fixed, bond length, compared to the zero of the Lennard-Jones potential, forcing an overlap between bonded monomers. A bending potential was also considered to keep the angle between consecutive bonds fixed. The secondary relaxation appears as rearrangement of the chain backbone.

Chapter 5 The timescale of the secondary relaxation is intermediate between the vibrational one and the structural relaxation time. It is quite natural to ask whether it can interfere with the scaling relation between them. Therefore, we investigated how the aforementioned scaling relation is modified by the introduction of a Johari-Goldstein secondary relaxation. Such an introduction is controlled by tuning the bond length of the polymer. We verified that the universal scaling relation between the vibrational dynamics and the structural relaxation is preserved. A similar scaling relation is not observed with the Johari-Goldstein secondary relaxation. We also carried out an analysis of the performance of several different functions in detecting the presence of secondary relaxation. We concluded that, among correlation functions, the bond orientation one gives the sharpest response for this kind of systems. Its performance is bested only by considering the mutual information between bond orientations.

Chapter 6 The JG secondary relaxation process was believed to be not directly related to dynamical heterogeneity. However, more and more studies started to build the evidence that the two might actually be correlated. Therefore, in the same systems investigated in the previous chapter, we analyzed the behavior of the dynamical heterogeneity by computing the non-Gaussian parameter of the displacements. The system showing a well-resolved JG secondary relaxation exhibited a bimodal non-Gaussian parameter time dependence, conversely to the usual one shown by the other system. In particular, it displayed two

peaks at times that are compatible respectively with the two relaxations (JG and structural) time scales, thus proving a connection between the JG secondary relaxation and the dynamical heterogeneity. By comparing the behavior of the time dependence of NGP with ISF and MSD in the two systems, we were able to track down the effect of JG relaxation on the structural relaxation and mobility. We also offered a microscopical picture of the mechanism explaining the rise of the JG relaxation when the bond length is changed and also its connection with the dynamical heterogeneity of the system.

Natural developments of the work reported in this thesis could aim to investigate other markers of dynamical heterogeneity, such as the four-point susceptibility, in the system showing a JG relaxation to get further insight on their relation. It could be also interesting to investigate the system showing a JG relaxation employing the mutual information apparatus described in the first part of this thesis. Further studies are also needed to strengthen the claim that mutual information is an improved observable for the detection of a secondary relaxation process.

Appendix A

Information theory observables derivations and properties

A.1 Entropy of a discrete random variable

In this section, we will derive the missing information or *entropy* of a discrete random variable with a finite number W of possible outcomes.

A.1.1 Equiprobable outcomes

Let us suppose that each outcome of the random variable has an equal probability $1/W$. We want to quantify the amount of information needed to correctly guess the value of the random variable. This missing information is the *entropy* of the considered random variable. As discussed in Chapter 2), the problem is conceptually equal to the one of a ball hidden in one of a set of W boxes where we want to guess the position of the ball. A naive strategy could be asking for each box whether or not the ball is there. This would lead to an average of $W/2$ question to guess correctly the position of the ball. The optimal strategy to tackle this kind of problem relies on dividing the entire set of boxes into two sets of $W/2$ boxes and then ask if the ball is in the first or the second set. At this point the possibility are halved. If W is a power of 2, it is trivial to conclude that the number of answers needed to locate the ball is $n = \log_2 W$. Therefore, for the missing information we have

$$H = n = \log_2 W \tag{A.1}$$

In general, W is not a power of 2. Thus, repeating several times the experiment will return different values for n. In this case, we can obtain a proper definition for the missing information considering the average over a large

number of repetitions of the same experiment N_E.

$$H = \langle n \rangle_{N_E} \tag{A.2}$$

In each of these N_E experiments, the ball is hidden in one of the W boxes. Thus, the total number of possible outcomes is W^{N_E}. In each experiment, the number of questions required to locate the ball will be $\lceil \log_2 W \rceil$ or $\lfloor \log_2 W \rfloor$ depending on our luck. Hence, the total number of questions will respect the inequality

$$\lfloor N_E \log_2 W \rfloor \leq n^{tot} \leq \lceil N_E \log_2 W \rceil \tag{A.3}$$

and even more so

$$\lfloor N_E \log_2 W \rfloor - 1 < n^{tot} < \lceil N_E \log_2 W \rceil + 1 \tag{A.4}$$

Identifying the missing information, I, as the *average* number of questions needed, we have

$$H = \langle n \rangle_{N_E} = \frac{n^{tot}}{N_E} \tag{A.5}$$

Thus, dividing Eq.A.4 by N_E, taking the limit $N_E \to \infty$ and then inserting it in Eq.A.5, we finally obtain

$$H = \log_2 W \tag{A.6}$$

A.1.2 Outcomes with a known probability

Let us now suppose that the boxes do not have an equal probability of hiding the ball. The box i has a probability p_i of hiding the ball. It goes without saying that

$$\sum_{i=1}^{W} p_i = 1 \tag{A.7}$$

As in the previous case, let us consider a large number N_E of repetitions of the same experiment. We of course know that the number of experiments in which the ball is found in the box i is $N_E p_i$. What is left to know is the order in which they appear. Thus, the total missing information is simply ascribable to the number of all the possible experiments sorts

$$H^{tot} = \log_2 \frac{N_E!}{\prod_{i=1}^{W} (N_E p_i)!} = \log_2 N_E! - \sum_{i=1}^{W} \log_2 (N_E p_i)! \tag{A.8}$$

Being N_E very large, we can use the Stirling approximation and obtain

$$\begin{aligned} H^{tot} \simeq & N_E \log_2 N_E - N_E - \sum_{i=1}^{W} N_E p_i (\log_2 N_E + \log_2 p_i) + \sum_{i=1}^{W} N_E p_i \\ = & - N_E \sum_{i=1}^{W} p_i \log_2 p_i \end{aligned} \tag{A.9}$$

Thus, the missing information for each experiment, and hence the entropy of a discrete random variable, is [105]

$$H = - \sum_{i=1}^{W} p_i \log_2 p_i \tag{A.10}$$

A.2 Entropy of a continuous random variable

In the case of a continuous random variable, the problem is equivalent to the one of determining the position x of a point within a given interval $a \leq x \leq b$. Let us suppose the existence of probability density function $p(x)$ so that the probability of finding x within the value x_1 and x_2 is

$$W(x_1, x_2) = \int_{x_1}^{x_2} p(x)\, dx \tag{A.11}$$

with

$$p(x) \geq 0 \quad \text{and} \quad \int_a^b p(x)\, dx = 1 \tag{A.12}$$

At this point, to obtain the entropy (missing information), a smart strategy is to discretize the problem and make use of the previous results. Hence, let us divide the interval $[a, b]$ in W equal sized cells. The probability for a cell i to contain the point is

$$\mathcal{P}_i(W) = \int_{a_i(W)}^{b_i(W)} p(x)\, dx = \bar{p_i} \frac{b-a}{W} \tag{A.13}$$

where $a_i(W)$ and $b_i(W)$ are the boundaries of the cell i and $\bar{p_i}$ is the mean value of $p(x)$ within the same cell. The probability $\mathcal{P}_\rangle(W)$ depends, of course,

on the discretization. At this stage we can use Eq.A.10 and obtain

$$\begin{aligned} H(W) &= -\sum_{i=1}^{W} \mathcal{P}_i \log_2 \mathcal{P}_i \\ &= -\sum_{i=1}^{W} \left[\int_{a_i(W)}^{b_i(W)} p(x)\, dx \right] \log_2 \left[\int_{a_i(W)}^{b_i(W)} p(x)\, dx \right] \\ &= -\sum_{i=1}^{W} \frac{b-a}{W} \bar{p}_i \log_2 \bar{p}_i - \log_2 \frac{b-a}{W} \end{aligned} \tag{A.14}$$

At this stage, it is necessary to take the limit for $W \to \infty$ but a problem stands out: the second term of the last raw of Eq.A.14 diverges as $W \to \infty$.

$$\lim_{W \to \infty} -\log_2 \frac{b-a}{W} = +\infty \tag{A.15}$$

Strictly speaking, the amount of information required to define a continuous random variable is infinite. However, the diverging therm in the last raw of Eq.A.14 depends only on the cell dimension, and especially it does not depend on the probability distribution $p(x)$. Hence, the difference between the missing information of two random variables is still a well-defined quantity. Therefore, it is possible to renormalize Eq.A.14, subtracting the diverging term, and define the missing information of a continuous random variable as [105]

$$H = -\int_a^b p(x) \log_2 p(x)\, dx \tag{A.16}$$

Appendix B

Estimating Mutual Information

While the mathematical formulation of the quantities in Chapter 2 is relatively straightforward, empirically estimating them in practice from a finite number N of samples can be a complex process. Here we focus on the estimation of Mutual Information. Typically, one has a set of N measurements, $z_i = \{x_i, y_i\}, i = 1, \ldots, N$, which are assumed to be iid (independent identically distributed) realizations of a random variable $Z = \{X, Y\}$ with joint probability density $p(x, y)$ and marginals $p(x)$ and $p(y)$. For discrete random variables, the definition, given in Eq.2.21, can be used directly by plugging-in the estimated probability

$$\hat{p}(X = x_i) = \frac{n_i^x}{N} \tag{B.1}$$

$$\hat{p}(Y = y_j) = \frac{n_j^y}{N} \tag{B.2}$$

$$\hat{p}(X = x_i, Y = y_j) = \frac{n_{ij}^{xy}}{N} \tag{B.3}$$

obtained counting the matching samples n_i^x, n_i^x and n_{ij}^{xy} . Accordingly, this class of estimators is known as plug-in estimators (or maximum likelihood estimators). Such kind of estimation is fast and simple. Of course, it presents bias and variance for which however there exist some correction techniques [119].

In the case of a continuous random variable instead, the matter gets a bit more complex. The most straightforward approach for estimating MI consists in partitioning the supports of X and Y into bins of finite size, and then approximating Eq.2.22 by the finite sum

$$I(X, Y) \approx I_{binned}(X, Y) = \sum_{i,j} p(i, j) \log \left[\frac{p(i, j)}{p_x(i) p_y(j)} \right] \tag{B.4}$$

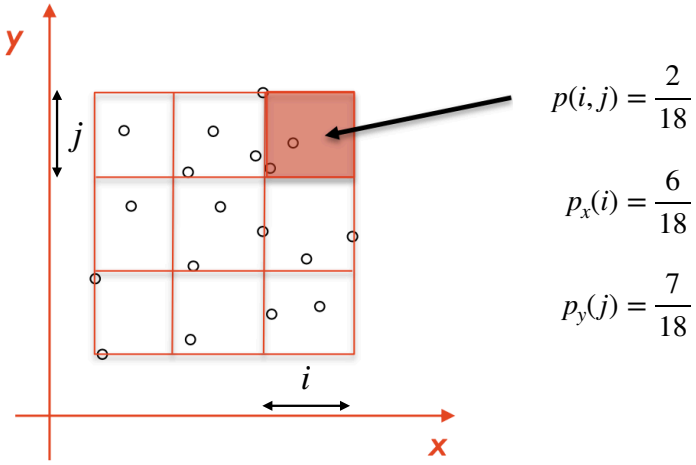

Figure B.1: Discretization example of two random variable, X and Y, supports. The estimates for the probability distribution functions (joint and marginals) are given on the right side of the figure.

where $p(i,j)$, $p_x(i)$ and $p_y(j)$ are the integrals over the binned space (plaquette $i \times j$ or bin i and bin j) of the joint or marginals probability densities (See for example Fig.B.1). The MI estimates obtained with this procedure is far from being optimal. It depends strongly on the binning procedure and is blind to any subtleties of the joint probability distribution happening on a scale shorter than the bin size. If overlooked, these points might result in a poor overall estimate accuracy.

A popular alternative for estimating MI is the class of non-parametric estimators built on the method derived by *Kraskov. et. al.*[90]. Kraskov-Stögbauer-Grassberger (KSG) estimator relies on local geometric information about the sample to approximate the density $p(x,y)$ at each point $z_i = \{x_i, y_i\}, i = 1, \ldots, N$ and then calculates directly a local estimate of (MI) from it. This method relies on *Kozachenko and Leonenko* k-th nearest neighbor entropy estimator[89]. Let us consider a single continuous random variable X with probability density $p(x)$ and a sample of its realizations $x_1, x_2 \ldots x_N$. According to the *Kozachenko* estimators we can write

$$\hat{H}_X = \psi(N) - \psi(k) + \log c_d + \frac{d}{N} \sum_{i=1}^{N} \log \varepsilon_i \tag{B.5}$$

where ψ is the digamma function, d is the dimension of x, c_d is the volume of the d-dimensional unit ball and ε_i is twice the distance from x_i (i-th realization of X) of its k-th nearest neighbor. A demonstration of this result is given in Ref.[90]. A this point, returning to the joint random variable

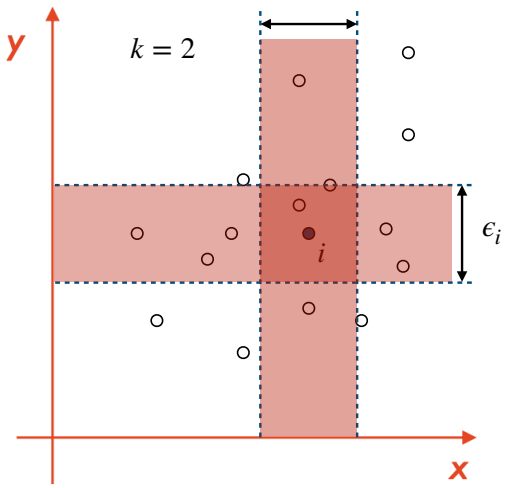

Figure B.2: Determination of ϵ_i, n_i^X and n_i^Y for the mutual information estimator $\hat{I}^{(1)}(X,Y)$ for $k=2$. In this example $n_i^X = 4$ and $n_i^Y = 6$.

$Z = \{X, Y\}$, it is possible to obtain MI by estimating in this way $H(X)$, $H(Y)$ and $H(X,Y)$. For the joint entropy we have

$$\hat{H}(X,Y) = \psi(N) - \psi(k) + \log(c_{d_X} c_{d_Y}) + \frac{d_X + d_Y}{N} \sum_{i=1}^{N} \log \varepsilon_i \tag{B.6}$$

Thus what seems to remain to be done is subtracting to the sum of the estimated entropies $\hat{H}_X$ and $\hat{H}_Y$, obtained via Eq.B.5, to Eq.B.6 using in all the estimate the same k. But this procedure would result in a summation of the biases of all the estimates. To avoid this, keeping in mind that Eq.B.5 holds true for any k, a few smart choices can be made.

First of all, we consider the max norm as a metric in the joint space

$$||\mathbf{z} - \mathbf{z}'|| = \max\{||\mathbf{x} - \mathbf{x}'||, ||\mathbf{y} - \mathbf{y}'||\} \tag{B.7}$$

Thus let us denote by $\epsilon_i/2$ the distance from z_i to its k-th neighbor and by $\epsilon_i^X/2$ and $\epsilon_i^Y/2$ the distance in the two subspace X and Y. Of course we have $\epsilon_i = \max\{\epsilon_i^X, \epsilon_i^Y\}$. At this point, we count n_i^X, the number of points x_j whose distance from x_i (the tagged point) is strictly less than $\epsilon_i/2$, and n_i^y in a similar way for the Y subspace. This procedure is illustrated in Fig.B.2. Now, we fix the k the estimator of the joint entropy, $\hat{H}(X,Y)$, and chose $k = k'$ in the estimator of the entropy of X so that the k-th neighbor of a given sample i in the joint distribution coincide with the k'-th neighbor of the same sample i in the X subspace. We have therefore $k' = n_i^X + 1$ and for

the entropy estimator

$$\hat{H}_X = \psi(N) - \frac{1}{N}\sum_{i=1}^{N}\psi(n_i^X + 1) + \log c_d + \frac{d}{N}\sum_{i=1}^{N}\log \varepsilon_i \tag{B.8}$$

Similar reasoning applies to the Y subspace. Substituting X with Y in Eq.B.8, gives a reasonable approximation of $\hat{H}_Y$. It is an approximation since in general ϵ_i could not match exactly to twice the distance from the $[n_i^Y + 1]$-th neighbor in the Y subspace or the $[n_i^X + 1]$-th neighbor in the X subspace. If we now combine $\hat{H}(X)$, $\hat{H}(Y)$ and $\hat{H}(X,Y)$ as in Eq.2.20 we obtain the estimator for the mutual information

$$\hat{I}^{(1)}(X,Y) = \psi(k) + \psi(N) - \left\langle \psi(n^X + 1) + \psi(n^Y + 1) \right\rangle \tag{B.9}$$

the average $\langle \ldots \rangle$ is taken considering all $i \in [1, \ldots N]$ and all the realization of the sample. The fact that the length scale, imposed by the choice of k, now matches in all the three estimators $\hat{H}(X)$, $\hat{H}(Y)$ and $\hat{H}(X,Y)$ gives a chance to the errors to cancel (even if not exactly) when combined.

Alternatively, there exists another KSG estimator of the mutual information which is similar to the one obtained above but with a few modifications. In the second estimator n_i^X and n_i^Y are replaced by the number of points with $||x - x_i|| \leq \epsilon_i^X/2$ and $||y - y_i|| \leq \epsilon_i^Y/2$. The mutual information estimator is

$$\hat{I}^{(2)}(X,Y) = \psi(k) - \frac{1}{k} + \psi(N) - \left\langle \psi(n^X + 1) + \psi(n^Y + 1) \right\rangle \tag{B.10}$$

The derivation of this alternative estimator is given in Ref.[90]. $\hat{I}^{(2)}(X,Y)$ presents a lower bias with respect to $\hat{I}^{(1)}(X,Y)$ but in exchange it has an higher variance. For this reason,in this work we chose $\hat{I}^{(1)}(X,Y)$ for the mutual information estimation.

Appendix C

A model of the heterogeneous relaxation in a viscous liquid

A first basis to connect fast and slow degrees of freedom was developed by Hall and Wolynes who pictured the glass transition as a freezing in an aperiodic crystal structure, assuming that atomic motion is restricted to cells [76]. As a result, the viscous flow is described in terms of activated jumps over energy barriers $\Delta E \propto k_B T a^2/\langle u^2 \rangle$ where a is the displacement to reach the transition state. The usual rate theory leads to the Hall-Wolynes equation:

$$\tau_\alpha^{(HW)}(a^2) \propto \exp\left(\frac{a^2}{2\langle u^2 \rangle}\right) \tag{C.1}$$

Eq.C.1 is expected to fail when τ_α becomes comparable to the typical rattling times of each atom in the cage of the surrounding atoms, corresponding to picosecond timescales.

One basic assumption of Eq.C.1 is that the distance to reach the transition state has a characteristic value a. Actually, this length scale is dispersed. To constrain the related distribution, $p(a^2)$, it is assumed that the latter does not depend on the state parameters such as the temperature, the density or the interacting potential. Averaging Eq.C.1 over the distribution $p(a^2)$ yields the structural relaxation time

$$\tau_\alpha = \left\langle \tau_\alpha^{(HW)}(a^2) \right\rangle_{a^2} \tag{C.2}$$

$$\equiv \int_0^\infty \tau_\alpha^{(HW)}(a^2)\, p(a^2) da^2 \tag{C.3}$$

This equation assumes the fact that the distribution of the relaxation times is mainly due to the distribution of the displacement to reach the transition state in the different local environments, whereas the average DW factor

$\langle u^2 \rangle$ is taken as homogeneous across the sample. This viewpoint relies on the picture that relaxation is related to long wavelength soft modes [35, 167]. Support has been provided by the strong correlation observed in glassformers between $\langle u^2 \rangle$ and the elastic modulus under quasi-static mechanical equilibrium [126]. As a suitable choice, the distribution of the squared distances $p(a^2)$ is taken as a truncated gaussian form [95, 116]

$$p(a^2) = \begin{cases} A \exp\left(-\frac{(a^2-\overline{a^2})^2}{2\sigma_{a^2}^2}\right) & \text{if } a > a_{min} \\ 0 & \text{otherwise} \end{cases} \tag{C.4}$$

where A is the normalization ensuring $\int_0^\infty p(a^2)\, da^2 = 1$ and a_{min}^2 is the minimum displacement to reach the transition state. Given the weak influence and to get rid of an adjustable parameter, one takes $a_{min}^2 = 0$ [95, 116]. The motivations behind the gaussian form of $p(a^2)$ mainly rely on the Central Limit Theorem. In fact, a^2 (r_0^2 in the notation of ref.[76]) is the cumulative squared displacement of the N moving particles in the system [76].

Plugging Eq.C.4 into Eq.C.3 leads to the following generalized HW equation (GHW) :

$$\tau_\alpha = \tau_0 \ \exp\left(\frac{\overline{a^2}}{2\langle u^2 \rangle} + \frac{\sigma_{a^2}^2}{8\langle u^2 \rangle^2}\right) \tag{C.5}$$

τ_0 is a suitable constant. An analogous law is anticipated for the viscosity η given the known near proportionality with τ_α [110]. Eq.C.5 is the form of the master curve Eq.4.2 adopted in our studies.

Bibliography

[1] http://lammps.sandia.gov.

[2] G. Adam and J. H. Gibbs. On the temperature dependence of cooperative relaxation properties in glass-forming liquids. *J. Chem. Phys.*, 43:139–146, 1965.

[3] A. N. Adhikari, N. A. Capurso, and D. Bingemann. Heterogeneous dynamics and dynamic heterogeneities at the glass transition probed with single molecule spectroscopy. *The Journal of Chemical Physics*, 127(11):114508, 2020/09/08 2007.

[4] S. Albert, T. Bauer, M. Michl, G. Biroli, J.-P. Bouchaud, A. Loidl, P. Lunkenheimer, R. Tourbot, C. Wiertel-Gasquet, and F. Ladieu. Fifth-order susceptibility unveils growth of thermodynamic amorphous order in glass-formers. *Science*, 352(6291):1308–1311, 2016.

[5] M. P. Allen and D. J. Tildesley. *Computer simulations of liquids*. Oxford university press, 1987.

[6] M. P. Allen and D. J. Tildesley. *Computer Simulation of Liquids*. Clarendon Press, New York, NY, USA, 1989.

[7] L. Andreozzi, M. Faetti, M. Giordano, and D. Leporini. Scaling between the rotational diffusion of tracers and the relaxation of polymers and glass formers. *J.Phys.:Condens. Matter*, 11:A131–A137, 1999.

[8] L. Andreozzi, M. Faetti, M. Giordano, and D. Leporini. Scaling of the rotational relaxation of tracers in o-terphenyl: A linear and nonlinear esr study. *The Journal of Physical Chemistry B*, 103(20):4097–4103, 1999.

[9] L. Andreozzi, M. Giordano, and D. Leporini. Linear and non-linear electron spin resonance study of the rotational diffusion of a molecular tracer in supercooled o-terphenyl. *J. Non-Cryst. Solids*, 235:219–224, 1998.

[10] C. Angell. Relaxation in liquids, polymers and plastic crystals - strong/fragile patterns and problems. *J.Non-Crystalline Sol.*, 131-133:13–31, 1991.

[11] C. A. Angell. Perspective on the glass transition. *J. Phys. Chem. Solids.*, 49:863–871, 1988.

[12] C. A. Angell. Formation of glasses from liquids and biopolymers. *Science*, 267:1924–1935, 1995.

[13] C. A. Angell, K. L. Ngai, G. B. McKenna, P. McMillan, and S.W.Martin. Relaxation in glassforming liquids and amorphous solids. *J. Appl. Phys.*, 88:3113–3157, 2000.

[14] A. Arbe, U. Buchenau, L. Willner, D. Richter, B. Farago, and J. Colmenero. Study of the dynamic structure factor in the β relaxation regime of polybutadiene. *Phys. Rev. Lett.*, 76:1872–1875, Mar 1996.

[15] A. Arbe, D. Richter, J. Colmenero, and B. Farago. Merging of the α and β relaxations in polybutadiene: A neutron spin echo and dielectric study. *Physical Review E*, 54(4):3853–3869, 10 1996.

[16] N. W. Ashcroft and N. D. Mermin. *Solid State Physics*. Holt, Rinehart and Wiston, New York, 1976.

[17] S. S. Ashwin and S. Sastry. Low-temperature behaviour of the kob-andersen binary mixture. *J.Phys.: Condens. Matter*, 15:S1253–S1258, 2003.

[18] I. Avramov. Viscosity in disordered media. *J. Non-Cryst. Solids*, 351:3163–3173, 2005.

[19] C. Balbuena, M. M. Gianetti, and E. R. Soulé. Looking at the dynamical heterogeneity in a supercooled polymer system through isoconfigurational ensemble. *The Journal of Chemical Physics*, 149(9):094506, 2021/02/11 2018.

[20] A. Barbieri, E. Campani, S. Capaccioli, and D. Leporini. Molecular dynamics study of the thermal and the density effects on the local and the large-scale motion of polymer melts: Scaling properties and dielectric relaxation. *J. Chem. Phys.*, 120:437–453, 2004.

[21] A. Barbieri, G. Gorini, and D. Leporini. Role of the density in the crossover region of o-terphenyl and poly(vinyl acetate). *Phys. Rev. E*, 69:061509, 2004.

[22] J. L. Barrat and M. L. Klein. Molecular dynamics simulations of supercooled liquids near the glass transition. *Annu. Rev. Phys. Chem.*, 42:23–53, 1991.

[23] H. Bässler. Viscous flow in supercooled liquids analyzed in terms of transport theory for random media with energetic disorder. *Phys. Rev. Lett.*, 58:767–770, 1987.

[24] M. Becchi, A. Giuntoli, and D. Leporini. Molecular layers in thin supported films exhibit the same scaling as the bulk between slow relaxation and vibrational dynamics. *Soft Matter*, 14:8814–8820, 2018.

[25] O. M. Becker. *Computational Biochemistry and Biophysics*. Marcel Dekker Inc., 2001.

[26] D. Bedrov and G. D. Smith. Molecular dynamics simulation study of the α and β-relaxation processes in a realistic model polymer. *Physical Review E*, 71(5):050801, 2005.

[27] D. Bedrov and G. D. Smith. Secondary johari–goldstein relaxation in linear polymer melts represented by a simple bead-necklace model. *Journal of Non-Crystalline Solids*, 357(2):258–263, 2011.

[28] L. A. Belfiore. Physical properties of macromolecules. 2010.

[29] S. Bernini and D. Leporini. Cage effect in supercooled molecular liquids: Local anisotropies and collective solid-like response. *The Journal of Chemical Physics*, 144(14):144505, 2016.

[30] S. Bernini, F. Puosi, M. Barucco, and D. Leporini. Competition of the connectivity with the local and the global order in polymer melts and crystals. *J. Chem. Phys.*, 139:184501, 2013.

[31] L. Berthier and G. Biroli. Theoretical perspective on the glass transition and amorphous materials. *Rev. Mod. Phys.*, 83:587–645, 2011.

[32] B. P. Bhowmik, I. Tah, and S. Karmakar. Non-gaussianity of the van hove function and dynamic-heterogeneity length scale. *Physical Review E*, 98(2):022122–, 08 2018.

[33] G. Biroli, S. Karmakar, and I. Procaccia. Comparison of static length scales characterizing the glass transition. *Phys. Rev. Lett.*, 111:165701, Oct 2013.

[34] P. Bordat, F. Affouard, M. Descamps, and K. L. Ngai. Does the interaction potential determine both the fragility of a liquid and the vibrational properties of its glassy state? *Phys. Rev. Lett.*, 93:105502, 2004.

[35] U. Buchenau and R. Zorn. A relation between fast and slow motions in glassy and liquid selenium. *Europhys. Lett.*, 18:523–528, 1992.

[36] D. Cangialosi. Dynamics and thermodynamics of polymer glasses. 26(15):153101, 2014.

[37] S. Capaccioli, M. Paluch, D. Prevosto, L.-M. Wang, and K. L. Ngai. Many-body nature of relaxation processes in glass-forming systems. *The Journal of Physical Chemistry Letters*, 3(6):735–743, 2012.

[38] F. Caporaletti, S. Capaccioli, S. Valenti, M. Mikolasek, A. I. Chumakov, and G. Monaco. A microscopic look at the johari-goldstein relaxation in a hydrogen-bonded glass-former. *Scientific Reports*, 9(1):14319, 2019.

[39] A. Cavagna. Supercooled liquids for pedestrians. *Phys. Rep.*, 476:51–124, 2009.

[40] H. S. Chen and M. Goldstein. Anomalous viscoelastic behaviour of metallic glasses of pd–si-based alloys. *J. Appl. Phys.*, 43:1642–1648, 1972.

[41] M. T. Cicerone and M. Tyagi. Metabasin transitions are johari-goldstein relaxation events. *The Journal of Chemical Physics*, 146(5):054502, 2020/10/25 2017.

[42] T. M. Cover and J. A. Thomas. *Elements of Information Theory*. Wiley-Interscience, New York, 2006.

[43] C. De Michele, E. Del Gado, and D. Leporini. Scaling between structural relaxation and particle caging in a model colloidal gel. *Soft Matter*, 7:4025–4031, 2011.

[44] C. De Michele and D. Leporini. Viscous flow and jump dynamics in molecular supercooled liquids. i. translations. *Phys. Rev. E*, 63:036701, 2001.

[45] P. G. Debenedetti. *Metastable Liquids*. Princeton University Press, Princeton USA, 1997.

[46] P. G. Debenedetti. Supercooled and glassy water. *J. Phys.: Condens. Matter*, 15:R1669–R1726, 2003.

[47] P. G. Debenedetti and F. H. Stillinger. Supercooled liquids and the glass transition. *Nature*, 410:259–267, 2001.

[48] P. G. deGennes. *Scaling Concepts in Polymer Physics.* Cornell University Press, 1988.

[49] M. Doi and S. F. Edwards. *The Theory of Polymer Dynamics.* Clarendon Press, 1988.

[50] C. Donati, J. F. Douglas, W. Kob, S. J. Plimpton, P. H. Poole, and S. C. Glotzer. Stringlike cooperative motion in a supercooled liquid. *Physical Review Letters*, 80(11):2338–2341, 03 1998.

[51] C. Donati, S. C. Glotzer, and P. H. Poole. Growing spatial correlations of particle displacements in a simulated liquid on cooling toward the glass transition. *Physical Review Letters*, 82(25):5064–5067, 06 1999.

[52] J. Douglas and D. Leporini. Obstruction model of the fractional stokes-einstein relation in glass-forming liquids. *J. Non-Cryst. Solids*, 235-237:137–141, 1998.

[53] J. F. Douglas, B. A. P. Betancourt, X. Tong, and H. Zhang. Localization model description of diffusion and structural relaxation in glass-forming cu–zr alloys. *Journal of Statistical Mechanics: Theory and Experiment*, 2016(5):054048, may 2016.

[54] J. P. K. Doye, D. J. Wales, and R. S. Berry. The effect of the range of the potential on the structures of clusters. *J. Chem. Phys.*, 103:4234–4249, 1995.

[55] A. J. Dunleavy, K. Wiesner, and C. P. Royall. Using mutual information to measure order in model glass-formers. *Phys. Rev. E*, 86:041505, 2012.

[56] A. J. Dunleavy, K. Wiesner, R. Yamamoto, and C. P. Royall. Mutual information reveals multiple structural relaxation mechanisms in a model glass former. *Nature Communications*, 6:6089, 2015.

[57] J. C. Dyre. The glass transition and elastic models of glass-forming liquids. *Rev. Mod. Phys.*, 78:953–972, 2006.

[58] J. C. Dyre, N. B. Olsen, and T. Christensen. Local elastic expansion model for viscous-flow activation energies of glass-forming molecular liquids. *Phys. Rev. B*, 53:2171–2174, 1996.

[59] M. D. Ediger. Spatially heterogeneous dynamics in supercooled liquids. *Annu. Rev. Phys. Chem.*, 51:99–128, 2000.

[60] Y. S. Elmatad, D. Chandler, and J. P. Garrahan. Corresponding states of structural glass formers. *J. Phys. Chem. B*, 113:5563–5567, 2009.

[61] D. J. Evans and G. Morriss. *Statistical Mechanics of Nonequilibrium Liquids*. Cambridge University Press, Cambridge, 2008.

[62] D. Fragiadakis and C. M. Roland. Molecular dynamics simulation of the johari-goldstein relaxation in a molecular liquid. *Phys. Rev. E*, 86:020501, 2012.

[63] D. Fragiadakis and C. M. Roland. Dynamic correlations and heterogeneity in the primary and secondary relaxations of a model molecular liquid. *Physical Review E*, 89(5):052304–, 05 2014.

[64] D. Fragiadakis and C. M. Roland. Participation in the johari–goldstein process: Molecular liquids versus polymers. *Macromolecules*, 50(10):4039–4042, 2017.

[65] D. Fragiadakis and C. M. Roland. Chain flexibility and the segmental dynamics of polymers. *The Journal of Physical Chemistry B*, 123(27):5930–5934, 07 2019.

[66] M. C. Gao and M. Widom. Information entropy of liquid metals. *The Journal of Physical Chemistry B*, 122(13):3550–3555, 2018.

[67] U. W. Gedde. *Polymer Physics*. Chapman and Hall, London, London, 1995.

[68] M. Goldstein. Viscous liquids and the glass transition: A potential energy barrier picture. *The Journal of Chemical Physics*, 51(9):3728–3739, 2020/10/25 1969.

[69] M. Goldstein. Communications: Comparison of activation barriers for the johari–goldstein and alpha relaxations and its implications. *The Journal of Chemical Physics*, 132(4):041104, 2020/10/25 2010.

[70] R. J. Greet and D. Turnbull. Glass transition in o-terphenil. *J. Chem. Phys.*, 46:1243–1251, 1967.

[71] A. Y. Grosberg and A. R. Khokhlov. *Statistical physics of macromolecules*. AIP Press, 1994.

[72] M. Guaita, F. Ciardeli, F. L. Mantia, and E. Pedemonte. *Fondamenti di scienza dei polimeri*. Pacini Editore, 1998.

[73] E. Guillaud, L. Joly, D. de Ligny, and S. Merabia. Assessment of elastic models in supercooled water: A molecular dynamics study with the tip4p/2005f force field. *The Journal of Chemical Physics*, 147(1):014504, 2017.

[74] S. Gupta, E. Mamontov, N. Jalarvo, L. Stingaciu, and M. Ohl. Characteristic length scales of the secondary relaxations in glass-forming glycerol. *The European Physical Journal E*, 39(3):40, 2016.

[75] R. R. H. B. Yu and K. Samwer. Structural rearrangements governing johari-goldstein relaxations in metallic glasses. *Sci. Adv.*, 3:1701577, 2017.

[76] R. W. Hall and P. G. Wolynes. The aperiodic crystal picture and free energy barriers in glasses. *J. Chem. Phys.*, 86:2943–2948, 1987.

[77] J. P. Hansen and I. R. McDonald. *Theory of Simple Liquids, 3rd Ed.* Academic Press, 2006.

[78] R. Hilfer. Analytical representations for relaxation functions of glasses. *Journal of Non-Crystalline Solids*, 305(1):122–126, 2002.

[79] W. G. Hoover. Canonical dynamics: Equilibrium phase-space distributions. *Physical Review A*, 31(3):1695–1697, 03 1985.

[80] R. Horstmann and M. Vogel. Common behaviors associated with the glass transitions of water-like models. *The Journal of Chemical Physics*, 147(3):034505, 2017.

[81] F. S. Howell, R. A. Bose, P. B. Macedo, and C. T. Moynihan. Electrical relaxation in a glass-forming molten salt. *J. Phys. Chem.*, 78:639–648, 1974.

[82] J. Iaconis, S. Inglis, A. B. Kallin, and R. G. Melko. Detecting classical phase transitions with renyi mutual information. *Physical Review B*, 87(19):195134–, 05 2013.

[83] R. L. Jack, A. J. Dunleavy, and C. P. Royall. Information-theoretic measurements of coupling between structure and dynamics in glass formers. *Phys. Rev. Lett.*, 113(9):095703, 2014.

[84] E. T. Jaynes. Information theory and statistical mechanics. *Physical Review*, 106(4):620–630, 05 1957.

[85] G. P. Johari and M. Goldstein. Viscous liquids and the glass transition. ii. secondary relaxations in glasses of rigid molecules. *J. Chem. Phys.*, 53:2372, 1970.

[86] Y. Jung, J. P. Garrahan, and D. Chandler. Excitation lines and the breakdown of stokes-einstein relations in supercooled liquids. *Phys. Rev. E*, 69:061205, Jun 2004.

[87] S. Karmakar, C. Dasgupta, and S. Sastry. Length scales in glass-forming liquids and related systems: a review. *Reports on Progress in Physics*, 79(1):016601, dec 2015.

[88] W. Kob. Computer simulations of supercooled liquids and glasses. *J. Phys.: Condens. Matter*, 11:R85–R115, 1999.

[89] L. F. Kozachenko and N. N. Leonenko. Sample estimate of the entropy of a random vector. *Problems Inform. Transmission*, 23(2):95–101, 1987.

[90] A. Kraskov, H. Stögbauer, and P. Grassberger. Estimating mutual information. *Phys. Rev. E*, 69:066138, 2004.

[91] K. Kremer and G. S. Grest. Dynamics of entangled linear polymer melts: A molecular-dynamics simulation. *J. Chem. Phys.*, 92:5057–5086, 1990.

[92] K. Kremer, G. S. Grest, and I. Carmesin. Crossover from rouse to reptation dynamics: A molecular-dynamics simulation. *Phys. Rev. Lett.*, 61:566–569, Aug 1988.

[93] M. Kröger. Simple models for complex nonequilibrium fluids. *Phys. Rep.*, 390:453–551, 2004.

[94] L. Larini, A. Barbieri, D. Prevosto, P. A. Rolla, and D. Leporini. Equilibrated polyethylene single-molecule crystals: molecular-dynamics simulations and analytic model of the global minimum of the free-energy landscape. *J. Phys.: Condens. Matter*, 17:L199–L208, 2005.

[95] L. Larini, A. Ottochian, C. De Michele, and D. Leporini. Universal scaling between structural relaxation and vibrational dynamics in glass-forming liquids and polymers. *Nature Physics*, 4:42–45, 2008.

[96] D. Leporini. Relationship between a nonlinear response and relaxation induced by colored noise. *Phys. Rev. A*, 49:992–1014, Feb 1994.

[97] W. Li. Mutual information functions versus correlation functions. *Journal of Statistical Physics*, 60(5):823–837, 1990.

[98] M. Lin, H.W.; Tegmark. Critical behavior in physics and probabilistic formal languages. *Entropy*, 19(7):299, 2017.

[99] Q. Z. M. T. Cicerone and M. Tyagi. Picosecond dynamic heterogeneity, hopping, and johari-goldstein relaxation in glass-forming liquids. *Phys. Rev. Lett.*, 113:117801, 2014.

[100] G. Maccari, G. Spampinato, and V. Tozzini. Ssecstant: Secondary structure analysis tool for data selection, statistics and models building. *Bioinf. Adv. Acc.*, 30(5):668–674, 2013.

[101] A. Malins, S. R. Williams, J. Eggers, and C. P. Royall. Identification of structure in condensed matter with the topological cluster classification. *The Journal of Chemical Physics*, 139(23):234506, 2019/07/04 2013.

[102] L.-M. Martinez and C. A. Angell. A thermodynamic connection to the fragility of glass-forming liquids. *Nature*, 410:663–667, 2001.

[103] N. G. McCrum, B. E. Read, and G. Williams. *Anelastic and Dielectric Effects in Polymeric Solids*. Dover Publications, New York, 1991.

[104] M. Mézard and A. Montanari. *Information, Physics, and Computation*. Oxford University Press, Oxford, 2009.

[105] G. Moruzzi. *Appunti di Struttura della Materia II*. Università di Pisa, 2013.

[106] C. Ness, V. V. Palyulin, R. Milkus, R. Elder, T. Sirk, and A. Zaccone. Nonmonotonic dependence of polymer-glass mechanical response on chain bending stiffness. *Phys Rev E*, 96(3-1):030501, Sep 2017.

[107] K. Ngai. Relation between some secondary relaxations and the a relaxations in glass-forming materials according to the coupling model. *J. Chem. Phys.*, 109:6982–6994, 1998.

[108] K. L. Ngai. Dynamic and thermodynamic properties of glass-forming substances. *J. Non-Cryst. Solids*, 275:7–51, 2000.

[109] K. L. Ngai. Why the fast relaxation in the picosecond to nanosecond time range can sense the glass transition. *Phil. Mag.*, 84:1341–1353, 2004.

[110] K. L. Ngai. *Relaxation and Diffusion in Complex Systems*. Springer, Berlin, 2011.

[111] K. L. Ngai and M. Paluch. Classification of secondary relaxation in glass-formers based on dynamic properties. *The Journal of Chemical Physics*, 120(2):857–873, 2004.

[112] S. Nosé. A unified formulation of the constant temperature molecular dynamics methods. *J. Chem. Phys.*, 81:511–519, 1984.

[113] V. N. Novikov and A. P. Sokolov. Role of quantum effects in the glass transition. *Phys. Rev. Lett.*, 110:065701, 2013.

[114] I. U. of Pure, A. Chemistry., C. on Macromolecular Nomenclature., and W. V. Metanomski. *Compendium of macromolecular nomenclature*. Blackwell Scientific Publications, Oxford; Boston, 1991.

[115] A. Ottochian, C. De Michele, and D. Leporini. Non-gaussian effects in the cage dynamics of polymers. *Philosophical Magazine*, 88:4057–4062, 2008.

[116] A. Ottochian, C. De Michele, and D. Leporini. Universal divergence-less scaling between structural relaxation and caged dynamics in glass-forming systems. *J. Chem. Phys.*, 131:224517, 2009.

[117] A. Ottochian and D. Leporini. Scaling between structural relaxation and caged dynamics in $ca_{0.4}k_{0.6}(no_3)_{1.4}$ and glycerol: free volume, time scales and implications for the pressure-energy correlations. *Philosophical Magazine*, 91:1786–1795, 2011.

[118] A. Ottochian and D. Leporini. Universal scaling between structural relaxation and caged dynamics in glass-forming systems: Free volume and time scales. *J. Non-Cryst. Solids*, 357:298–301, 2011.

[119] L. Paninski. Estimation of entropy and mutual information. *Neural Computation*, 15(6):1191–1253, 2020/09/21 2003.

[120] L. C. Pardo, P. Lunkenheimer, and A. Loidl. Dielectric spectroscopy in benzophenone: The *beta* relaxation and its relation to the mode-coupling cole-cole peak. *Physical Review E*, 76(3):030502–, 09 2007.

[121] B. A. Pazmiño Betancourt, P. Z. Hanakata, F. W. Starr, and J. F. Douglas. Quantitative relations between cooperative motion, emergent elasticity, and free volume in model glass-forming polymer materials. *Proc. Natl. Acad. Sci. USA*, 112:2966–2971, 2015.

[122] S. Plimpton. Fast parallel algorithms for short-range molecular dynamics. *J. Comput. Phys.*, 117:1–19, 1995.

[123] F. Puosi, O. Chulkin, S. Bernini, S. Capaccioli, and D. Leporini. Thermodynamic scaling of vibrational dynamics and relaxation. *J. Chem. Phys.*, 145:234904, 2016.

[124] F. Puosi and D. Leporini. Scaling between relaxation, transport, and caged dynamics in polymers: From cage restructuring to diffusion. *J.Phys. Chem. B*, 115:14046–14051, 2011.

[125] F. Puosi and D. Leporini. Communication: Fast and local predictors of the violation of the stokes- einstein law in polymers and supercooled liquids. *J. Chem. Phys.*, 136:211101, 2012.

[126] F. Puosi and D. Leporini. Correlation of the instantaneous and the intermediate-time elasticity with the structural relaxation in glassforming systems. *J. Chem. Phys.*, 136:041104, 2012.

[127] F. Puosi and D. Leporini. Spatial displacement correlations in polymeric systems. *J. Chem. Phys.*, 136:164901, 2012.

[128] F. Puosi and D. Leporini. Erratum: "spatial displacement correlations in polymeric systems" [j. chem. phys.136, 164901 (2012)]. *J. Chem. Phys.*, 139:029901, 2013.

[129] F. Puosi and D. Leporini. Communication: Fast dynamics perspective on the breakdown of the stokes-einstein law in fragile glassformers. *J. Chem. Phys.*, 148:131102, 2018.

[130] F. Puosi, C. D. Michele, and D. Leporini. Scaling between relaxation, transport and caged dynamics in a binary mixture on a per-component basis. *J. Chem. Phys.*, 138:12A532, 2013.

[131] F. Puosi, A. Tripodo, and D. Leporini. Fast vibrational modes and slow heterogeneous dynamics in polymers and viscous liquids. *International Journal of Molecular Sciences*, 20(5708), 2019.

[132] R. Richert. Heterogeneous dynamics in liquids: fluctuations in space and time. *J. Phys.: Condens. Matter*, 14:R703–R738, 2002.

[133] D. Richter, M. Monkenbusch, A. Arbe, J. Colmenero, and B. Farago. Dynamic structure factors due to relaxation processes in glass-forming polymers. *Physica B: Condensed Matter*, 241-243:1005–1012, 1997.

[134] S. Rogers and L. Mandelkern. Glass transition of the poly-(n-alkyl methacrylates). *J. Phys. Chem.*, 61:985–991, 1957.

[135] C. P. Royall, A. Malins, A. J. Dunleavy, and R. Pinney. Strong geometric frustration in model glassformers. *Journal of Non-Crystalline Solids*, 407:34–43, 2015.

[136] C. P. Royall and S. R. Williams. C60: The first one-component gel? *The Journal of Physical Chemistry B*, 115(22):7288–7293, 06 2011.

[137] C. P. Royall, S. R. Williams, T. Ohtsuka, and H. Tanaka. Direct observation of a local structural mechanism for dynamic arrest. *Nat. Mater.*, 7:556–561, 2008.

[138] S. Sastry, P. G. Debenedetti, and F. H. Stillinger. Signatures of distinct dynamical regimes in the energy landscape of a glass-forming liquid. *Nature*, 393(6685):554–557, 1998.

[139] B. Schnell, H. Meyer, C. Fond, J. P. Wittmer, and J. Baschnagel. Simulated glass-forming polymer melts: Glass transition temperature and elastic constants of the glassy state. *The European Physical Journal E*, 34(9):97, 2011.

[140] T. Scopigno, G. Ruocco, F. Sette, and G. Monaco. Is the fragility of a liquid embedded in the properties of its glass? *Science*, 302(5646):849–852, 2003.

[141] C. E. Shannon. A mathematical theory of communication. *Bell System Technical Journal*, 27(3):379–423, 2019/05/08 1948.

[142] J. Shao and C. A. Angell. Vibrational anharmonicity and the glass transition in strong and fragile vitreous polymorphs. In *Proc. XVIIth International Congress on Glass, Beijing*, volume 1, pages 311–320. Chinese Ceramic Societ, 1995.

[143] H. Sillescu. Heterogeneity at the glass transition: a review. *Journal of Non-Crystalline Solids*, 243(2):81–108, 1999.

[144] D. S. Simmons, M. T. Cicerone, Q. Zhong, M. Tyagic, and J. F. Douglas. Generalized localization model of relaxation in glass-forming liquids. *Soft Matter*, 8:11455–11461, 2012.

[145] G. D. Smith and D. Bedrov. A molecular dynamics simulation study of the α- and β-relaxation processes in 1,4-polybutadiene. *Journal of Non-Crystalline Solids*, 352(42):4690 – 4695, 2006.

[146] R. S. Smith and B. D. Kay. Breaking through the glass ceiling: Recent experimental approaches to probe the properties of supercooled liquids near the glass transition. *J. Phys. Chem. Lett.*, 3:725–730, 2012.

[147] P. V. Sriluckshmy and I. Mandal. Critical scaling of the mutual information in two-dimensional disordered ising models. *Journal of Statistical Mechanics: Theory and Experiment*, 2018:043301, 2018.

[148] F. Starr, S. Sastry, J. F. Douglas, and S. Glotzer. What do we learn from the local geometry of glass-forming liquids? *Phys. Rev. Lett.*, 89:125501, 2002.

[149] F. W. Starr, J. F. Douglas, and S. Sastry. The relationship of dynamical heterogeneity to the adam-gibbs and random first-order transition theories of glass formation. *The Journal of Chemical Physics*, 138(12):12A541, 2021/02/15 2013.

[150] F. Stillinger. A topographic view of supercooled liquids and glass formation. *Science*, 267:1935–1939, 1995.

[151] G. Strobl. *The Physics of Polymers, III Ed.* Springer, Berlin, 2007.

[152] W. Swope, H. Andersen, H. Berens, and K. Wilson. A computer simulationmethod for the calculation of equilibrium constants for the formation of physical clusters of molecules: Application to small water clusters. *J. Chem. Phys.*, 76:637–649, 1982.

[153] D. C. T. Scopigno and G. Ruocco. Universal relation between viscous flow and fast dynamics in glass-forming materials. *Phys. Rev. B*, 81:100202, 2010.

[154] J. Taffs, A. Malins, S. R. Williams, and C. P. Royall. A structural comparison of models of colloid-polymer mixtures. *J. Phys.: Condens. Matter*, 22:104119, 2010.

[155] G. Tarjus and D. Kivelson. Breakdown of the stokes–einstein relation in supercooled liquids. *The Journal of Chemical Physics*, 103(8):3071–3073, 1995.

[156] A. Tobolsky, R. E. Powell, and H. Eyring. Elastic-viscous properties of matter. In R. E. Burk and O. Grummit, editors, *Frontiers in Chemistry*, volume 1, pages 125–190, New York, 1943. Interscience.

[157] A. Tölle. Neutron scattering studies of the model glass former *ortho*-terphenyl. *Rep. Prog. Phys.*, 64:1473–1532, 2001.

[158] N. Tomoshige, H. Mizuno, T. Mori, K. Kim, and N. Matubayasi. Boson peak, elasticity, and glass transition temperature in polymer glasses: Effects of the rigidity of chain bending. *Scientific Reports*, 9(1):19514, 2019.

[159] U. Tracht, M. Wilhelm, A. Heuer, H. Feng, K. Schmidt-Rohr, and H. W. Spiess. Length scale of dynamic heterogeneities at the glass transition determined by multidimensional nuclear magnetic resonance. *Phys. Rev. Lett.*, 81:2727–2730, 1998.

[160] A. Tripodo, A. Giuntoli, M. Malvaldi, and D. Leporini. Mutual information does not detect growing correlations in the propensity of a model molecular liquid. *Soft Matter*, 2019.

[161] A. Tripodo, F. Puosi, M. Malvaldi, S. Capaccioli, and D. Leporini. Coincident correlation between vibrational dynamics and primary relaxation of polymers with strong or weak johari-goldstein relaxation. *Polymers*, 12(761), 2020.

[162] A. Tripodo, F. Puosi, M. Malvaldi, and D. Leporini. Vibrational scaling of the heterogeneous dynamics detected by mutual information. *Eur. Phys. J. E*, 42(11), 2019.

[163] L. Verlet. Computer "experiments" on classical fluids. i. thermodynamical properties of lennard-jones molecules. *Phys. Rev.*, 159:98–103, 1967.

[164] E. Vidal Russell and N. E. Israeloff. Direct observation of molecular cooperativity near the glass transition. *Nature*, 408(6813):695–698, 2000.

[165] A. Widmer-Cooper and P. Harrowell. Predicting the long-time dynamic heterogeneity in a supercooled liquid on the basis of short-time heterogeneities. *Phys. Rev. Lett.*, 96:185701, 2006.

[166] A. Widmer-Cooper, P. Harrowell, and H. Fynewever. How reproducible are dynamic heterogeneities in a supercooled liquid? *Phys. Rev. Lett.*, 93:135701, 2004.

[167] A. Widmer-Cooper, H. Perry, P. Harrowell, and D. R. Reichman. Irreversible reorganization in a supercooled liquid originates from localized soft modes. *Nature Physics*, 4:711–715, 2008.

[168] M. Wyart and M. E. Cates. Does a growing static length scale control the glass transition? *Phys. Rev. Lett.*, 119:195501, Nov 2017.

[169] X. Xia and P. G. Wolynes. Fragilities of liquids predicted from the random first order transition theory of glasses. *Proc. Natl. Acad. Sci. USA*, 97:2990–2994, 2000.

[170] H. B. Yu, W. H. Wang, H. Y. Bai, and K. Samwer. The β-relaxation in metallic glasses. *National Science Review*, 1(3):429–461, 2/23/2021 2014.

[171] H. Zhang, D. J. Srolovitz, J. F. Douglas, and J. A. Warren. Grain boundaries exhibit the dynamics of glass-forming liquids. *Proc. Natl. Acad. Sci. USA*, 106:7735–7740, 2009.

[172] R. Zorn. Deviation from gaussian behavior in the self-correlation function of the proton motion in polybutadiene. *Physical Review B*, 55(10):6249–6259, 03 1997.

[173] R. Zorn, A. Arbe, J. Colmenero, B. Frick, D. Richter, and U. Buchenau. Neutron scattering study of the picosecond dynamics of polybutadiene and polyisoprene. *Physical Review E*, 52(1):781–795, 07 1995.